Politecnico di Milano

SCUOLA DI INGEGNERIA INDUSTRIALE E DELL'INFORMAZIONE

Aeronautical Engineering

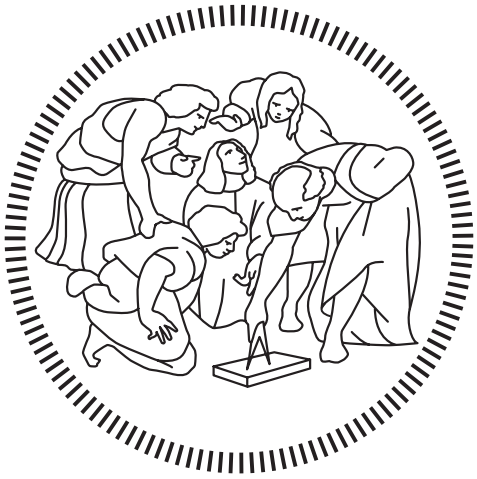

Noise analysis in the wind turbine design process

Relatore

Prof. Alessandro Croce

Autore

Federico Cattaneo

Matricola

920243

Anno Accademico 2019 – 2020

Ringraziamenti

Giunto al termine del mio percorso ci tengo innanzitutto a ringraziare il professor Croce per avermi dato l'opportunità di svolgere la mia tesi su un argomento che ritengo particolarmente interessante e attuale. Un grazie va anche a Luca, per la disponibilità e la bravura; senza il suo contributo orientarsi nel complesso codice Cp Max sarebbe stato arduo.

È strano pensare che il mio percorso in università sia terminato, che siano ormai passati più di cinque anni da quando ho messo piede per la prima volta al Polimi. Ogni anno porta con sé le proprie fatiche ma anche le proprie gioie e soddisfazioni; ma soprattutto ogni anno regala molti volti. Durante il mio percorso, infatti, ho avuto modo di incontrare e conoscere molte persone, che hanno permesso di alleggerire le interminabili ore di lezione e di stemperare la tensione dovuta agli esami. Vi avrei voluti ringraziare tutti personalmente, festeggiare insieme gli ultimi momenti in università, ma purtroppo non ci è possibile. Un grazie va a tutti, ma è doveroso citare coloro che maggiormente hanno condiviso questo viaggio con me: Silvia e Alessandro con cui ho trascorso i viaggi in treno parlando di moto, basket e qualsiasi altra cosa ci passasse per la mente. Andrea e Antonio con cui ho condiviso molte lezioni dal fondo dell'aula, e a cui poi si sono aggiunti Andrea, Marco e Luca: grazie a tutti voi per aver rotto la monotonia di ogni giornata di triennale. Ci tengo particolarmente a ringraziare anche Tiziana, una persona speciale, sempre disponibile e gentile, e Noraiz, mio fedele compagno di giornate durante l'ultimo anno: non credo di aver mai conosciuto una persona tanto intelligente e al tempo stesso umile e disponibile. Infine Samuele, con cui ho condiviso i mesi di realizzazione della tesi, e che è stato un prezioso supporto e fonte di confronto per problematiche e preoccupazioni.

Un ringraziamento speciale va alla mia famiglia, ai miei zii e a mia nonna. Un grazie immenso è da destinarsi in particolare ai miei genitori, Mauro e Piera. Se posso ritenermi orgoglioso di quello che sono è principalmente merito vostro. Mi avete insegnato ad affrontare ogni impegno dando sempre il 100 % di me stesso e ad accettare anche le sconfitte e i risultati negativi. Avete sempre creduto in me, spronandomi senza mai forzarmi, lasciandomi la libertà di fare ciò che volevo. Da voi ho impara-

to quanto conti il sacrificio del lavoro, quanto sia importante la generosità e qual è il vero significato della felicità. Non siete perfetti, ma non avrei potuto chiedere genitori migliori. Un grazie speciale va anche a Nicolò e Giulia, mia sorella. So che ci sei e ci sarai sempre quando ne avrò bisogno.

Un grazie anche a tutti i miei amici che mi hanno accompagnato in questo cammino. Sono stati anni di cambiamento e molte persone ne hanno condiviso anche solo una piccola parte. Sarebbe impossibile citarvi tutti, ma sappiate che ognuno di voi mi ha lasciato qualcosa e che non vi dimenticherò mai. Due persone in particolare ci sono sempre state sin dalla prima elementare, grazie Francesca e Serena.

Infine è impossibile pensare a quello che sono, al traguardo che oggi raggiungo senza di te, Alice. Sei sempre stata la mia forza durante questo cammino. In ogni mio momento di fragilità mi hai dato l'energia e il vigore di lottare con tutto me stesso. Mi hai sempre ricordato chi sono, dandomi l'autostima necessaria nei momenti di difficoltà. Le parole non possono rappresentare quanto tu sia importante per me. Sei il mio punto d'appoggio, la mia colonna portante. Hai sempre la parola giusta per ogni mia ansia o paura. In qualsiasi mood io sia con te sto meglio. Sai farmi ridere, scherzare, ma anche riflettere. Grazie per esserci sempre.

Abstract

The present thesis focuses on the development and improvement of tools for the design process of a wind turbine. In particular, the main goal is to implement a predictive noise analysis inside the design loop to limit the noise emissions of the final configuration. The idea is to modify the shape of the airfoils composing the blades, by using a recently implemented *free-form* optimization method, and the distributions of the chord, in order to find the most performing turbine that respects the imposed limit on noise emissions. The latter are considered as constraints during the whole optimization process.

The main tool used is *Cp-Max*, which is the framework in use for wind turbine design and simulation at Politecnico di Milano. It is modified especially in its aerodynamic optimization cycle, which has the goal to maximize the annual energy production, AEP. The *free-form* optimization method requires the use of the software *XFoil* to compute the polar curves of the airfoils in order to increase the efficiency of the blade and, consequently, the AEP. Also the noise analysis, which is founded on semi-empirical frequency based models, demands the use of *XFoil* to characterize the boundary layer developed along the blade. The tool requires, also, the use of *Cp-Lambda*, which is an aero-servo-elastic finite element software able to compute various aerodynamic and geometric variables used by the semi-empirical models.

The noise evaluation tool is simplified to reduce the computational time and a sensitive analysis is performed to show the differences with the original one. Furthermore, to save time, specific dynamic simulations are implemented for the acoustic analysis. At the beginning of the work data were retrieved from dynamic load case simulations computed for structural reasons and that last 10 minutes according to regulations. Noise analysis, instead, only requires few seconds. Then, the tool is integrated inside the aerodynamic cycle and used to compute a constraint to be respected by the optimized configuration. Lastly, the robustness of the *free-form* method is raised by introducing a new limit on the minimum thickness of the airfoils from the mid-chord towards the trailing edge. Indeed, initial simulations crash due to the permeation of suction and pressure side.

The contributions of three noise sources are considered: turbulent boundary layer - trailing edge noise, computed according to the TNO-DTU model; turbulent inflow

noise, computed according to *Amiet* and *Lowson* models; trailing edge bluntness noise, computed according to *Brooks, Pope, Marcolini* model. It's important to underline that the models used are very common in literature and reproduce reasonable qualitatively results, while no quantitative validation is performed due to the unavailability of experimentally measured data.

The new implemented code is tested on a 10 MW wind turbine of class 1A. The results found show that the total noise reduction depends on the noise source that is predominant. Indeed, the design of the blade affects strongly the bluntness noise generation and the turbulent boundary layer - trailing edge one, whereas it has only an indirect influence on the turbulent inflow noise. Nevertheless, the preliminary simulations performed are successful and show the possibility to introduce noise emissions inside the design process of a wind turbine.

Sommario

Il presente lavoro di tesi è incentrato sullo sviluppo e il miglioramento del processo di design di un turbina eolica. In particolare, l'obiettivo principale è stato quello di implementare un'analisi predittiva del rumore all'interno del ciclo di design, in modo da limitare il rumore prodotto dalla configurazione finale del generatore. L'idea è stata quella di modificare la forma dei profili che compongono le pale, grazie all'uso del metodo di ottimizzazione di *free-form* recentemente implementato, e della distribuzione di corda, in modo da trovare la configurazione più performante in grado di rispettare i limiti imposti sulle emissioni di rumore. Queste ultime sono state considerate come un vincolo di progettazione durante l'intero processo di ottimizzazione.

Il principale strumento utilizzato è stato *Cp-Max*, che è il software di progettazione e simulazione di turbine eoliche attualmente in uso al Politecnico Di Milano. In particolare è stato modificato il ciclo di ottimizzazione aerodinamica, che ha l'obiettivo di massimizzare l'energia prodotta in un anno, AEP. Il metodo di ottimizzazione di *free-form* richiede l'uso del software *XFoil* per calcolare le curve polari dei profili alari al fine di aumentarne l'efficienza e, di conseguenza, l'AEP. Anche l'analisi sul rumore, che è fondata su modelli semi-empirici basati sulla frequenza, necessita l'uso di *XFoil* per caratterizzare lo strato limite che si sviluppa lungo la pala. Richiede, inoltre, l'utilizzo di *Cp-Lambda*, che è un software aero-servo-elistico ad elementi finiti in grado di computare diversi parametri aerodinamic e geometrici usati successivamente dai modelli semi-empirici.

L'analisi predittiva del rumore è stata semplificata al fine di ridurre il tempo computazionale. Inoltre è stata eseguita un'analisi di sensitività per osservare le differenze con il metodo originale. Al fine di ridurre i tempi computazionali, specifiche simulazioni dinamiche sono state introdotte per l'analisi aeroacustica. In precedenza i dati necessari erano acquisiti dalle simulazioni dinamiche con carichi designati che sono eseguite per motivi strutturali e che devono durare 10 minuti secondo le normative. L'analisi, invece, necessita solo di una decina di secondi. Successivamente, il processo è stato inserito all'interno del ciclo aerodinamico e usato al fine di calcolare un vincolo da essere rispettato dalla configurazione ottimizzata. Infine, la robustezza del metodo di *free-form* è stata incrementata aggiungendo un limite sullo spessore minimo che i profili alari possono avere da metà corda al bordo d'uscita. Infatti, le

simulazioni iniziali non sono andate a buon fine a causa della compenetrazione del ventre e del dorso.

I contributi di tre diverse sorgenti di rumore sono stati considerati: rumore dovuto allo strato limite turbolento al bordo di uscita, calcolato secondo il modello TNO; quello causato dal flusso d'ingresso turbolento, calcolato secondo i modelli di *Amiet* e *Lawson*; il rumore dovuto ad un bordo d'uscita non affilato, calcolato secondo il modello di *Brooks, Pope, Marcolini*.

Le nuove implementazioni sono state testate su un generatore eolico di 10 MW di classe 1A. I risultati trovati dimostrano che la riduzione del rumore totale è strettamente dipendente dalla sorgente di rumore predominante. Infatti, il design della pala influenza molto il rumore dovuto ad un bordo d'uscita non affilato e quello generato dallo strato limite turbolento al bordo di uscita, ma non ha un'influenza diretta sul rumore prodotto dal flusso d'ingresso turbolento. Ciò nonostante, le simulazioni preliminari testate sono andate a buon fine e hanno dimostrato la possibilità di introdurre un'analisi aeroacustica predittiva all'interno del processo di progettazione di una turbina eolica.

Contents

List of Figures

List of Tables

Chapter 1

Introduction

In recent years the attention of the world to the climate change has increased exponentially. Sustainability has become an important political topic, which has catapulted the energy production market towards renewable energy sources. Therefore, as it can be seen from Fig. 1.1, also the request of wind turbines has increased, which has had the effect of allocating more funds in this raising sector and of pushing more industry towards the development of improved design methods and, consequently, machines. Of course, the green movement has been a good starting point, but to be a real alternative and, ultimately, replacement of the traditional fossil power plants, wind turbines needs to have comparable performances in terms of efficiency, measured by the cost of energy, CoE, and energy produced. For these reasons, rotor size has become bigger and bigger, trying to generate as much possible power from each machine. Also, studies are ongoing to optimize wind turbine farms and to find better solutions for both onshore and offshore turbines, so that it is possible to fully take advantage of favorable sites.

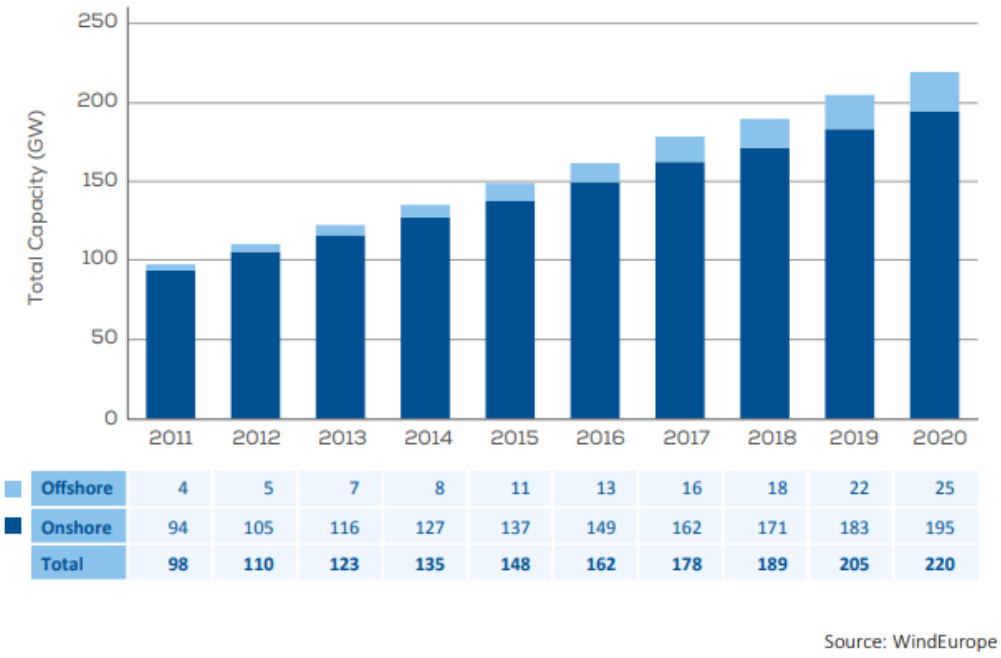

Figure 1.1: Wind energy capacity installed in Europe in the last 10 years [1]

1.1 Reasons behind the work

The increasing number of wind turbines has reduced the optimal places where it is convenient to collocate them. In the future, it is easy to imagine more and more machines positioned near small villages and houses, so it's important to limit the produced noise pollution by acting directly on the design cycle. Wind turbine emissions, indeed, can be really annoying due to their constant disturbance, even if humans are used to much higher sources. Therefore, the goal is to reduce noise amplitude to increase the available sites for wind turbine placement, of course at the expense of machine performances.

Nations have started to introduce norms about the maximum noise producible by wind turbines. The limits are based on the location of the machines on the territory. Some examples are shown in Tab. 1.1, where wind velocities are referred to 10 m height according to IEC61400-11 [2]. Therefore, it is of paramount importance to be able, not only to predict noise emissions of a machine, but also to develop new design cycles that are able to include noise amplitude as a constraint, in order to guarantee that the final configuration is respecting the legal values.

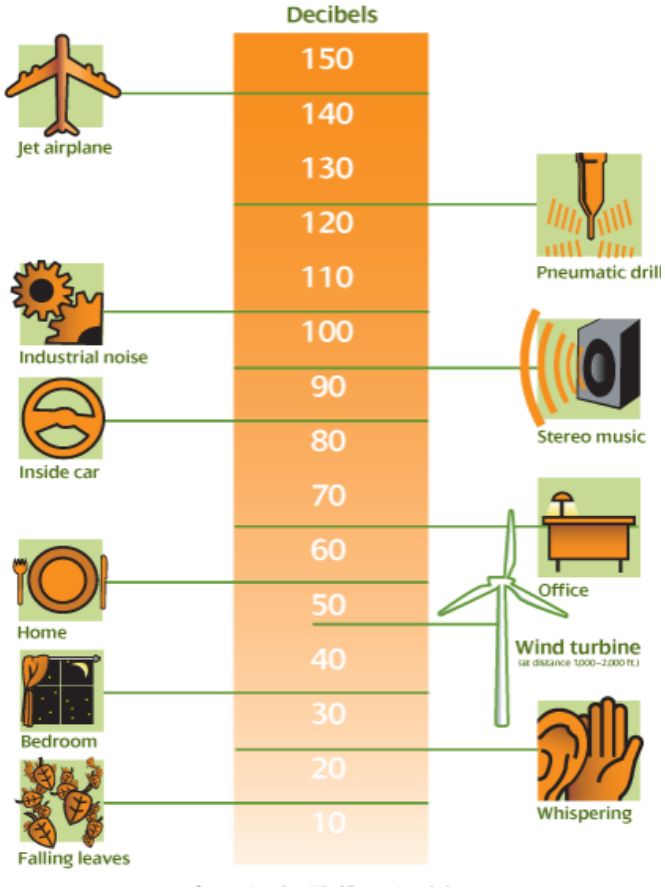

Figure 1.2: Noise emissions comparison between different sources

Country	Regulations or Guideline
Australia	Greater of 35/40 dBA or existing plus 5 dBA
Ontario, Canada	40 dBA to 51 dBA; increasing with wind speed
Denmark	Typically 42 dBA at 6 m/s and 44 dBA at 8 m/s
Germany	35 to 40 dBA at night
Netherlands	41 dBA at night or 47 dBA as annual average
United Kingdoom	Greater of 43 dBA or 5 dBA above existing at night

Table 1.1: Legal norms on wind turbine noise emissions imposed by some countries

At the moment the only way to reduce noise emissions is to act on the control laws governing the turbine, particularly by fixing a maximum tip velocity, which ultimately sets a maximum rotational velocity. This, of course, is a coarse method, since it does not involve any kind of analysis, simply imposing a limit on an important variable that

strongly influences noise, but does not measure it. The present work has the main purpose to surpass this method and to develop a design cycle that is able to quantify the noise amplitude and to automatically adjust the machine to respect the limit imposed, which is a much more precise one. Furthermore, limiting the rotational speed has also a great impact on the maximum energy produced by the machine. For this reason the idea is to act on the geometry of the blade in order to limit noise emissions without decreasing too much turbine performances.

At the beginning of the work, *Cp-Max*, which is an optimization software developed at Politecnico di Milano and Technische Universität München specifically for designing wind turbines, is able to compute a predictive noise analysis, but only after the final configuration is defined, not affecting the design process. The main goal of the present work is, instead, to introduce the aeroacustic analysis tool inside the optimization processes, in particular, inside the aerodynamic optimization of the blades, so that it is possible to limit the emissions. The idea arises by the recent implementation of a *free-form* method introduced by Bolzoni [3]. Now, indeed, the blade geometry can be modified by acting not only on the distribution of chord, twist, as before, but also by changing the shape of the profile along the blade. As will be better explained in chapter 3, previously the shape and the thickness of the profiles along the blade was controlled by a set of prescribed airfoils that could be shifted along the span. Currently, instead, it is possible to change them by acting directly on the shape of the profiles, as better understandable by Fig. 1.3

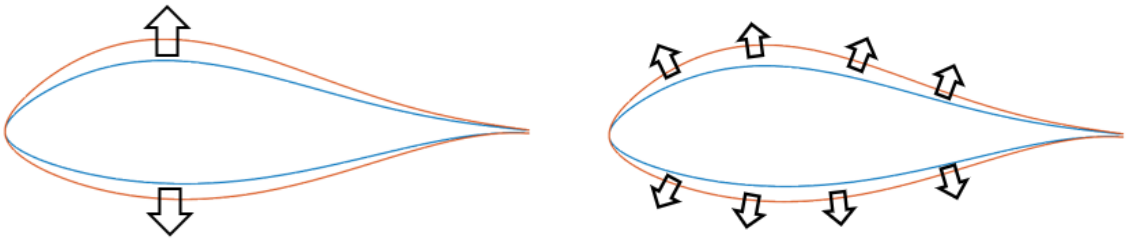

Figure 1.3: How the airfoil shape is modified without or with a *free-form* method

Finally, it is important to underline that, as said, the main purpose of the work is to show the possibility to directly consider noise emissions as constraints inside the design cycle. For this reason, models used must be accurate from a qualitative point

of view, not on a quantitative one. Indeed, the goal is not to design a wind turbine for a real application, so no validation about the quantitative results is performed. This aspect does not diminish the importance of the thesis, since, by being coherent, so by always using the same key parameters, if the models used are qualitative correct, the reduction of noise emissions, which will be hopefully found, can still be considered reliable.

1.2 State of art

1.2.1 Wind turbine design with a *free-form* methodology

A modern approach to wind turbine design consists in the application of system-engineering procedures to the accurate numerical models developed inside multi-disciplinar simulation tools. *Fuglsang et al.* [7] were the first who used macro parameters, like the rotor diameter, as variables of an aeroealstic model developed to optimize small wind turbines by maximizing the CoE. *Bottasso et al.* [61] followed the same idea of implementing a System Design and Optimization procedure by developing a step by step process that optimizes the chord and the twist of the blade together with the thickness of the structural components. In particular, the structural optimization was founded on a set of Design Load Cases, DLCs, that must be recomputed any time the aerodynamic properties are modified. A multi-layer architecture similar to the one used in this work was then presented by *Maki et al.* [8], in which an external optimization conducted on general turbine parameters, such as rated power and rotor speed, is interfaced with two sub-levels to maximize the AEP and minimize the loads. In literature is possible to find, also, other approaches, for example the aero-structural design of a 1.5 MW rotor blade carried out by *Zhu et al.* [9] that was based on a genetic algorithm.

Only in recent years the implementation of a *free-form* method inside the design optimization cycle of a wind turbine has been explored. Many studies, instead, have been performed on the optimization of a standalone airfoil. *Grasso* [10] used an improved version of *XFoil* for the aerodynamic calculations inside an optimization scheme, in order to redesign the shapes of a family of airfoils. He then evaluated their

application for blades in low wind regimes trough a simplified turbine model based on Blade Element Momentum, BEM, formulation. *Zhang* [11] and *Hewitt et al.* [55] developed a condensed parameterization to describe the airfoil shapes, focusing on high geometric fidelity with reduced number of variables. This was then used by *Hansen* [12] to modify three different Delft airfoils by considering the sum of aerodynamic efficiency in a range of angles of attack as performance indicator.

One of the first proposal of an integrated design of the airfoils within a simplified aerodynamic environment was presented by *Sartori* [13]. The idea was then improved by *Bottasso et al.* [14] that completed an aero-structural optimization of the blade in a *free-form* logic. The authors solved a monolithic constrained minimization problem using a Sequential Quadratic Programming optimization procedure, where aerodynamic and structural design variables are calculated simultaneously. They maintained the computational time low by parallelizing the algorithm and by using a BEM model to compute the Cp - TSR envelope and a 2D FEM to evaluate the structural requirements on the spar caps. Results showed promising improvement in turbine performances and matched modern design criteria for large rotor airfoils. *Barret and Ning* [15] investigated the differences between a *free-form* approach, which ideally allows absolute flexibility, and a precomutational one, which is less demanding in terms of variables to be handled and of computational time. The authors, also, showed the outcome changes when *XFoil* was replaced with a CFD simulation to compute airfoil polars. A monolithic optimization was then performed on a simplified model of the NREL 5-MW [56], and included chord and twist distributions, thickness of spar caps and trailing reinforcements.

Finally, *Bolzoni* [3] implemented a *free-form* method inside *Cp-Max*, in particular inside the aerodynamic optimization. By using a Class and Shape Transformation parameterization of the airfoils, he was able to consider the shapes of the profiles as aerodynamic variables. Furthermore, in order to avoid high computational cost, he used *WTPerf*, which is based on a simplified BEM model, to evaluate the aerodynamic performances of the profiles. The maximum thickness of each airfoils is considered as a macro variable to create a link between the profile shape and the structural optimiza-

tion, otherwise the geometry would be fully driven by the aerodynamic optimization. An explanation in details is given in chapter chapter 3.

1.2.2 Noise emissions evaluation

Noise emissions of wind turbines are typically computed using two different approaches in literature: computational aeroacoustics methods, CAA, or semi-empirical methods based on frequency.

CAA methods are numerical techniques based on computational fluid dynamics techniques, which makes them computationally demanding, since they require high spatial and temporal resolution to capture the small and quick fluctuations generated by sound radiations. However, they are able to determinate both noise sources and propagation of sound waves. Direct methods represent the first category of CAA. They are rarely used in practical applications because they couple simultaneous computation of aeroacoustic source region with acoustic propagation to far field, which is very time demanding.

Much more adopted CAA techniques are the hybrid schemes, which compute source near field pressure fluctuations with CFD and then propagates it to the far field through wave equations. The latter have been studied for years. First *Lighthill* [15] gave a formulation of a wave equation rearranging the Navier-Stokes mass and momentum equations and defining a new stress tensor composed of flow convection, shear stress and acoustic propagation. The author then showed that is possible to consider only flow convection for low Mach number. *Curle* [16] extended the theory by including the effects of static solid surfaces on aerodynamic noise. He, also, showed the importance of interaction between turbulent flow and solid boundaries on the generation of sound. This aspect has been studied thoroughly by *Ffowcs-Williams, Hawkings and Hall* [17, 18], which took into account the influence of arbitrary moving surfaces. The latter can be represented as a distribution of monopoles and dipoles, called generally thickness and loading noise. Then, *Farassat* [19, 20] has reformulated the resulting *Ffowcs-Williams and Hawkings*, FW-H, model in time or frequency domain.

These methods have regained interest due to the improvements in computational capacity, which has allowed application of CAA techniques for calculation of noise emissions from both helicopters and wind turbines. *Brentner* [21, 22], developed *WOPWOP*, a ”near real-time” code for helicopter noise computations. *Arakawa et al.* [24] used CFD simulations for the near-field computation and FW-H for far-field propagation to compute noise emissions of a wind turbine.

Semi-empirical frequency methods are used to approximate sound spectra produced by wing sections or by the whole wind turbine. They are the most used tools for noise prediction in the wind energy industry, thanks to their simplicity and rapidity. The starting point of their development is the dependence of sound intensity from the fifth power of the velocity, which was discovered by many studies that have focused on determination of far field noise due to turbulence convecting over an infinitely extended half plane [18, 40, 39].

The first models developed for wind turbine applications were presented by *Lowson* [33]. They are based on very few parameters such as rated power, rotor diameter and tip speed. Improved aerocustic theory allowed to develop more sophisticated noise prediction tools such as the one developed by *Grosveld* [25] or *Glegg* [26], which takes into account contributions of inflow turbulence, turbulent boundary layer - trailing edge and trailing edge bluntness noise. Then in 1989, *Brooks, Pope and Marcolini* [44] built a model based on experimental fitting to compute noise spectra of wing sections. The BPM model is still used nowadays and takes into account five different self-generated noise sources: turbulent boundary layer - trailing edge, laminar boundary layer - vortex shedding, trailing edge bluntness, separation-stall and tip noise. A work conducted by *Lau* [27] has recently improved the model. Another recent model able to study turbulent boundary layer - trailing edge noise has been developed by *Parchen* [38] and is called TNO. This method is not entirely based on empirical considerations, as the BPM model, but uses a detailed boundary layer characterization given by a CFD simulation or by a boundary layer solver, as *XFoil*, in order to compute sound spectra.

Turbulent inflow noise, instead, was initially described by the work conducted by

Amiet [5, 6], which established the basis for computation of noise radiated from a solid surface as a result of incoming gusts or unsteady flow. In his work *Amiet* divided the spectra on a low and a high frequency range. Then, *Lowson* [33] proposed a new approximation for the low band in order to produce more smooth transition between the two ranges. More recently *Guidati et al* [24] developed a model combining a boundary element method with *Amiet* theory, improving the accuracy of the results at the price of a higher computational cost. In order to reduce the computational cost, *Moriarty* [32] designed an empirical correction based on *Guidati* model to include effects of airfoil shape and angle of attack, not included in the original *Amiet* formulation.

Different authors developed tools for noise computation, such as NREL's code *NAFNoise* implemented by *Moriarty* [34] that includes all the mentioned model and computes sound emissions of a 2d wing section. Other codes are for example *SILANT* [36], based on BPM model coupled with boundary layer code *R-Foil* [28], successfully used in the European project Sirocco [30], or the one developed by *Fulglsang* [29] at DTU. In the present work, the tool implemented in *Cp-Max* has been developed by *Sucameli* [4], which is still improving it in actual studies conducted at Technische Universität München. It allows to compute noise analysis for boundary layer - trailing edge, turbulent inflow and trailing edge bluntness noise. The latter is computed following the BPM model, while the other can be computed with different models. Turbulent boundary layer - trailing edge can be calculated with BPM model or with TNO model given by *Howe* [39] or improved by DTU [53]. Turbulent inflow noise, instead, can be evaluated following: full *Amiet* and *Paterson* [5] model, *Lowson* [33] model, *Amiet* model approximated with *Lowson* or *Paterson* [6] theory. Furthermore *NAFNoise* is also implemented and can be used in its full or simplified version.

Chapter 2

Noise analysis models

In this chapter are presented the physical quantities used to measure and describe sound and noise contributions that are taken into account during this work: turbulent boundary layer - trailing edge, turbulent inflow and trailing edge bluntness. Each source is described by a semi-empirical model based on frequency methods that have the advantage of computing the results in brief time, which is fundamental for the purpose and realization of the present work. The models have already been implemented and, even if they are not modified, are here presented for completeness. Additional details can be found in work done by *Sucameli* [4], which developed and tested the code.

2.1 Introduction to sound

Sound is composed of waves, indeed it is generated by rapid and small fluctuations of atmospheric pressure that propagate through a medium as waves. For this reason, sound has an energy content distributed at different frequencies and it can be broadband, if it is important for a big range of frequencies, or tonal, if it involves only a limited range. The most used physical quantity that characterizes noise amplitude is the sound pressure level, SPL, which is measured in dB and does not differ linearly but logarithmically to better suit human hearing perception. Different sources can be summed to find the total value, but it must be noted that due to the logarithmic scale it is not a normal summation and, for example, doubling a sound amplitude produces only a rise of 3 dB.

$$SPL = 10 \log_{10} \left(\frac{p^2}{p_{ref}^2} \right) \tag{2.1}$$

$$SPL_{Tot} = 10 \log_{10} \left(\sum_{i=1}^{n} 10^{0.1\, SPL_i} \right) \tag{2.2}$$

Where p indicates the pressure amplitude and p_{ref} is a reference pressure value fixed at 20 μPa.

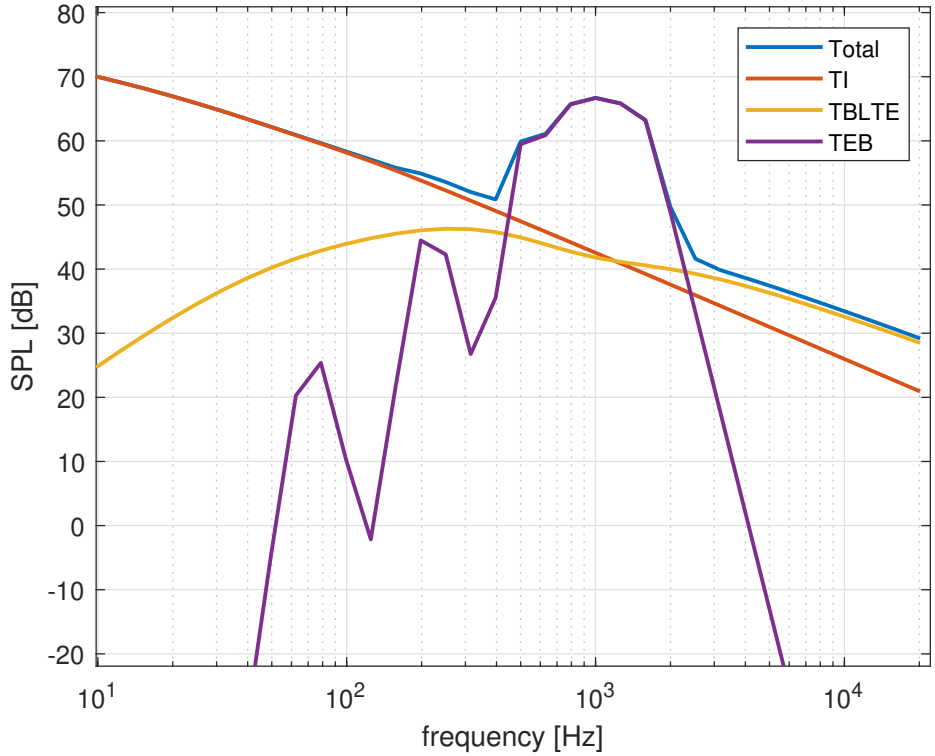

Figure 2.1: Example of total and singular contribution SPL spectra of a wind turbine

Furthermore, SPL is usually given as function of the frequency and it is defined between 20 Hz and 20 KHz, which is equivalent of the human hearing range. Its definition depends on the frequency discretization. Indeed, it is not necessary to analyze sound amplitude for each singular frequency, but bandwidth can be defined. As in the present work, it is often used a 1/3 octave band discretization.

$$f_u = 2^{1/3} f_l \tag{2.3}$$

f_u and f_l represent the upper and lower bound of each interval. From their definitions, it is possible to compute the center frequency, which can be seen in Tab. 2.1, and,

more importantly, the frequency bandwidth:

$$f_c = \sqrt{f_l f_u} = \sqrt{2^{1/3}} f_l \tag{2.4}$$

$$\Delta f = f_u - f_l = f_l(2^{1/3} - 1) = \frac{f_c}{2^{1/6}}(2^{1/3} - 1) = f_c \left(2^{1/6} - \frac{1}{2^{1/6}}\right) \tag{2.5}$$

Sound pressure levels defined in bands can now be related to the power spectral density of a noise spectrum evaluated at a center frequency f_c by multiplying the second for the respective pulsation bandwidth $\Delta\omega = 2\pi\Delta f$:

$$SPL(\omega) = 10 \log_{10} \left(\frac{PSD(\omega)\, 4\pi\Delta f(\omega)}{P_{ref}^2} \right) \tag{2.6}$$

Another important quantity used in the work is the overall sound pressure level, which, as the name suggest, corresponds to the integration of sound pressure level on the whole spectrum:

$$OASPL = 10 \log_{10} \int 10^{0.1\, SPL(\omega)}\, d\omega \tag{2.7}$$

Lastly, humans not only are not linearly sensible to sound, but also perceive it differently based on the frequency of the source. For this reason, in literature exist different filter functions, with A-weighting one being commonly used, Fig. 2.2.

$$R_A(f) = \frac{12200^2 f^4}{(f^2 + 20.6^2)\sqrt{(f^2 + 107.7^2)(f^2 + 737.9^2)}(f^2 + 12200^2)} \tag{2.8}$$

The filter is used to modify the power spectral density of a noise spectrum and to compute the sound pressure level and the overall sound pressure level of a source, which better evaluate how an observer is disturbed by noise emissions.

$$SPL_A(f) = SPL(f) + R_A(f) \tag{2.9}$$

$$OASPL_A = 10 \log_{10} \int 10^{0.1\, SPL_A(\omega)}\, d\omega \tag{2.10}$$

Lower limit	Center frequency	Upper limit
11.2	12.5	14.1
14.1	16	17.8
17.8	20	22.4
22.4	25	28.2
28.2	31.5	35.5
35.5	40	44.7
...	...	...
5623	6300	7079
7079	8000	8913
8913	10000	11220
11220	12500	14130
14130	16000	17780
17780	20000	22390

Table 2.1: 1/3 Octave bands discretization

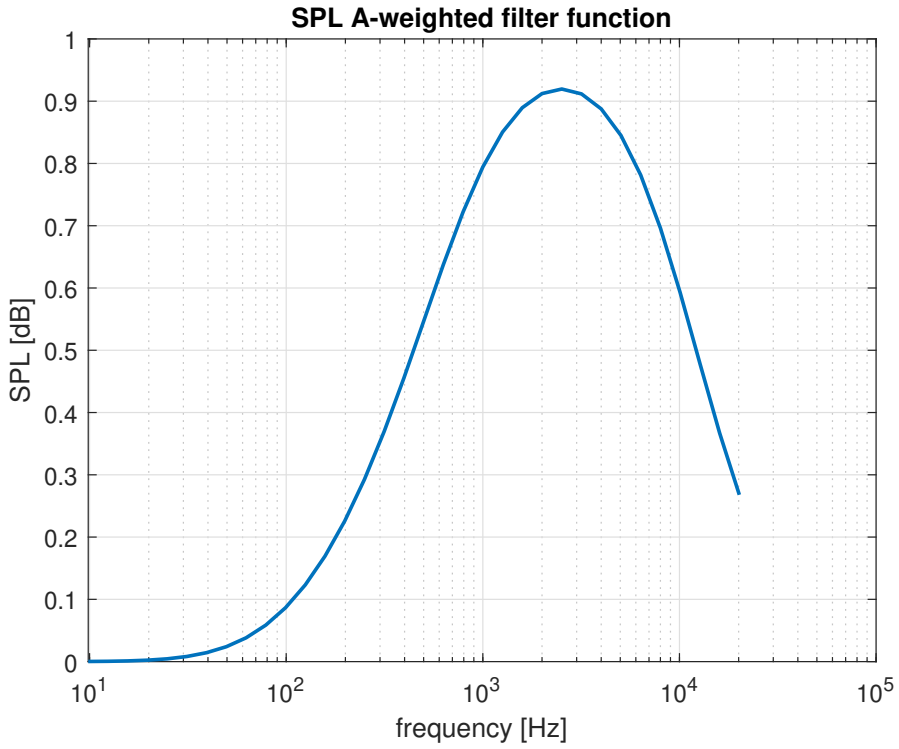

Figure 2.2: SPL spectrum of A-weighted filter function

2.2 Noise sources of a wind turbine

Wind turbine emissions can be divided in mechanical noise, which is generated by friction of the rotating parts of the machine, and in aerodynamic noise, which is created by the interaction between blades and wind. In the present work, only the second one has been analyzed, since the mechanical one does not depend on the geometry of the blades and it can be reduced by carefully designing gearbox, acoustic damping of nacelle and generator. The main aerodynamic sources are presented, following the definitions of *Brooks, Pope and Marcolini* [44]. In particular, only the first three will be considered in the analysis, while the others are here for completeness:

- Turbulent inflow noise, TI, is originated from interaction between blades and incident turbulence: vortices of various size impacting on the airfoil cause an unsteady change in loading conditions that produces a broadband noise spectrum. It is the only aerodynamic source that is not self-produced, since this mechanism strongly depends on the characteristics of incident turbulence, such as vortices extension and intensity of the turbulence. Nevertheless, it is a very important source for which it is not implemented a semi-empirical model that can include the geometry of the blades as a variable. For this reason, it represents the main obstacle in the present work.

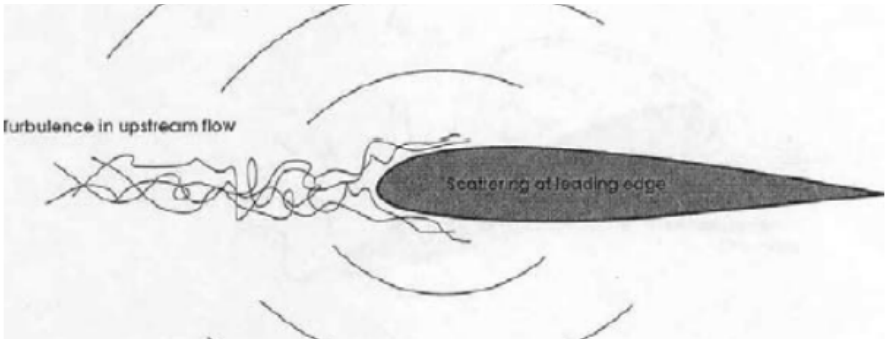

Figure 2.3: Turbulent inflow noise

- Turbulent boundary layer - trailing edge noise, TBLTE, is one of the main sources of airfoil self-noise, namely produced from the interaction of solid airfoils with its boundary layer and near wake. It generates from interaction between a turbulent boundary layer and a trailing edge. Turbulent boundary layers are composed by vortices of various sizes, and their convection over the trailing edge causes

propagation of pressure fluctuations to the wake and then to the far field. Noise spectra produced by this source must be computed on both pressure and suction side and it is often broadband due to the randomness of turbulence.

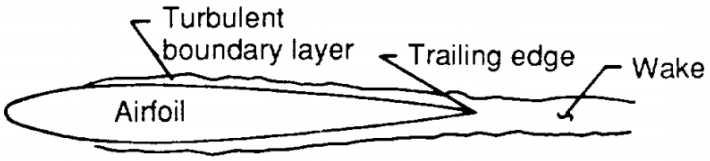

Figure 2.4: Turbulent boundary layer - trailing edge noise [44]

- Trailing edge bluntness noise, TEB, is generated by vortex shedding due to the presence of a thick trailing edge. It is usually tonal, and it strongly depends on the shape of the trailing edge, particularly on the ratio between trailing edge thickness and displacement thickness.

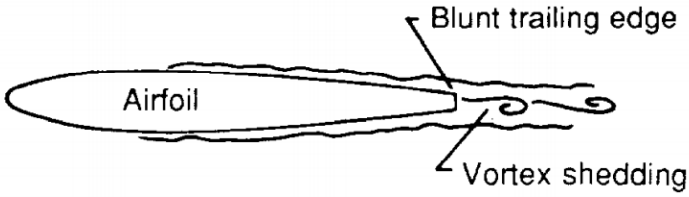

Figure 2.5: Trailing edge bluntness - vortex shedding noise [44]

- Separation - stall noise is produced when a high angle of attack on the airfoil creates wide areas of separation on the suction side of the profile, which sheds vorticity and then broadband noise to the far field. Stall noise it is usually of less importance and, also, knowledge about it is very limited and no predictive model has yet been developed, so it is not included inside the analysis.

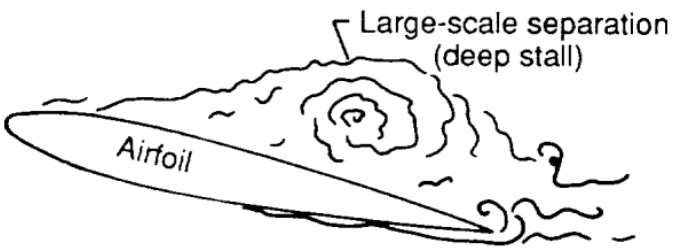

Figure 2.6: Separation - stall noise [44]

- Laminar boundary layer - vortex shedding noise is generated when boundary layer on suction or pressure side remains laminar for most of the surface of the blade, typically for Reynolds numbers close to 10^5, which is lower than the typical range of application of wind turbine. This phenomenon may cause vortex shedding, usually distributed on a narrow band of frequencies.

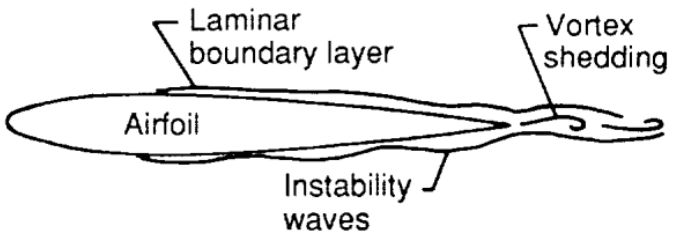

Figure 2.7: Laminar boundary layer - vortex shedding noise [44]

- Tip vortex formation noise is caused by the different pressures between suction and pressure side, which makes the flow three-dimensional around the tip of the blade. This causes the formation of a rotational area, which sheds noise to the far field. For modern wind turbines, tip noise is not considered as an important source of aerodynamic noise due to rounded and sharp blade tips now used.

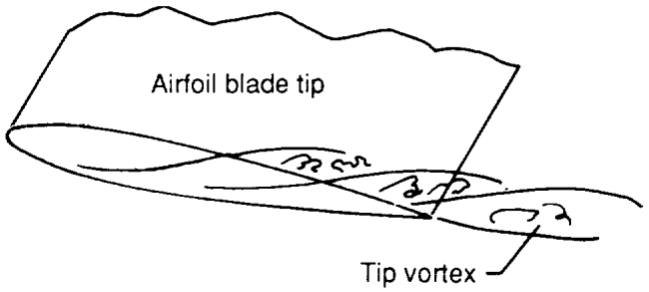

Figure 2.8: Tip vortex formation noise [44]

2.3 Turbulent inflow noise

Turbulent inflow noise is modeled according to the work of *Amiet* and *Paterson* [5, 6]. In their work, the authors developed and validated experimentally a model to predict power spectral density of the noise generated by the interaction of a turbulent flow with the leading edge of the profile, considered as a flat plate of span $2d$ and chord

$2b$, with no thickness nor angle of attack. This aspect is critical for the present work, since the modification of the blade shape has no direct effect on the total emissive noise. Based on previous studies conducted [31], *Guidati* and *Moriarty* [32] developed a method that takes into account the geometry of the blade. However, the full method requires a high computational time, so it does not represent a valid choice for the present work, while its simplified version is embedded inside the NAFNoise code.

In his publication, *Amiet* arrived at the following expression of the far-field power spectral density of the noise:

$$S_{pp}(\vec{x},\omega) = \left(\frac{\omega x_3 \rho_0 b}{c_0 \sigma^2}\right)^2 U_{inf} d\pi \int_{-\infty}^{+\infty} \left[\frac{\sin^2\left(d\left(k_2 + \omega x_2/c_0\sigma\right)\right)}{(k_2 + \omega x_2/c_0\sigma)^2 \pi d}\right] \left|\mathcal{L}(\vec{x}, K_1, k_2)\right|^2 \Phi_{ww}(K_1, k_2)\, dk_2 \quad (2.11)$$

With:

$$\sigma = x_1^2 + \beta^2(x_2^2 + x_3^2) \quad (2.12)$$

$$\beta^2 = 1 - M^2 \quad (2.13)$$

$$K_1 = \frac{\omega}{U_{inf}} \quad (2.14)$$

As they are usually defined in literature: ρ_0 is the air density, ω is the pulsation $2\pi f$, defined depending on the frequency discretization, and c_0 is the speed of sound. Instead, more specific variables are k_1 and k_2, which are the axial, chordwise, and lateral, spanwise, wavenumbers of the turbulence. $\vec{x} = (x_1, x_2, x_3)$ is the position of the observer with respect to the mid chord point of the wing section, in the reference frame, which can be seen in Fig. 2.9. The other terms are $\mathcal{L}(\vec{x}, K_1, k_2)$, defined as the effective lift, and $\Phi_{ww}(K_1, k_2)$, the two-dimensional spectrum.

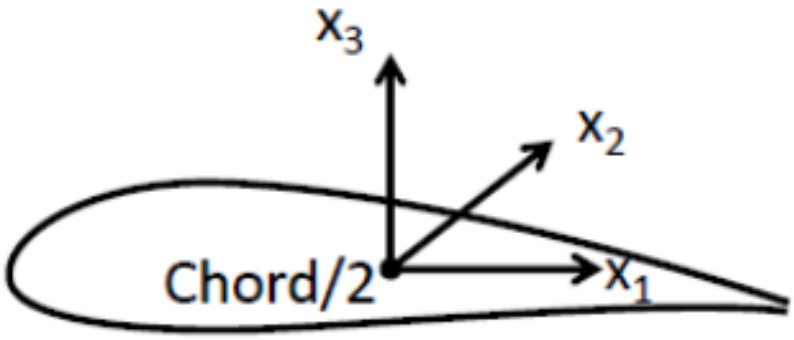

Figure 2.9: Reference system of turbulent inflow noise model [6]

The equation can be simplified by exploiting the fact that, if the semi-span d increases, the quantity in square brackets behaves like a Dirac delta:

$$\lim_{d\to+\infty}\left[\frac{\sin^2(\xi d)}{\xi^2\pi d}\right]\to\delta(\xi) \tag{2.15}$$

Moreover, if the acoustic wavelength λ is much smaller than the airfoil semi-span d, or $MK_1d >> 1$, the equation becomes:

$$S_{pp}(\vec{x},\omega)=\left(\frac{\omega x_3\rho_0 b}{c_0\sigma^2}\right)^2 U_{inf}d\pi\left|\mathcal{L}(\vec{x},K_1,K_2)\right|^2\Phi_{ww}(K_1,K_2) \tag{2.16}$$

$$K_2=\frac{\omega x_2}{c_0\sigma} \tag{2.17}$$

Von Karman spectrum is computed by considering the atmosperic turbulence isotropic:

$$\Phi_{ww}(k_1,k_2)=\frac{4\overline{u^2}}{9\pi k_e^2}\frac{\hat{k}_1^2+\hat{k}_2^2}{(1+\hat{k}_1^2+\hat{k}_2^2)^{7/3}} \tag{2.18}$$

$\hat{k}_i=k_i/k_e$ are the ratios between wavenumber components and the wavenumber of the energy containing vortices k_e, that can be described as a function of the longitudinal integral length of the turbulence length L_t:

$$k_e=\frac{\sqrt{\pi}}{L_t}\frac{\Gamma(5/6)}{\Gamma(1/3)} \tag{2.19}$$

where Γ is the gamma function, a well known mathematical function used in many models:

$$\Gamma(x) = \int_0^\infty e^{-t} t^{x-1}\, dt \tag{2.20}$$

The term $\overline{u_2^2}$ indicates the mean square value of the velocity fluctuations normal to the profile, and can be computed from *Cp-Lambda* aeroelastic simulations. The turbulent length scale L_t is a function of the turbulent flow field and, for wind turbines, it usually depends on the height of the source with respect to the ground, as it will be better described later.

Since the implementation of the full *Amiet* theory is computationally costly, it is often avoided in practical application, but approximate expressions of SPL given by the authors are used. Indeed, in case of observer placed directly above the profile $x_1 = x_2 = K_2 = 0$, the far-field power spectral density is expressed as:

$$S_{pp}(0, 0, x_3, \omega) = \left(\frac{\omega \rho_0 b}{c_0 z}\right)^2 \pi U d |g(\hat{\omega})|^2 \Phi_{ww}(K_1, 0) \tag{2.21}$$

$g(\hat{\omega})$ is the two-dimensional airfoil lift response function, whereas $\hat{\omega} = \omega b / U$ is the reduced frequency. Furthermore, the frequency regime is divided in a low frequency part and in a high frequency one, depending on if the value of the parameter μ is, respectively, smaller or bigger than 0.4.

$$\mu = \frac{M K_1 b}{\beta^2} \tag{2.22}$$

The two parts are approximated differently: the higher one follows the original *Amiet* approximation, while the implementation of the lower one is based on *Lowson* [33] theory.

For the high frequency band, airfoil response function can be defined by approximating it to the limit value for an infinite reduced frequency:

$$\lim_{\omega \to \infty} g(\hat{\omega}) = \frac{-i}{\pi \hat{\omega} \sqrt{M}} \tag{2.23}$$

By inserting, inside the far-field power spectral density equation, this expression and the one for the wavenumber of the energy containing vortices, Eq. (2.19), it is obtained:

$$S_{pp}(z,\omega) = \frac{d}{\pi c_0}\left(\frac{2L}{3\pi z}\right)^2 \frac{\overline{u^2}}{U^2}(\rho_0 U^2)^2 \left[\frac{\Gamma(1/3)}{\Gamma(5/6)}\right]^2 \frac{\hat{K}_1^2}{(1+\hat{K}_1^2)^{7/3}} \tag{2.24}$$

By multiplying the power spectral density by a third octave bandwidth, it is possible to convert the results in sound pressure level:

$$\Delta\omega = 2\pi\Delta f = 2\pi\, 0.232 f \tag{2.25}$$

$$SPL_{high} = 10\log_{10}\left(\frac{4\pi\, 0.232 f S_{pp}}{P_{ref}^2}\right) \tag{2.26}$$

The factor 2 is necessary to convert from double-sided to single-sided PSD, while the subscript high, obviously, is referred to the range of application of the approximation. At this point, the approximated expression can be computed:

$$SPL_{high} = 10\log_{10}\left(\frac{L_t d}{x_3^2} M^5 \frac{\overline{u^2}}{U^2}\frac{\hat{K}_1^3}{(1+\hat{K}_1^2)^{7/3}}\rho_o^2 c_0^4\right) + 10\log_{10}\left(\frac{2\times 0.232\sqrt{\pi}}{\pi P_{ref}^2}\left(\frac{2}{3\pi}\right)^2 \frac{\Gamma(1/3)}{\Gamma(5/6)}\right) \tag{2.27}$$

The second logarithmic term is grouping all known terms, and assumes different values depending on the system of units of measure used. For this reason, it is important to use always the same units of measure and be coherent through the whole implementation. By using S.I. units, as in the present work, the reference pressure is $P_{ref} = 2\times 10^{-5}$ Pa, and the constant is equal to 78.4. Finally, the general expression to be implemented numerically for approximation of high frequency turbulent inflow noise is:

$$SPL_{high} = 10\log_{10}\left(\frac{L_t d}{x_3^2} M^5 \frac{\overline{u^2}}{U^2}\frac{\hat{K}_1^3}{(1+\hat{K}_1^2)^{7/3}}\rho_o^2 c_0^4\right) + 78.4 \tag{2.28}$$

Low frequency approximation is implemented according to *Lowson* theory [33], which is preferred because it assures a smooth transition between the two frequency regimes:

$$SPL_{total} = SPL_{high} + 10\log_{10}\left(\frac{LFC}{1+LFC}\right) \tag{2.29}$$

The term LFC means Low Frequency Correction and, according to *Lowson*, it can be approximated by using in a simple form the Sears function S:

$$LFC = 10S^2 M\frac{\overline{\omega}^2}{\beta^2} \tag{2.30}$$

$$S^2 \approx \left(\frac{2\pi\overline{\omega}}{\beta^2} + \left(1 + 2.4\frac{\overline{\omega}}{\beta^2}\right)^{-1}\right)^{-1} \tag{2.31}$$

All the formulas given above have been obtained thanks to the hypothesis of source positioned directly above the profile. As reported by *Moriarty* [34], this fact may be overcome by taking into account the directivity of sound, which means to consider that the strength of the noise varies depending on the direction of the sound source. Therefore, directivity depends on the relative position between source-observer and generally on noise frequency.

$$SPL_{high} = 10\log_{10}\left(\frac{L_t d}{R^2}M^5\frac{\overline{u^2}}{U^2}\frac{\hat{K}_1^3}{(1+\hat{K}_1^2)^{7/3}}\rho_o^2 c_0^4 D_L\right) + 78.4 \tag{2.32}$$

Term R indicates the distance between source and observer, while D_L is the low frequency directivity:

$$D_L(\Theta_e, \Phi_e) = \frac{\sin^2\Theta_e sin^2\Phi}{(1+M\cos\Theta_e)^4} \tag{2.33}$$

the angles present in the equation are shown in Fig. 2.11.

Turbulent inflow noise is strongly dependent on the turbulent integral length scale L_t and the turbulence intensity $I = u_2/U_2$. In the present implementation, the

solution proposed by *Moriarty* [34] has been adopted and L_t is defined as:

$$L_t(h) = \begin{cases} 0.7h & h \leq 60m \\ 42 & h > 60m \end{cases} \tag{2.34}$$

Other models, as the one proposed by *Zhu* [35] or by *Boorsma* and *Schepers* [36], suggest a different trend, in particular avoiding a constant region after a certain high. It is still unclear which solutions model better this key parameter, as studies are still ongoing.

2.4 Turbulent boundary layer-trailing edge noise

The TNO model is used for the computation of noise generated due to a turbulent boundary layer at the trailing edge. This model was developed by *Parchen* [38] following theoretical studies of *Blake* [37], who derived an expression for the surface pressure fluctuations spectrum thanks to a detailed characterization of the turbulent boundary layer. As reported by *Howe* [39], the power spectral density of the far field noise can be recovered from the previous spectrum. Noise contributions must be computed for both suction side and pressure side of the profile.

As said, the method requires a quite detailed description of the turbulent boundary layer, which is computed using *XFoil*, which has implemented a 2d panel method with boundary layer solver. This approach has already been followed by *Moriarty et al* (NREL) [32] and more recently by *Bertagnolio et al* (DTU) [40, 41]. The software needs as inputs:

- profile shape, given as a set of coordinates
- angle of attack α
- Reynolds number Re
- Mach number M
- profile shape, given as a set of coordinates

- angle of attack α
- Reynolds number Re
- Mach number M

In chapter 3 is described in details how parameters are computed and how the simulations are performed. For the moment, it's important to know that thanks to *XFoil* is possible to recover different quantities at the trailing edge, precisely:

- velocity at the outer edge of the boundary layer U_0
- friction and pressure coefficients, respectively C_f and C_p
- shape factor H_k
- displacement and momentum thickness, respectively δ^* and θ

Then, through the relation given by *Drela*, displacement thickness and momentum thickness are used to obtain an expression of boundary layer thickness δ:

$$\delta = C\left(\theta\left(3.15 + \frac{1.72}{H_k - 1}\right) + \delta^*\right) \tag{2.35}$$

C is the chord of the considered wing section and it is needed because *XFoil* computes θ and δ^* normalized on a unity chord. Moreover, dimensional velocity at the outer edge of the boundary layer is obtained from:

$$U_0^{dim} = U_{inf} U_0 \tag{2.36}$$

Which allows the computation of the friction velocity as:

$$U^* = U_0^{dim}\sqrt{\frac{C_f}{2}} \tag{2.37}$$

Now, the expression of surface pressure fluctuations is presented along with a description of the terms inside it, and how it is possible compute them.

$$P(k_1, k_3, \omega) = 4\rho_0^2 \frac{k_1^2}{k_1^2 + k_3^2} \int_0^\delta L_2(x_2) \overline{u_2^2} \left(\frac{\partial U_1}{\partial x_2} \right)^2 \phi_{22}(k_1, k_3, \omega) \times \phi_m(\omega - U_c(x_2)k_1) e^{(-2|k|y_2)} \, dx_2 \quad (2.38)$$

Indices 1, 2, 3 represent, respectively, the direction: perpendicular to the trailing edge and directed as the mean flow U, normal to the surface of the profile and parallel to the trailing edge, as reported in Fig. 2.10

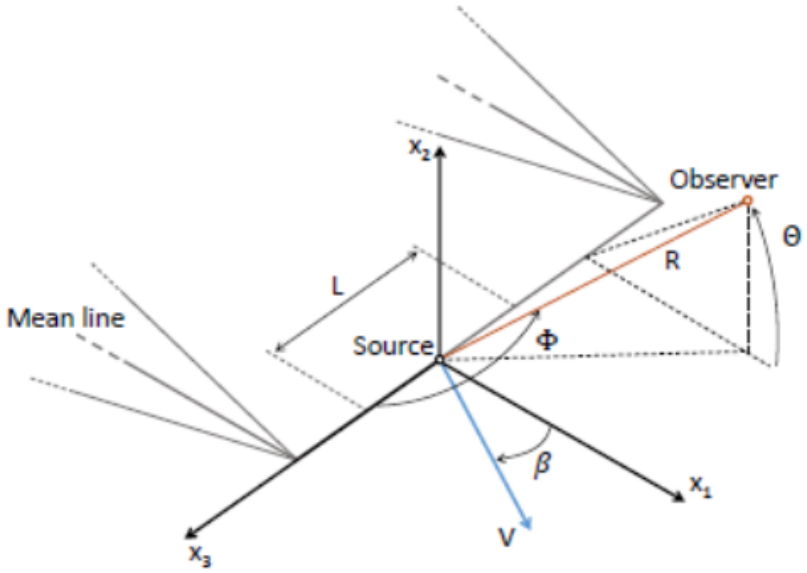

Figure 2.10: Reference system of turbulent boundary layer - trailing edge noise model

The terms in the equation are presented and explained in details:

- Thanks to the Cole law for the wake, it is possible to relate the average speed in the boundary layer, $U_1(x_2)$, to parameters such as friction velocity, viscosity, boundary layer thickness and other constants:

$$U_1(x_2) = U^* \left(\frac{1}{K} \log \left(\frac{U^* x_2}{\nu} \right) \right) + B + \frac{1}{2} \left(1 - \cos \left(\frac{\pi x_2}{\delta} \right) \right) \left(\frac{U_0^{dim}}{U^*} - \frac{1}{K} \log \left(\frac{U^* \delta}{\nu} \right) - B \right) \quad (2.39)$$

The partial derivative $\partial U_1 / \partial x_2$ present in the equation, which represents the

mean shear across the boundary layer, can be obtained by direct differentiation:

$$\frac{\partial U_1}{\partial x_2} = \frac{U^*}{K x_2} + \frac{1}{2} U^* \sin\left(\frac{\pi x_2}{\delta}\right) \frac{\pi}{\delta} \left(\frac{U_0^{dim}}{U^*} - \frac{1}{K} \log\left(\frac{U^* \delta}{\nu}\right) - B \right) \tag{2.40}$$

Where $K = 0.41$ is the Prandtl constant and $B = 5.5$ is a correction factor. Negative friction coefficients, which are typical of separations, cannot be considered by the TNO, so in such cases C_f is set to a very small value, namely 0.0001.

- Convection velocity of vortices U_c is calculated simply as $70\,\%$ of the mean velocity in the boundary layer:

$$U_c(x_2) = 0.7\, U_1(x_2) \tag{2.41}$$

- The absolute value of the wave number directional array, $\vec{k} = (k_1, 0, k_3)$, is then defined as:

$$|\vec{k}| = \sqrt{k_1^2 + k_3^2} \tag{2.42}$$

with k_1 and k_3 computed with respect of pulsation, ω, and relative position between source and observer, $\vec{r}$:

$$k_1(\omega, x_2) = \frac{\omega}{U_c(x_2)} \qquad k_3(\omega, \vec{r}) = \frac{\omega}{c} \cos\Phi \tag{2.43}$$

- Studies conducted by *Bertagnolio et al* [43] allow to take into account the anisotropy of the turbulent boundary layer inside the formulation of the velocity spectrum ϕ_{22}, which is computed as:

$$\phi_{22}(k_1, k_3, \Lambda) = \frac{4\Lambda^2 \beta_1 \beta_3}{9\pi} \frac{(\beta_1 \Lambda k_1)^2 + (\beta_3 \Lambda k_3)^2}{((\beta_1 \Lambda k_1)^2 + (\beta_3 \Lambda k_3)^2 + 1)^{7/3}} \tag{2.44}$$

$$\Lambda(x_2) = \frac{L_m}{0.74683 K} \tag{2.45}$$

Where L_m is the mixing length that is described by the expression of *Schlichting*

[42], which imposes a maximum value around $0.085\,\delta$:

$$L_m = 0.085\delta \tanh\left(\frac{Kx_2}{0.085\delta}\right) \tag{2.46}$$

- From the previous theory, is, also, modelled the integral length L_2, so that it can depend on the anisotropy and also on the frequency:

$$L_2(\omega) = \frac{55\Gamma(1/3)}{108\sqrt{\pi}\Gamma(17/6)}\Lambda\beta_2\frac{3+11(\beta_1\Lambda k_1)^2}{3+8(\beta_1\Lambda k_1)^2}\frac{1}{\sqrt{1+(\beta_1\Lambda k_1)^2}} \tag{2.47}$$

It is clear that the studies strongly rely on the determination of coefficients β_1, β_2, β_3, which have been determined experimentally by the authors by using a NACA 0015 airfoil. At the end, it has been found:

$$\beta_1 = 0.4 \tag{2.48}$$

$$\beta_2 = \gamma^{1/5} \tag{2.49}$$

$$\beta_3 = (2\gamma)^{1/2} \tag{2.50}$$

$$\gamma(y_2) = \frac{\delta}{U^*}\left(\frac{1}{\rho^2\nu}\left(\frac{\partial P}{\partial x_1}\right)^2\right)^{1/3} \tag{2.51}$$

With $\partial P/\partial x_1$ representing the pressure gradient in direction 1, evaluated at the trailing edge.

- The following parameter to be modeled is the vertical velocity Reynolds stress component $\overline{u_2^2}$. The latter is estimated following the approach proposed by DTU [40], so using the turbulent kinetic energy in the boundary layer, computed thanks to the determination of the turbulent viscosity ν_t:

$$\nu_t = l_m^2\frac{\partial P}{\partial x_2} \tag{2.52}$$

$$k_t = \sqrt{\nu_t\frac{\left(\frac{\partial P}{\partial x_2}\right)^2}{C_\mu}} \qquad C_\mu = 0.09 \tag{2.53}$$

$$\overline{u_2^2}(x_2) = \alpha k_t \qquad \alpha = \begin{cases} 0.45 & \text{Suction side} \\ 0.3 & \text{Pressure side} \end{cases} \tag{2.54}$$

- The last quantity to be computed is the moving axis spectrum ϕ_m, modeled as a gaussian distribution:

$$\phi_m(k_1, \omega, x_2) = \frac{1}{\alpha_G \sqrt{\pi}} e^{-((\omega - U_c k_1)/\alpha_G)^2} \tag{2.55}$$

Where:

$$\alpha_G = 0.05 \frac{U_c}{L_2} \tag{2.56}$$

Now, the power spectral density of the far field noise $S_{pp}(\omega)$ for a general observer placed in the space can be computed using the pressure fluctuation spectrum $P(k_1, k_3, \omega)$ as follows:

$$S_{pp}(\omega) = \frac{L}{2\pi R^2} D \int_{-\infty}^{+\infty} \frac{\omega}{c_0 |\vec{k} \cdot \vec{n}|} \frac{P(k_1, k_3, \omega)}{(1 - M_{v,R})^2 (1 - M_{v,1} \sin \Phi)} dk_1 \tag{2.57}$$

In the previous formula: L indicates the span of the wing section considered; R is the distance from the mid-span point of the trailing edge, which corresponds to the source point of noise emissions, to the observer; the versor $\vec{n}$ is parallel to the mean vortex convection velocity U_c; $M_{v,R}$ and $M_{v,1}$ are the components of vortex convection Mach number projected in the observer direction and along the chord, respectively. Finally the last term D, which is the directivity factor of the sound, is computed following *Bertagnolio* [53] model:

$$D = \frac{2 \sin^2\left(\frac{\Theta}{2}\right) \sin^2 \Phi}{(1 + M_r \cos \Theta_c)^3} \tag{2.58}$$

It is important to underline that the angles Θ and Φ are not the same used for the turbulent inflow contribution, but they are taken from work of *Brooks, Pope and Marcolini* [44] and are shown in Fig. 2.11.

Furthermore, in case of observer placed directly above the trailing edge, which means $\Theta = \Phi = 90°$, the equation of the power spectral density can be simplified to (see

[45]):

$$S_{pp}(\omega) = \frac{L}{4\pi R^2} \int_{-\infty}^{+\infty} \frac{\omega}{c_0 k_1} P(k_1, k_3 = 0, \omega)\, dk_1 \tag{2.59}$$

At the end, the integral, obtained combining Eq. (2.57) and Eq. (2.38), to be solved for the computation of trailing edge noise spectrum is the following:

$$S_{pp}(\omega) = \frac{L}{2\pi R^2} D \int_{-\infty}^{+\infty} \int_0^{\delta} 4\rho_0^2 \frac{k_1^2}{k_1^2 + k_3^2} \frac{\omega}{c_0 |\overrightarrow{k} \cdot \overrightarrow{n}|} \frac{1}{(1 - M_{v,R})^2 (1 - M_{v,1} \sin \Phi)}$$
$$L_2(x_2) \overline{u_2^2} \left(\frac{\partial U_1}{\partial x_2} \right)^2 \phi_{22}(k_1, k_3, \omega) \times \phi_m(\omega - U_c(x_2) k_1) e^{(-2|k|y_2)}\, dx_2\, dk_1 \tag{2.60}$$

By considering ϕ_m as a Dirac's delta, exploiting the sampling effect of the moving axis spectrum, it is possible to avoid the integration on k_1:

$$\int_{-\infty}^{+\infty} f(x) \delta(g(x)) = \sum_i \frac{f(x_i)}{|g'(x_i)|} \tag{2.61}$$

Where x_i are the zeros of the function $g(x)$. For $\phi_m(\omega - k_1 U_c)$, it means to evaluate the integrand in $k_1 = \omega / U_c$ and multiplying it by $1/|U_c|$.

It must be underlined that, even if the TNO just described in details is quite sofisticated, the results strongly depend on many factors such as constants, modeling, hypothesis, aeroelastic input and boundary layer data. Again, any validation is out of the scope of the present work, but this aspect has to be taken into account for a real designing project.

2.5 Trailing edge bluntness noise

The trailing edge bluntness – vortex shredding noise is typically a tonal contribution, which is analyzed with the BPM model developed by *Brooks, Pope and Marcolini* [44]. The authors studied the noise emission on a airfoil by analyzing different trailing edge shapes. Particularly, they interpolate results derived for a flat plate edge, solid angle $\Psi = 0°$, and a standard NACA 0012, $\Psi = 14°$. Studies has been performed on other airfoils and it was found that it tends to overestimate the SPL produced by other profiles [54]. It is still used in the work since it strongly depends on the airfoil

shape, particularly on the thickness of the trailing edge blunt and on its ratio with the thickness of the turbulent boundary layer, which makes it very suitable to be lowered by modifying the geometry of the blade. Furthermore, this contribution vanishes for a sharp trailing edge, but manufacturing and structural reasons often limit the minimum thickness value.

The model requires as input: trailing edge solid angle Ψ and thickness h, displacement thickness δ^*, freestream velocity U, Mach number M, span L, distance source-observer R and high frequency directivity $\overline{D_h}$.

$$\overline{D_h}(\Theta_e, \Phi_e) = \frac{2\sin^2\left(\frac{\Theta_e}{2}\right)\sin^2\Phi_e}{(1+M\cos\Theta_e)[1+(M-Mc)cos\Theta_e]^2} \tag{2.62}$$

The convection Mach number M_c is defined as $M_c = 0.8M$; the angles Θ_e and Φ_e are reported in the following figure, taken directly from the original work.

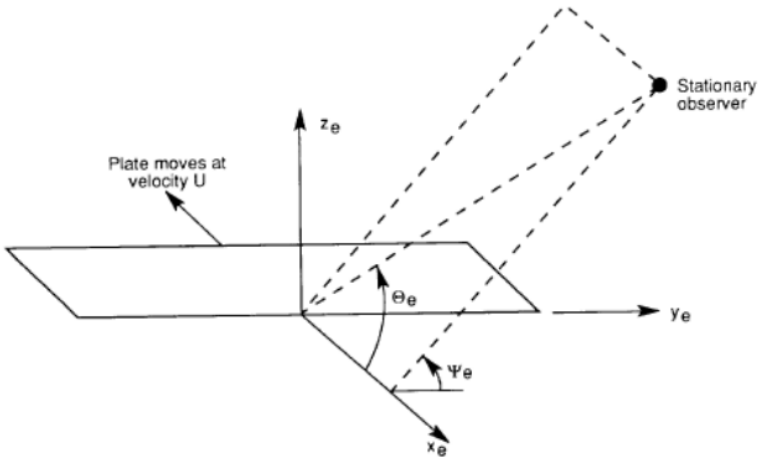

Figure 2.11: Reference system of trailing edge bluntness noise [44]

The authors found that the SPL due to a blunt trailing edge can be computed as:

$$SPL = 10\log\left(\frac{hM^{5.5}L\overline{D_h}}{R^2}\right) + G_4\left(\frac{h}{\delta^*}, \Psi\right) + G_5\left(\frac{h}{\delta^*}, \Psi, \frac{St'''}{St'''_{peak}}\right) \tag{2.63}$$

The first term represents an amplitude scaling determined experimentally, while G_4 and G_5 are the key functions that define spectral characteristics of the contribution. They are both influenced by the solid angle Ψ and by the average boundary-layer

displacement thickness δ^*_{avg}:

$$\delta^*_{avg} = \frac{\delta^*_{pressure} + \delta^*_{suction}}{2} \tag{2.64}$$

Function G_5 also depend on St''', St'''_{peak}, which are the Strouhal number and its peak that can be calculated as:

$$St''' = \frac{fh}{U} \tag{2.65}$$

$$St'''_{peak} = \begin{cases} 0.1(h/\delta^*_{avg}) + 0.095 - 0.00243\,\Psi & h/\delta^*_{avg} \leq 0.2 \\ 0.212 - 0.0045\,\Psi & \\ \hline 1 + 0.235(h/\delta^*_{avg})^{-1} - 0.0132(h/\delta^*_{avg})^{-2} & h/\delta^*_{avg} \geq 0.2 \end{cases} \tag{2.66}$$

In particular, the peak level of the spectrum is defined by function G_4, which can be derived as:

$$G_4\left(h/\delta^*_{avg}, \Psi\right) = \begin{cases} 17.5\log(h/\delta^*_{avg}) + 157.5 - 1.114\,\Psi & h/\delta^*_{avg} \leq 5 \\ 169.7 - 1.114\,\Psi & h/\delta^*_{avg} > 5 \end{cases} \tag{2.67}$$

The shape of the spectrum is, instead, determined by the function G_5 that is computed by interpolating spectra for $\Psi = 0°$ and $14°$ as follows:

$$G_5\left(\frac{h}{\delta^*}, \Psi, \frac{St'''}{St'''_{peak}}\right) = (G_5)_{\Psi=0°} + 0.0714\left[(G_5)_{\Psi=14°} - (G_5)_{\Psi=0°}\right] \tag{2.68}$$

Where:

$$(G_5)_{\Psi=14°} = \begin{cases} m\eta + k & \eta < \eta_0 \\ 2.5\sqrt{1-(\eta/\mu)^2} - 2.5 & \eta_0 \leq \eta < 0 \\ \sqrt{1.5625 - 1194.99\,\eta^2} - 1.25 & 0 \leq \eta < 0.03616 \\ -155.543\,\eta + 4.375 & 0.03616 \leq \eta \end{cases} \tag{2.69}$$

$$\eta = \log\left(\frac{St'''}{St'''_{peak}}\right) \tag{2.70}$$

$$\mu = \begin{cases} 0.1221 & h/\delta^*_{avg} < 0.25 \\ -0.2175(h/\delta^*_{avg}) + 0.1755 & 0.25 \leq h/\delta^*_{avg} < 0.62 \\ -0.0308(h/\delta^*_{avg}) + 0.0596 & 0.62 \leq h/\delta^*_{avg} < 1.15 \\ 0.0242 & h/\delta^*_{avg} \geq 1.15 \end{cases} \tag{2.71}$$

$$m = \begin{cases} 0 & h/\delta^*_{avg} \leq 0.02 \\ 68.724(h/\delta^*_{avg}) - 1.35 & 0.02 < h/\delta^*_{avg} \leq 0.5 \\ 308.475(h/\delta^*_{avg}) - 121.23 & 0.5 < h/\delta^*_{avg} \leq 0.62 \\ 224.811(h/\delta^*_{avg}) - 69.35 & 0.62 < h/\delta^*_{avg} \leq 1.15 \\ 1583.28(h/\delta^*_{avg}) - 1631.59 & 1.15 < h/\delta^*_{avg} \leq 1.2 \\ 268.344 & h/\delta^*_{avg} \geq 1.2 \end{cases} \tag{2.72}$$

$$\eta_0 = -\sqrt{\frac{m^2\mu^4}{6.25 + m^2\mu^2}} \tag{2.73}$$

and

$$k = 2.5\sqrt{1 - \left(\frac{\eta_0}{\mu}\right)^2} - 2.5 - m\eta_0 \tag{2.74}$$

Finally, the spectrum $(G_s)_{\Psi=0^\circ}$ is obtained by computing the same equations just described for $(G_s)_{\Psi=14^\circ}$, but replacing (h/δ^*_{avg}) with $(h/\delta^*_{avg})'$.

$$\left(\frac{h}{\delta^*_{avg}}\right)' = 6.724\left(\frac{h}{\delta^*_{avg}}\right)^2 - 4.019\left(\frac{h}{\delta^*_{avg}}\right) + 1.107 \tag{2.75}$$

As said, BPM model was developed by interpolating experimental results on a NACA 0012 profile, whose chord was of nearly 61 cm, with trailing edge thicknesses of few millimeters. In the turbine considered in the work, the chord is in order of meters and the thickness of centimeters. For these reasons, it is easy to understand that the model is not the most suitable and future studies and experiments will develop a more adequate semi-empirical model. Nevertheless, the variables used by the authors are effectively acting on the noise emissions and in the present work the main goal is to show that by acting on them is possible to reduce the amplitude of this contribution.

Chapter 3

Optimization tool description

The chapter has the main goal to briefly described *Cp-Max*, which is the optimization software used during the work. First, its nested structure is described to let the user understand the main logic that there is behind the code. Then, the aerodynamic module and the structural one, which are the two main blocks of the tool, are illustrated, with particular attention on the first one, which will be then modified in order to reach the goal imposed. It is especially explained in details how the *free-form* method is implemented, since the shape of the airfoils is the most influencing parameter for noise emissions.

3.1 *Cp-Max*

The *Code for Performance Maximization* is a consolidated multi-disciplinary design suite, developed specifically for wind turbine applications, that works inside *Matlab* framework and that is able to call different software during its processes. In particular, the main one is *Cp-Lambda*, that stands for *Code for Performance, Loads, Aero-Elasticity by Multi-Body Dynamic Analysis*, an aero-servo-elastic simulation software which is based on the multibody method adapted for wind energy applications by *Bottasso* [47, 48]. In this way the user can choose how to assembly the machine, by selecting the elements from a furnished library that includes beam models, actuators, rigid bodies, joints and sensors, and also to perform simulations at the wanted level of detail. Moreover, beams are described by their 6×6 stiffness matrix, while aerodynamics is modeled by lifting line theory that, although being a simplified model, is able

to describe accurately the loading condition on the rotor. Furthermore, it is possible to characterize the wind time history acting on the model during aeroelastic simulations. Turbulent wind grids can be generated by the software *Turbsim* [50], which can take as input information such as turbulence intensity, mean speed, wind shear and it can generate a wind grid accordingly. The results of the simulation are collected in output files and depend on the sensors used, which can be placed in any element or position of the wind turbine model and can be of various type, depending on the quantity to be measured.

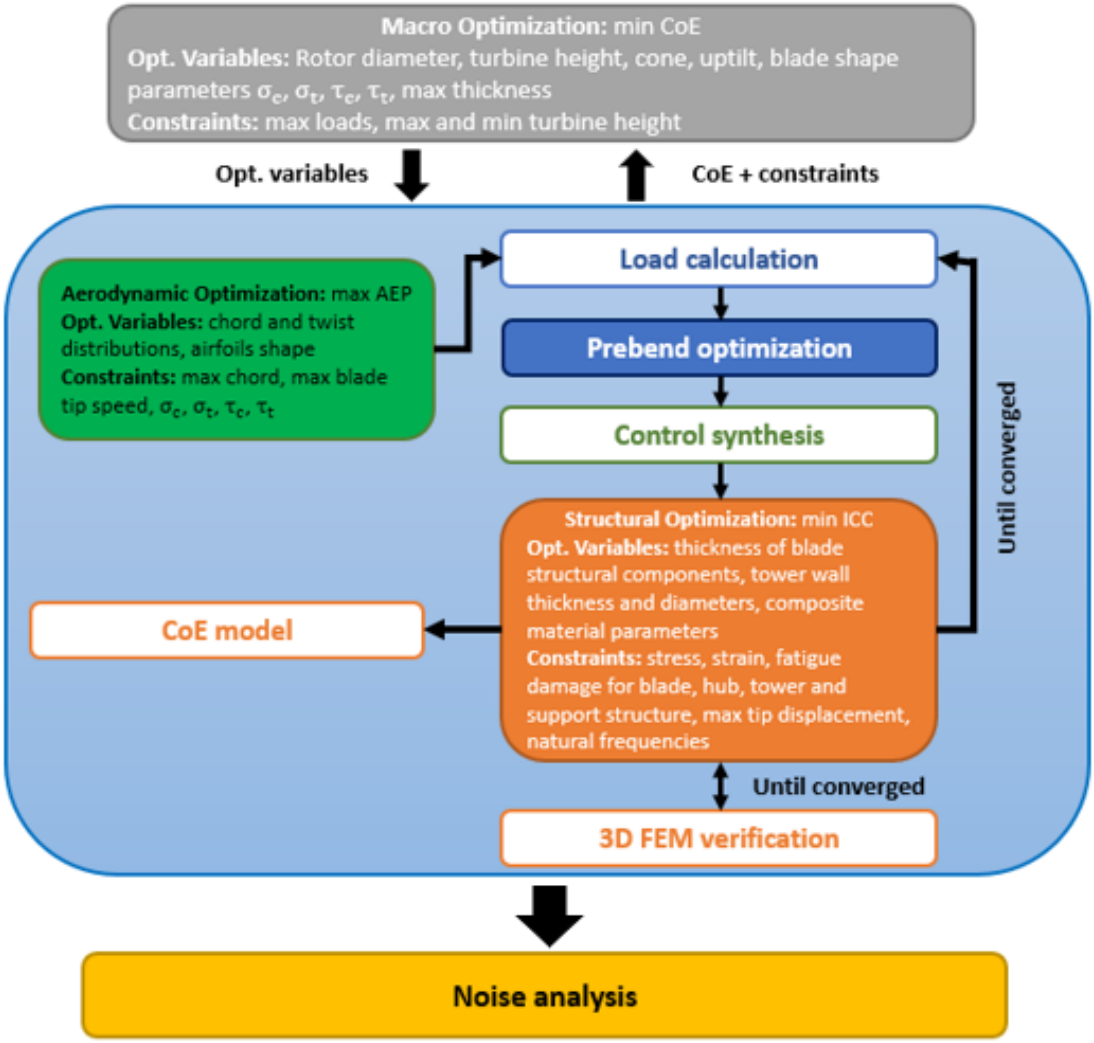

Figure 3.1: Architecture of *Cp-Max*

This method guarantees *Cp-Max* a realistic approach to the analysis of the machines and, more importantly, lot of flexibility, which is a key aspect of the code and that is further magnified by the strategy and the structure of the tool. As said, the design

of a wind turbine is a multidisciplinary optimization problem, which makes impossible to solve the whole problem in one step by formulating a single system that includes all the variables and constraints. For this reason, the process, which is automatically performed, is controlled by an outer Macro Design Loop, MDL, whose variables are a set of macro preliminary parameters that influence the whole wind turbine behavior, and then subdivided in more specific submodules. Indeed, *Cp-Max* has a nested architecture, as it can be seen in Fig. 3.1, in which every module performs a gradient-based optimization whose variables are the sub-set of the design parameters that influence most the merit function, which is specific for each module. For example the index of merit of the aerodynamic block is the AEP, annual energy production, and the variables associated are the distributions of chord, twist, thickness and the shape of the airfoils, while thicknesses of the structural components are not considered since they have little to none impact on the aerodynamic performance.

The array of the global design variables contains fundamental features of the wind turbine and has a significant impact on the whole design and on the CoE, Cost of Energy, computed according to the *INNWIND* model [46]. Every perturbation of one of them requires the code to compute a new global cycle, rerunning every submodule. In the latter, global variables are frozen and considered as constraints. As the CoE is the most effective indicator of a successful project, it suits well for guiding the MDL, whereas AEP and ICC, Initial Capital Cost, are selected respectively for the Aerodynamic and Structural inner Design Submodules, ADS and SDS, since they are two of the most influencing quantities of the CoE. In this way it is possible to split the optimization problem in multiple subproblems without losing the MDL final goal, which is to find the best optimal design solution.

Another advantage of the nested architecture is that variables and modules can be activated and disabled independently by the user, which is of fundamental importance in the first stage of the optimization or during the development of the code, since it allows the user to understand the trend of the optimization and how parameters and processes influence the final design. Moreover, in this way it is possible to introduce different tools to increase the level of detail of the optimization, as a 3D finite element

simulation, or to compute specific analysis, as it is the noise one. Also, since the code is developed in *Matlab* framework, it is very easy to pause the computation during the optimization to check the provisional results or to test the correct implementation of a new part.

A clean formalization in the form *Outputs* = $Function$ (*Inputs*) of the algorithm structure in the general macro-design case can be the following:

$$
\begin{aligned}
COE^* &= \min_{p_g}(\textit{ComputeCOE}(p_a, p_s, p_g, D)) \\
(p_a^*, AEP^*) &= \textit{MaxAEP}(p_a, p_s, p_g, D) \\
(r_{laws}^*) &= \textit{CreateControlLaws}(p_a^*, p_s, p_g, D) \\
(p_s^*, ICC^*) &= \textit{MinICC}(p_a^*, p_s^*, p_g, D, r_{laws}^*) \\
AEP^* &= \textit{UpdateAEP}(p_a^*, p_s^*, p_g, D, r_{laws}^*) \\
COE &= \textit{CostModel}\,(AEP^*, ICC^*, p_a^*, p_s^*, p_g, D)
\end{aligned}
\tag{3.1}
$$

Each design parameter is collected in different input arrays and divided on whether it is aerodynamic p_a, structural p_s, global p_g or belong to the parameters D, which are fixed during the whole optimization process, and are turbine characteristics such as rotor overhang, electrical rated power, class, and simulation options like the list of DLCs, Design Load Cases, selected. In particular, the global variables are: the rotor diameter, turbine height, cone and uptilt angle, blade solidity σ and tapering τ calculated with respect to the chord and thickness and, in case of active *free-form* method, the maximum thickness of each airfoil. The optimal combinations coming out at every stage are labeled as starred conditions. The prebend module is left out from this formulation, since it is not used in any part of this work, while the regulation strategy r_{laws}^* is computed after having define the aerodynamic properties of the blade and according to the chosen type of controller, for example an Integral Linear Quadratic Regulator as in the present work. Now the submoules are described, with particular attention for the ADS, which will be modified. The interested reader can see *Sartori* [51] for a complete and precise description of each blocks.

3.2 Aerodynamic optimization

The aerodynamic module has the main goal of maximizing the AEP through the variation of the distributions of the twist, chord and, in case the *free-form* method is inactive, thickness. The last, when a *free-form* strategy is adopted, as in the present work, is no more an aerodynamic variable while, of course, the shape of the airfoils is. Indeed, to be able to link the optimization of the profiles also to the SDS, which is key to obtain a final configuration that is optimized not only from the aerodynamic point of view, the maximum thickness of each profile is considered a global variable. The same is done for the optimization of the chord distribution, where the solidity is a macro parameter that makes the structure influence the final solution and achieve the best compromise between all the aspects. This is due to the multi-layer architecture of the code, in which the aerodynamic module performs its optimization without any feedback on the structural side of the blade, which is kept frozen. The macro parameters containing information about the blade geometry are enforced here as constraints, in order to maintain the feasibility of the solution and creating a virtual bridge with the macro design loop.

The AEP is the chosen parameter to maximize because it evaluates the performance of a wind turbine in a specific site, by coupling the curve of produced power, which depends on the wind speed, with the expected wind speed of site, so that the machine is optimized for its real operating conditions.

$$AEP = 8760 \, \frac{hours}{year} \int_{V_{in}}^{V_{out}} P(V) f_w(V) \, dV \tag{3.2}$$

The probability density function of the hourly mean wind speed is computed by a Weibull distribution, in which is usually fixed k = 2 and where C is the scale factor containing the average wind of the site.

$$f_w(V) = \frac{k}{C^k} V^{(k-1)} e^{-\left(\frac{V}{C}\right)^k} \tag{3.3}$$

Of course, the algorithm has to act on the power curve to find the optimum solution, so, after the blade geometry has been defined, for every iteration the code computes

an estimation of the aerodynamic performances. The latter are calculated through the evaluation of the power coefficient C_p at given pitch angle and TSR, Tip Speed Ratio, with this one being a direct measure of how much the relative wind is parallel to the rotor plane. Then the final power curve is generated adopting a classical regulation strategy for pitch-regulated, variable wind turbine, which in the present work is based on a LQR integral controller. Due to the use of the *free-form* strategy, the computation time required by the module is quite high. For this reason, it has been implemented the possibility to use, instead of *Cp-Lambda*, *WTPerf*, which is a lighter software with a simpler rigid BEM, Blade Element Momentum, formulation. This can be done due to the nature of the simulation inside the aerodynamic module, which, as said, are performed for low wind speeds, typical of wind turbines, and for imposed set of pitch angle and TSR. The tool introduced is a good compromise in the prospective of this work, since it adopts a refined BEM with the possibility of adding various corrections accounting for blade tilt and precone, hub and tip losses, yaw misalignment and skewed wake swirl. What is not supported in this formulation is the possibility of accounting for loss in power due to blade flexibility and, more importantly, the study of prebent blades, as there is no possibility of modeling built-in deformations of the rotor plane. However, the first one is still considered in structural module and it is, ultimately, influencing the CoE. Furthermore, the introduction of a new constraint on noise emissions increases a lot the computational time, as it will be better explained in the following chapter, so compromises have to be accepted in sake of a feasible algorithm.

It's important to highlight how the aerodynamic variables are described and modified by the code. Chord and twist distributions are managed by piece-wise cubic hermite interpolating polynomials, in which the number of poles and their position along the blade span are chosen by the user. Their variation is then controlled through the station values: the optimized poles are multiplied by a percentage gain before interpolating, forming a sort of bump function affecting only the portion of the blade delimited by the previous and following variable positions. A detailed explanation can be found in the work of *Gualdoni* [49]. Of course, a high number of active stations permits a finer optimized distribution, but it must be kept in mind that the number of variables

added at the optimization corresponds at the number of active poles, which increases the computational time.

The thickness distribution, instead, was managed by shifting along the blade span a fixed number of airfoil stations for which it was known the shape and the maximum thickness relative to the chord. It is clear that before the *free-form* method was introduced, also the profiles of the blade depended by where the stations were defined. On contrary, when the *free-form* method is active as in the present work, the position of the airfoil stations is fixed, while the shape can be fully changed by directly acting on the profiles, which were previously frozen.

For what concerns the shape of the airfoils a CST, Class-Shape function Transformation, is used to parameterize the profiles. It is a recently introduced parametrization, first proposed by *Kulfan* [52], able to accurately describe aerodynamic shapes through regular analytic functions. This regularity capability makes it a powerful tool for optimization purposes, with proven effectiveness when included in a gradient-based algorithm [55]. This solution was found to be the best compromise between:

- Feasibility, directly related to the minimum number of degrees of freedom required to accurately describe a target airfoil
- Completeness of the design space covered by the number of active parameters
- Orthogonality, guaranteeing that each airfoil shape corresponds to a specific set of unique parameters
- Robustness, to avoid faulty airfoil or unfeasible geometries that could cause numerical errors and convergence problems

From a mathematical point of view, airfoils are expressed in polar coordinates normalized respect to the chord, with suction and pressure surfaces described independently by the following:

$$\xi(\phi) = C(\phi) \cdot S(\phi) + \phi \cdot \Delta\xi_{_{TE}} \tag{3.4}$$

where $C(\phi)$ and $S(\phi)$ are respectively called *Class* and *Shape* functions, while $\xi_{_{TE}}$ is

the adimensional thickness of trailing edge. The latter is considered symmetric, since, through a polar representation, it can be described in this way for almost every airfoil. For this reason, the trailing edge values of pressure and suction side are identical and can be recovered by simply dividing in half the adimensional thickness:

$$\Delta\xi_{TE} = \frac{\xi_{TE}}{2} \tag{3.5}$$

The geometries that the transformation is able to generate is mainly decided by the *Class* function, which, also, defines how the parametrization describes the airfoils at both ends. To be able to produce typical subsonic profiles with pointed trailing edge and rounded nose, which is mainly reconstructed by the square root, the function is defined as:

$$C(\phi) = \sqrt{\phi}\,(1-\phi) \tag{3.6}$$

The *Shape* functions are responsible for the regularity, uniqueness and completeness of the profile shape and they include the actual design variables. They are described by a special polynomial function built with a linear combination of weighted Bernstein basis polynomials of degree n, $S_{i,n}$, which are based on the binomial coefficient, $\binom{n}{i}$:

$$S(\phi) = \sum_{i=0}^{n} A_i S_{i,n} \tag{3.7}$$

$$S_{i,n}(\phi) = \binom{n}{i}\phi^i(1-\phi)^{n-i} \tag{3.8}$$

Once the *Class* is chosen, CST parametrization depends only on the $n+1$ weights of the basis polynomials. The influence of each weights A_i can be seen from Fig. 3.2, where the product between the *Class* function and each singular *Shape* one is shown. As it can be seen, A_0 is essentially the only one that defines the leading edge shape, while, as the order increases, the weight impacts mostly the trailing edge.

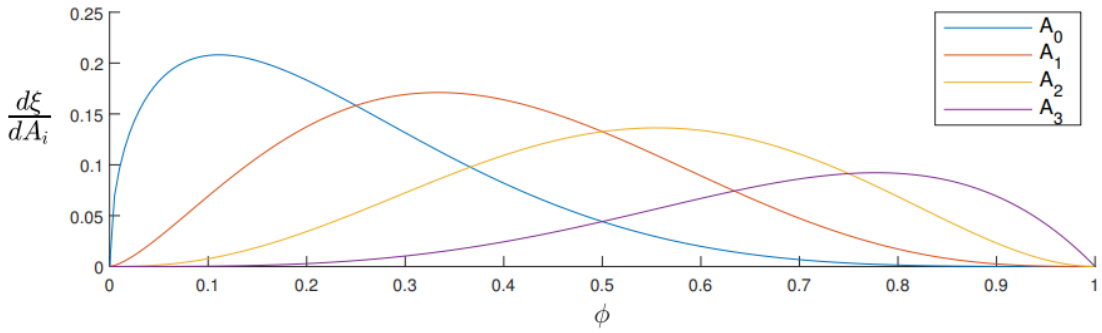

Figure 3.2: Functions multiplying the respective weight in a 3^{th} order CST [3]

The shape is then reconstructed thanks to a simple identification procedure founded on a gradient-based unconstrained optimization method, where the performance index to be minimized is the summation of the ξ-coordinates errors. The problem can be cast in the following form:

$$\min_p J(p),$$

$$J(p) = \sum_i \xi_i^{err}$$

$$= \sum_i |\xi(\phi_i) - \xi_{CST}(\phi_i)| \tag{3.9}$$

with the array $p = [A_0^{ss}, ..., A_n^{ss}, A_0^{ps}, ..., A_n^{ps}, \Delta\xi_{TE}]$ containing all the degrees of freedom.

As *Bolzoni* [3] showed to be the best choice, the order of the CST parametrization n has been fixed at 3. It is a key parameter to be chosen with care, since a CST with very small n reduces the overall stability and robustness of the code due to the higher influence on the overall geometry. Moreover, a low order parametrization, also, limits the design space that can be explored. Instead, choosing a higher-order polynomial increases the accuracy in replicating the original given shape, but it rises, also, the computational time. Furthermore, it decreases the sensitivity of the geometry to each parameter, which may cause serious difficulties to the optimizer during the computation of the gradients. As said, the number of degrees of freedom, so of variables for the aerodynamic cycle, used to describe an airfoil depends on the order

of parametrization chosen:

$$N_{d.o.f} = 2N_{weights} + N_{_{TE}} = 2(n+1) + 1 \tag{3.10}$$

Which means, of course, that in the present work, where $n = 3$, each airfoil to be optimized adds 9 variables to the aerodynamic cycle.

Another important aspect is that the user can choose which airfoils activate to modify their shape with the *free-form* method, which is important to reduce the computational time, since the contribution of the first part of the blade to the power produced is close to none and the geometry of the airfoils is mainly guided by structural and manufacturing reasons. The last aspect to underlined is that the code recognizes if two or more airfoil stations are originally described by the same airfoil, and it modifies them in the same way, as they are linked. This is done to obtain the most from the algorithm. Indeed, even if the solution would be more accurate if airfoils are treated independently, this would increase the computational time, while in this way two or more airfoils are modified at the cost of one. Furthermore, as it is easy to understand, same airfoils are used only at the tip of the blade, where the conditions are similar and the profiles are, already, fully transformed from a cyclical shape to a much more aerodynamic one.

To aerodynamically optimize the airfoils, *XFoil* and a *Viterna-Corrigan* method [58] are used to evaluate the aerodynamic performances of the profile at a fixed Reynolds, particularly their polar curve and efficiency, which are then used to compute the new AEP of the turbine. Indeed, due to the change of the airfoil geometry during the process, is not feasible to use real data coming from experiment when adopting a *free-form* strategy. Previous literature showed that, by combining the two aforementioned tools, an efficient and reliable method [59, 60] is possible to fully characterize the aerodynamic properties in the wide range of angles of attack required. The process starts by computing a *XFoil* viscous calculation in which only the Reynolds number and the airfoil paneling settings are required, since it is neglected the compressibility correction due to typical working Mach number lower than 0.3 for wind turbines. The polar curve is computed for angles of attack between -20° to 20° and then extended

to the $\pm 180°$ range with the *Viterna* model, which basically uses a flat plate analogy in order to extend the aerodynamic data from the post-stall region to the needed domain. At the end *WTPerf* uses a refined BEM to evaluate the performances of the blades and then the gradient based optimization can modify the blades accordingly to increase the AEP, while respecting the constraints imposed.

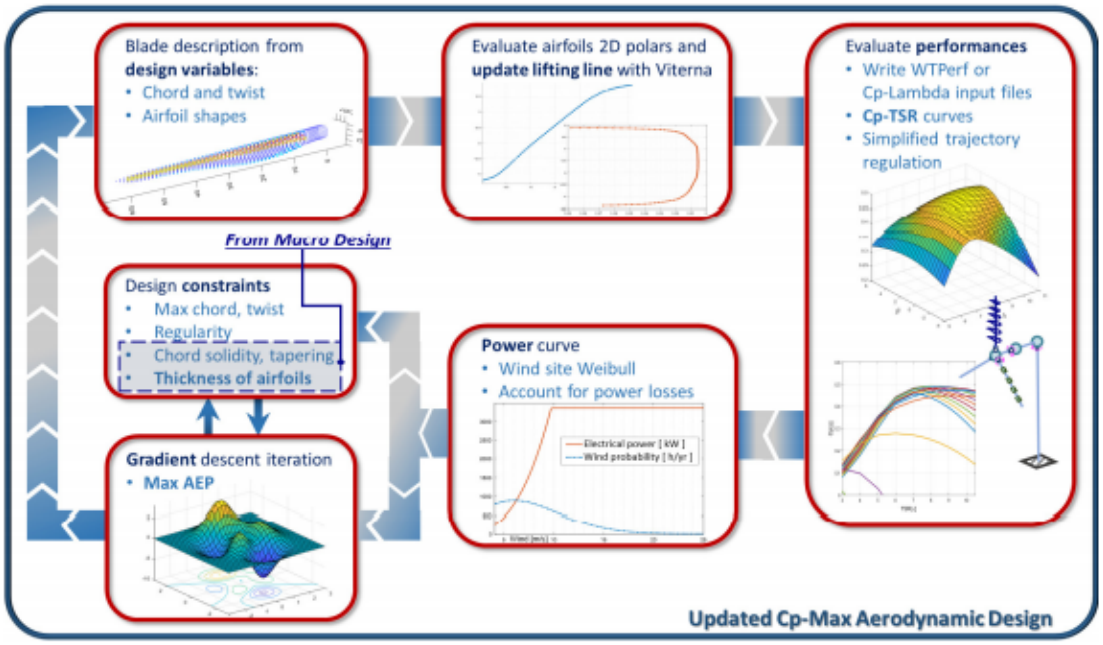

Figure 3.3: Architecture of the aerodynamic optimization cycle [3]

The main drawback of the method is the inability of *XFoil* to correctly describe the stall part of the airfoils, which is often overestimated, with the consequence of even bigger errors in the extended *Viterna* data. Nevertheless, since stall happens for high angles of attack, this aspect is not so relevant in aerodynamically designing the final part of the blade. Also, it must be noted that the aerodynamic data will be computed with the same procedure during both the optimization process and the initialization. Indeed, by being coherent through the whole optimization, it is possible to eliminate systematic errors in performances evaluation.

3.3 Structural optimization

The structural model has been only used during the simulations and not modified, so only a brief description is here presented. Extended details of the original structural

design are explained by *Bottasso* [61]. First of all it's important to define the geometry of the sectional structure, which is designed with three closed cells, with the main one being the central spar box, and composed of panels characterized by their position, function and material distribution:

- shell panels maintain the external shape and absorb torsional loads thanks to triaxial fibers;
- shear webs carry the shear loads and, also, reduce the free-length of the cell to retard the onset of buckling phenomena;
- spar caps bear most of the flapwise bending, being the main contributor to the out-of-plane stiffness;
- leading and trailing edge reinforcements help provide in-plane stiffness to the rotor and take care of edgewise loads.

The position of the sectional element can be seen in Fig. 3.4, where it is represented, also, their lamination sequence accounting for the correct staking of the single layers, so that each element has unique structural properties specific for their functions. The latter are added to the model with the finite element cross-sectional analysis code for *ANisotropic Beam Analysis*, *ANBA*, implementing the theory of *Giavotto et al.* [62]. The tool needs as input the sectional description, in terms of panels, and gives as output the 6×6 stiffness matrix, the mass and inertial properties with the location of the fundamental structural points, so that it is possible to consider the anisotropy of composite materials used in modern wind turbine rotors. The software, thanks to a dedicated model, takes into account, also, the parasitic masses, which correspond to elements necessary for reasons different from the structural ones and that have an impact on the frequencies and displacement of the blades, for example the balsa wood core for sandwich panels used to avoid buckling phenomena.

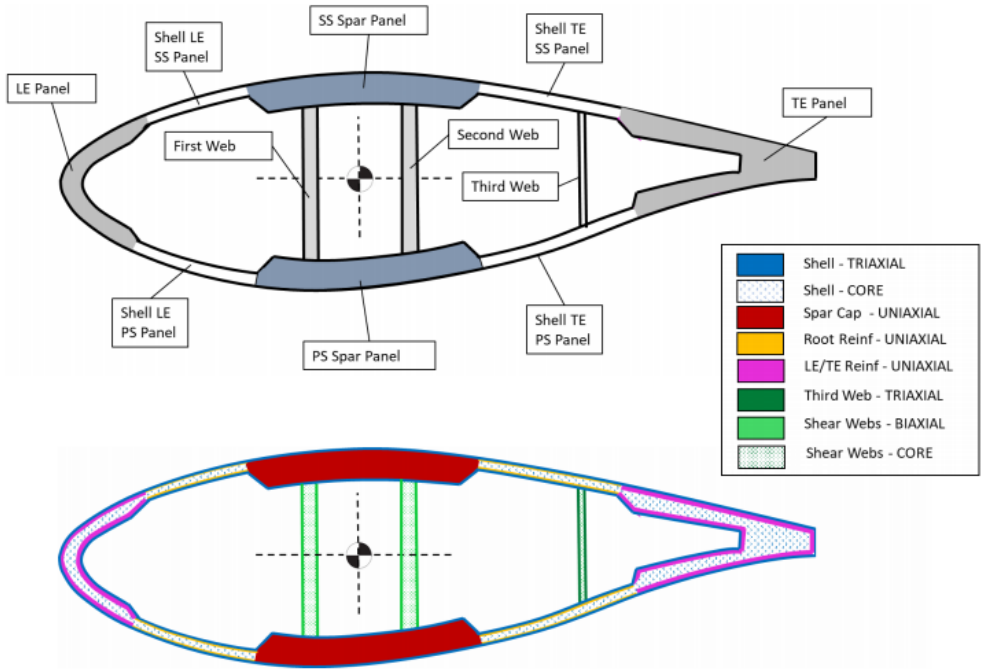

Figure 3.4: Structural elements and components of a typical section

It is important to understand the main workflow of the structural design optimization: *Cp-Lambda* model is updated with structural properties coming from the blade composition and the thickness distribution of the materials. The desired set of DLCs are then performed to obtain loads histories, which fix the limits to be respected by the optimization of the selected thickness variables. These constraints are computed with a complete structural analysis, which includes fatigue, a FEM for stress and strains evaluation, modal analysis and the evaluation of max blade displacement. At the end, the structural thicknesses and the corresponding boundaries are saved, so that the code is ready for the next global iteration.

As it is now clear *Cp-Max* is a complex and powerful design optimization code characterized by a great flexibility, which causes the user to invest time and experience to learn how the code works, but at the same time makes it is very adaptable, adjustable and, ultimately, improvable.

Chapter 4

Cp-Max implementations

In the following chapter it is explained how it is possible to introduce the noise analysis tool inside the aerodynamic cycle to guarantee its influence on the designed configuration. As can be seen in Fig. 4.1, the analysis can be divided in three main blocks: preprocessing, *XFoil* simulations and semi-empirical models. The latter have already been presented and left untouched, whereas the others are described and then modified to suit the work purpose. Furthermore, for the preprocessing phase, which mainly consists of *Cp-Lambda* dynamic simulations, specific routines are computed to overcome the absence of data due to the new position of the tool inside the code. Regarding *XFoil*, a sensitivity analysis is performed to find the best compromise between computational time and accuracy of the results. Moreover, noise emissions are calculated for different wind speeds, so the analysis of one configuration is in reality the sum of multiple analyses computed for selected velocities. This is important because the computational time is influenced by the number of wind speeds chosen by the user.

4.1 Prepocessing

The acoustic tool, to be able to compute *XFoil* simulations and, ultimately, noise emissions, requires data of specific sensors from *Cp-Lambda* dynamic simulations. Particularly, the noise analysis has the purpose to calculate the amplitude for a normal working condition, inspecting the annoying constant sound produced. For this reason, data are retrieved from DLC 1.1, Dynamic Load Cases defined by IEC 61400-1[63],

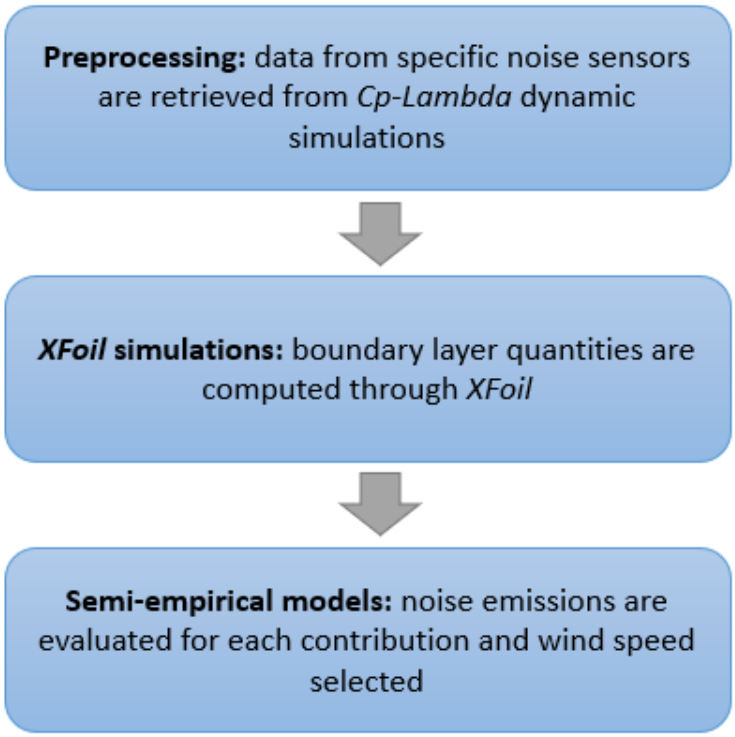

Figure 4.1: The three main blocks in which is divided the noise analysis

which are computed for 12 wind velocities, from 4 m/s to 25 m/s. They correspond at simulations for an energy production with a normal turbulent model. Another important aspect is that studies have shown that the second half of the blades is responsible for most of the noise produced by the whole rotor, therefore sensors are distributed only from the mid-span to the tip, and also the analysis is performed only on this section. Sensors are able to compute, for each section where they are positioned, the time history of:

- positions
- velocity of the flow and relative velocity
- aerodynamic properties, specifically angle of attack α, C_L, C_D and C_M
- displacements
- rotor azimuth angle

Initially, as it can be seen from Fig. 3.1, the noise tool is positioned after the structural block, since it has the purpose to analyze the configuration without acting on it.

Therefore, data are retrieved from DLC 1.1, computed for structural reasons, which inspect wind turbine response for 10 minutes. As demonstrated by *Sucameli* [4], aeroacustic analysis require only 15, 20 seconds to be able to compute reliable results. This is important, since to be able to introduce the tool inside the aerodynamic block, DLCs computation must be anticipated, but there is no reason to perform long simulations.

First it is needed to create a new routine which can compute DLC 1.1 for a much shorter time. Due to their new position before the aerodynamic cycle, dynamic simulations require three unavailable inputs at the moment: normal turbulent wind time history, control laws and static simulations. They can all be calculated by duplicating the routines used in the control and structural blocks. Dynamic routines, instead, cannot be simply copied, since sensors different from noise ones are useless and, more importantly, a new definition is given to the length of the simulations. The latter, indeed, is composed of the real noise analysis time, which is defined starting from the minimum rotational velocity, plus a transition time fixed at 15 s, to ensure convergence, letting the simulations adapt to dynamic conditions, and to make possible to calculate retarded configurations. The latter are needed to be able to sum the different noise sources, since trailing edge contributions are produced at the end of the profile while turbulent inflow one at the mid-chord.

The idea is to study at least a third of revolution of the rotor, since the machine has three blades and so it follows a nearly cyclical behavior every 120°. Moreover, as it is shown in Figs. 4.2 and 4.3, low wind simulations, which corresponds to low rotational speed simulations, generate much lower noise emissions than high ones, so are of less importance. Also, the simulation time is fixed for every dynamic simulation, so results from higher rotational speeds than the minimum one are even more reliable, since they include more than just a third of revolution of the rotor. This is the same approach used and demonstrated by *Sucameli* [4] in developing the noise tool.

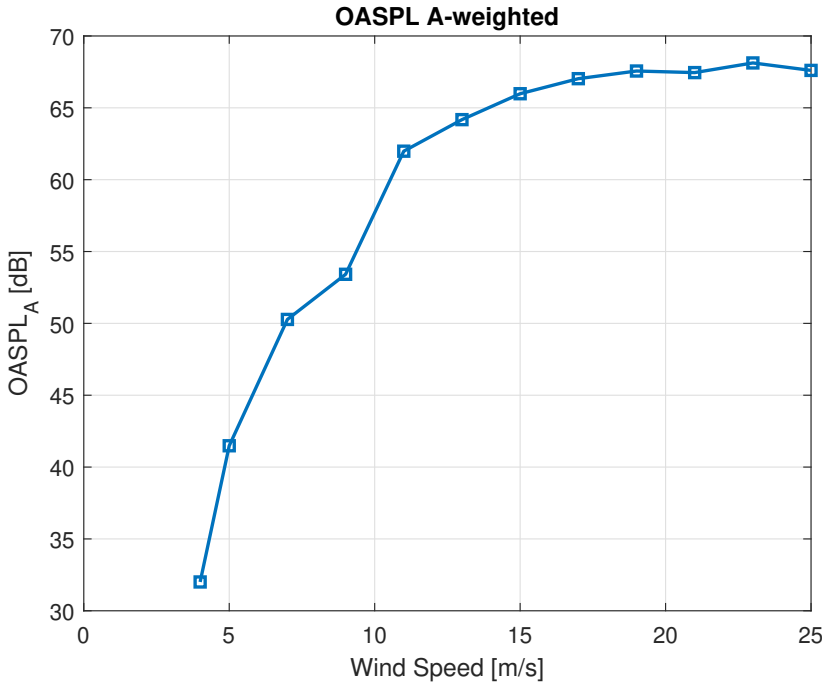

Figure 4.2: OASPL$_A$ computed for different wind speed values

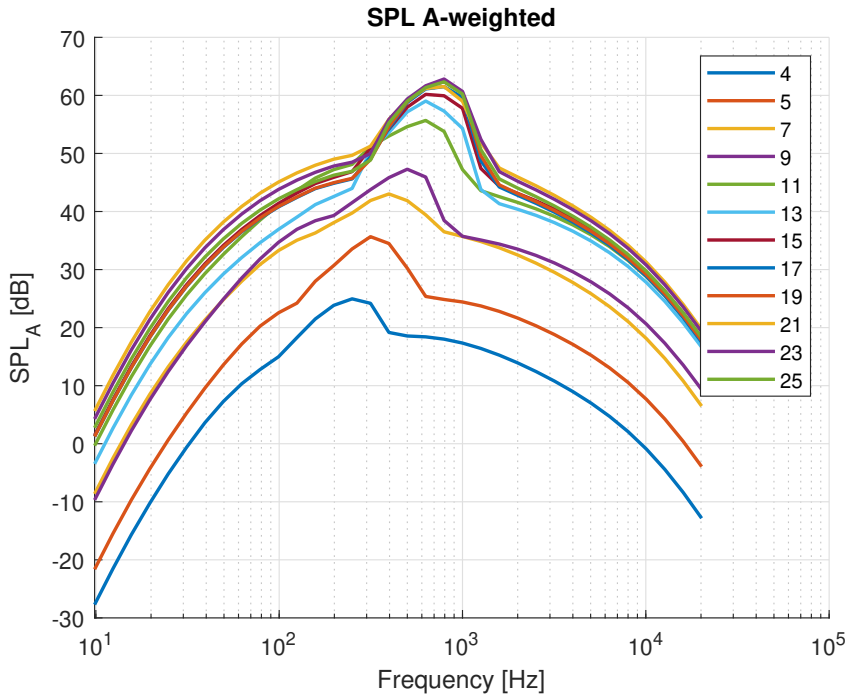

Figure 4.3: SPL$_A$ computed for different wind speed values [m/s]

The last aspect to underline is that, as already said, the noise analysis can be performed for each reference wind speed of DLC 1.1. The user can select all the wind speeds or can choose only a subset of them. This is very important because, as it can be seen from Figs. 4.2 and 4.3, once the control limits the rotational velocity the amplitude of the emissions are very similar, showing a strong dependence on it

and not on the ideal free-stream velocity. So it is possible to save time by performing the analysis not for each speed, but, only, for specific ones. Following the same logic also the dynamic simulations are computed at wind speeds for which is required to evaluate noise emissions.

4.2 *XFoil* simulations

The noise analysis is based on the *strip theory*: blades are divided in several sections of constant chord and the noise produced by each one is calculated. The total spectra of the rotor is then recovered by summing the sound emitted by every portion. This method is a good and faster alternative at a CFD analysis of the whole rotor and it is very suitable to be coupled with *Cp-Lambda* simulations, whose results are directly computed on airfoils along the blades. Moreover, the set of profiles chosen for the analysis, consequently the number and the span of each sector, can be different from the one chosen for *Cp-Lambda* calculation, thanks to the previous interpolation along the blade of data acquired from sensors. This is very important because the number of sensors have few relevance on the computational time of the dynamic simulations, while the number of airfoils is one of the four parameters that strongly impact the computational cost of *XFoil* simulations.

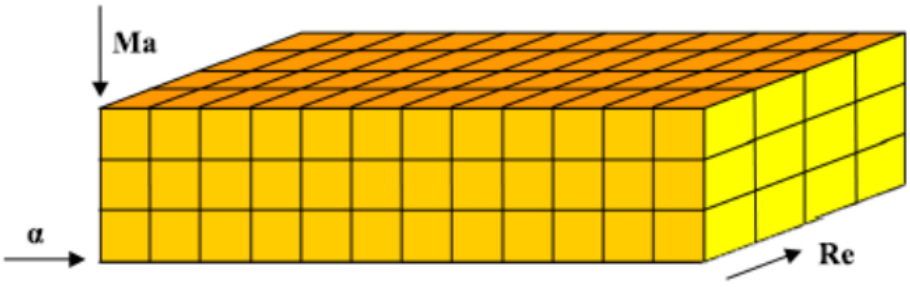

Figure 4.4: Logical representation of the 3D lookup table built for each section

Theoretically, *XFoil* simulations should be performed for every angle of attack, Mach and Reynolds experimented by the machine during the dynamic testing to precisely compute boundary layer data. Of course, this is unfeasible and the solution is

to generate a three dimensional lookup table based on their values. The idea is to simulate only some conditions and then to interpolate the results, so that it is possible to reconstruct the outputs for different inputs. For each airfoil station selected by the user, a lookup table is generated. Initially, 500 conditions are tested by considering 20 angles of attack, 5 Mach numbers and 5 Reynolds ones. It is important to understand that these are the number of values considered for each quantity in order to create the lookup table and not directly the values of the quantities, which are computed automatically by the code. The set of airfoils selected is composed by 10 profiles equally distributed from the mid-span to the tip, η = [0.5 : 0.05 : 0.95]. At the end the total number of simulations is 5000. The latter require a lot of time to be computed, nearly three hours, which is way too much to be inserted in a cyclical process.

A sensitivity analysis is conduced in order to find a good compromise between the quality of the results and the computational time. The previous set is considered as the reference configuration and the parameters are varied individually, so that it is possible to understand their influence on the results. Particular attention is given to to the set of profiles considered, since it can be changed the length of each sector, or it can be chosen a different portion of the blade, by considering different starting and ending sections. The analysis is performed by comparing, for every wind speed, the sound pressure level spectra of each contribution and the total one. Also, in order to be able to consider only one value for a variable, a modification to the code is done, so that it is possible to use only the average value between the minimum and the maximum. Before, indeed, the algorithm forced an interpolation that required to use at least two values. The results are here reported for a wind speed of 11 m/s.

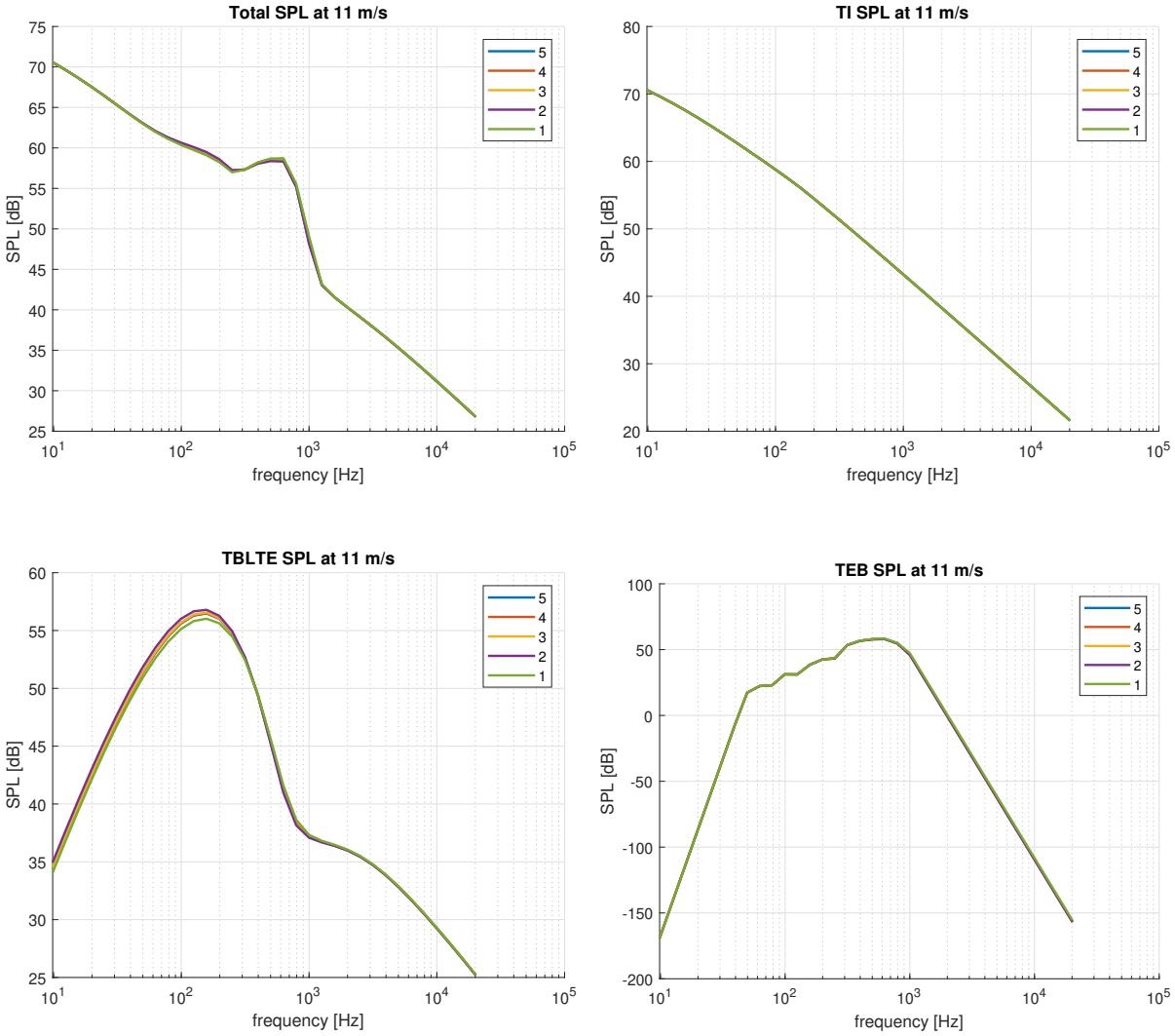

Figure 4.5: SPL spectra varying the number of Mach values used by the lookup table

As it can be seen, Mach value has really little impact on the final results. This was expected, since wind turbines, so also the machine considered, work with low wind and rotational speed, which causes the Mach number to be less than 0.3, where compressibility effects are negligible.

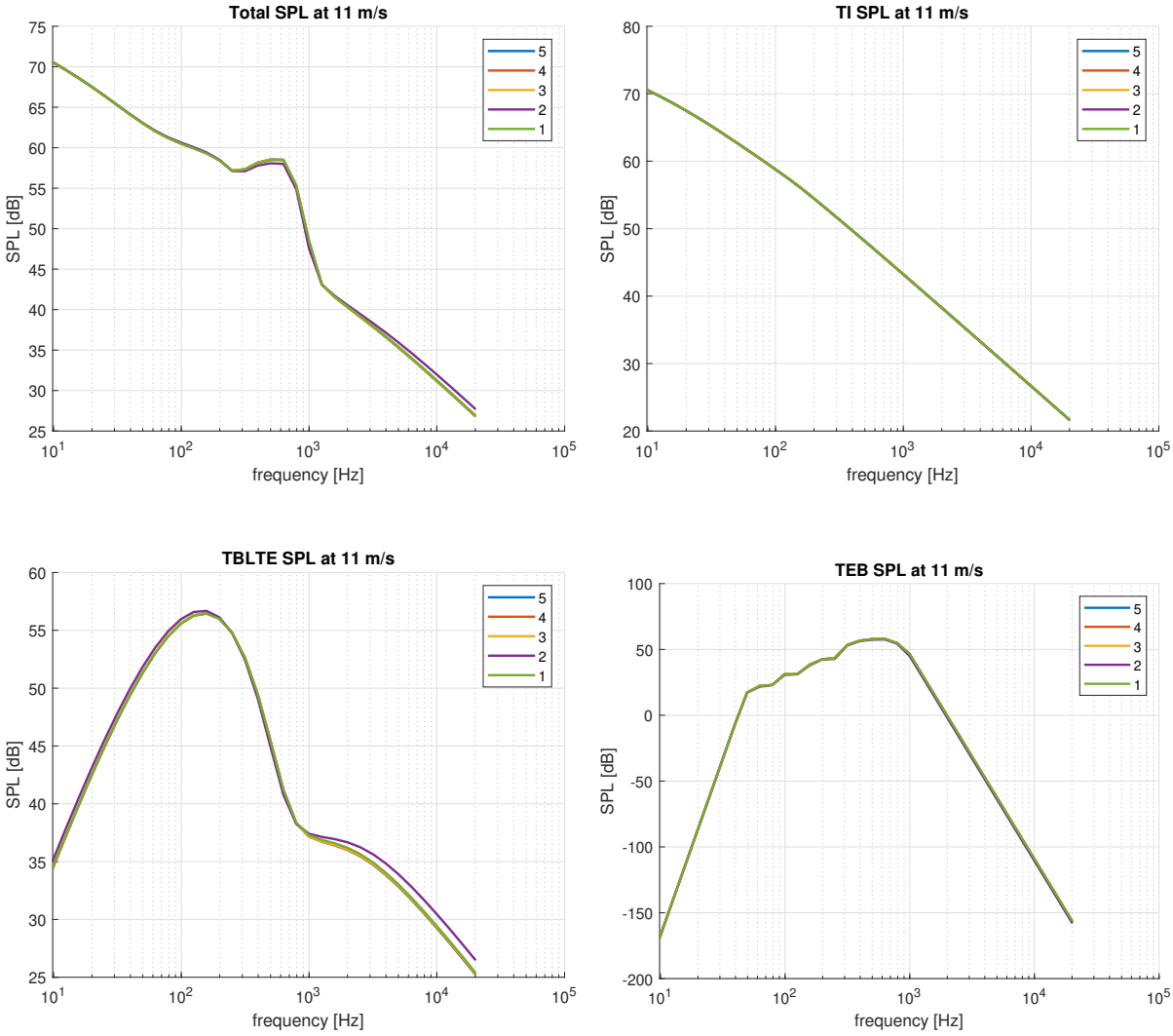

Figure 4.6: SPL spectra varying the number of Reynolds values used by the lookup table

It is clear that also Reynolds number has little influence on the results. This is explained by the working range of turbines, which is in order of 10^6, where the boundary layer is already fully turbulent for every tested conditions.

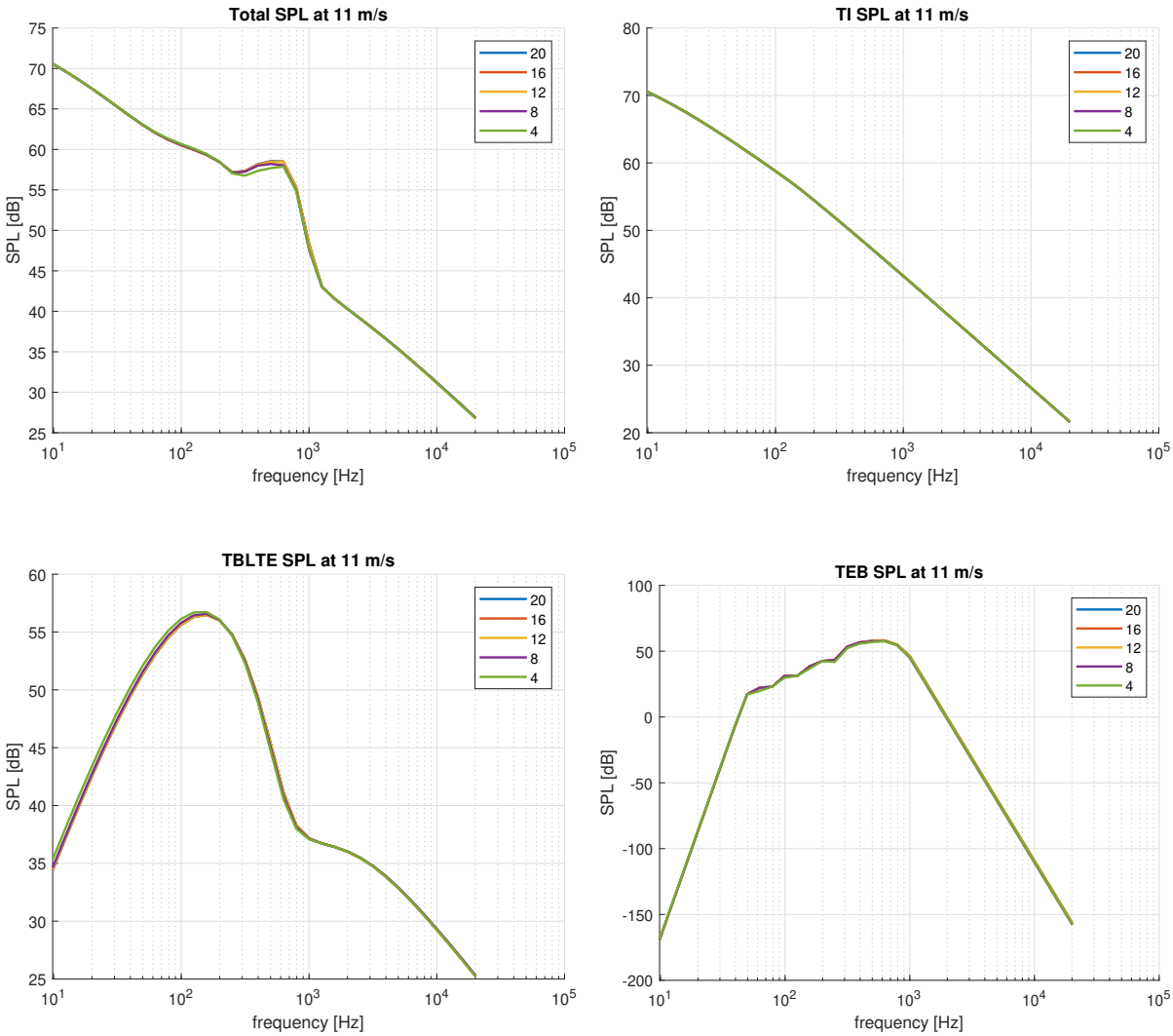

Figure 4.7: SPL spectra varying the number of angles of attack used by the lookup table

The number of angles of attack cannot be lowered too much, because the code may not work due to the inability to reach convergence. Indeed, *XFoil* simulations may crash, when this happens the code automatically interpolates results from other angles of attack and reconstructs the solution. For this reason, using less than 4 angles must be avoided, in order to guarantee that the code works during the aerodynamic cycle. As shown by Fig. 4.7, also in this case using much lower values has little influence on the final results, which proves the goodness of approximating the solution by interpolating only few results.

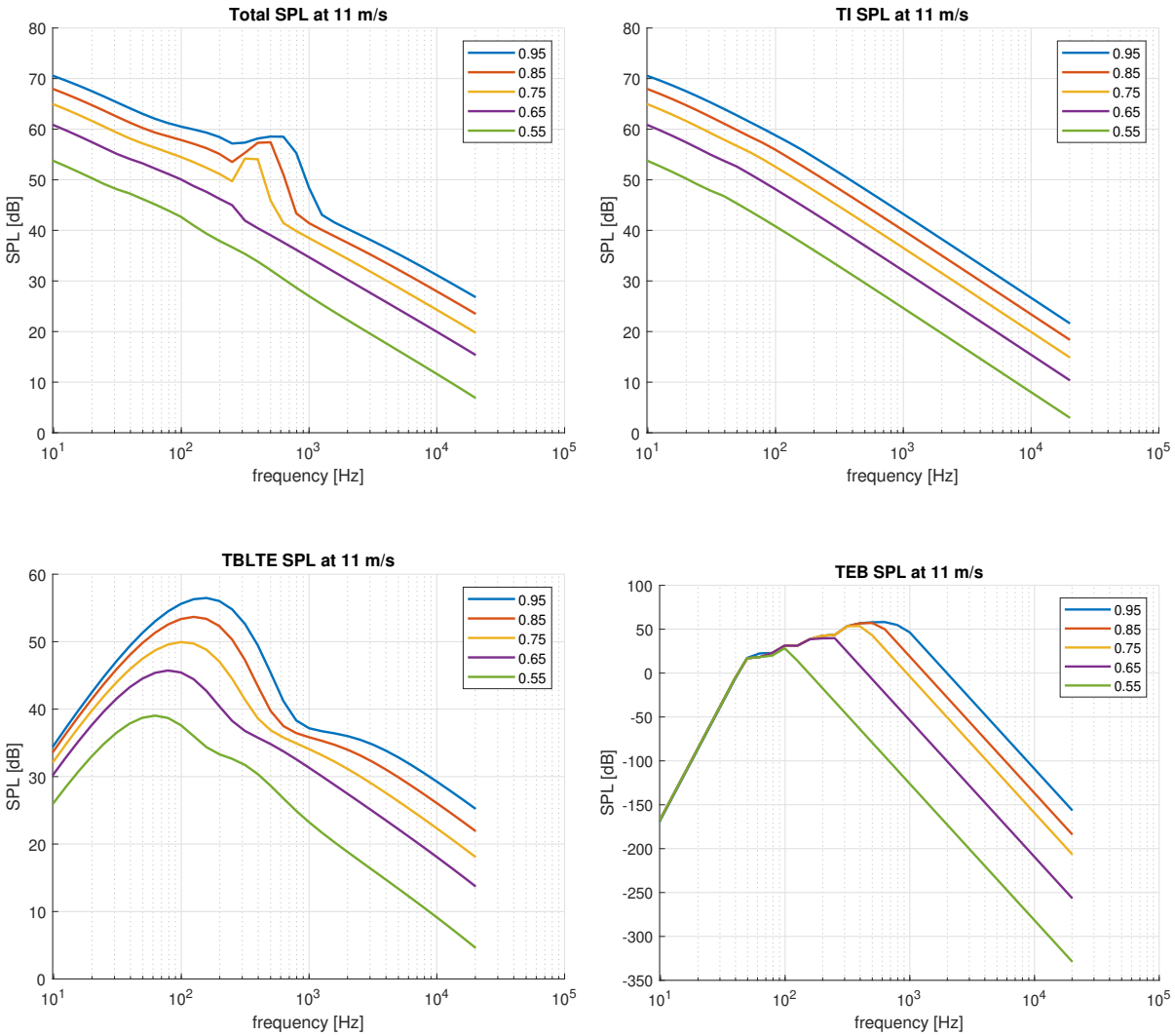

Figure 4.8: SPL spectra moving the inner section and fixing $\Delta\eta$ = 0.05, η_{out} = 0.95

As said, airfoil stations array can be modified in different ways. From Fig. 4.8, it is clear that the final part of the blade is the main noise source and must be included in the analysis. This confirms what was expected and already demonstrated in literature [4, 23]. The other possibilities are far more important to better understand how it is possible to reduce the number of airfoils without losing accuracy of the results. Fig. 4.9 shows how too long sectors, so too much distance between two airfoils, compromise the goodness of the *strip theory*. Indeed, the blade must be divided in multiple small parts to have trustworthy results comparable with the ones produced by CFD simulations.

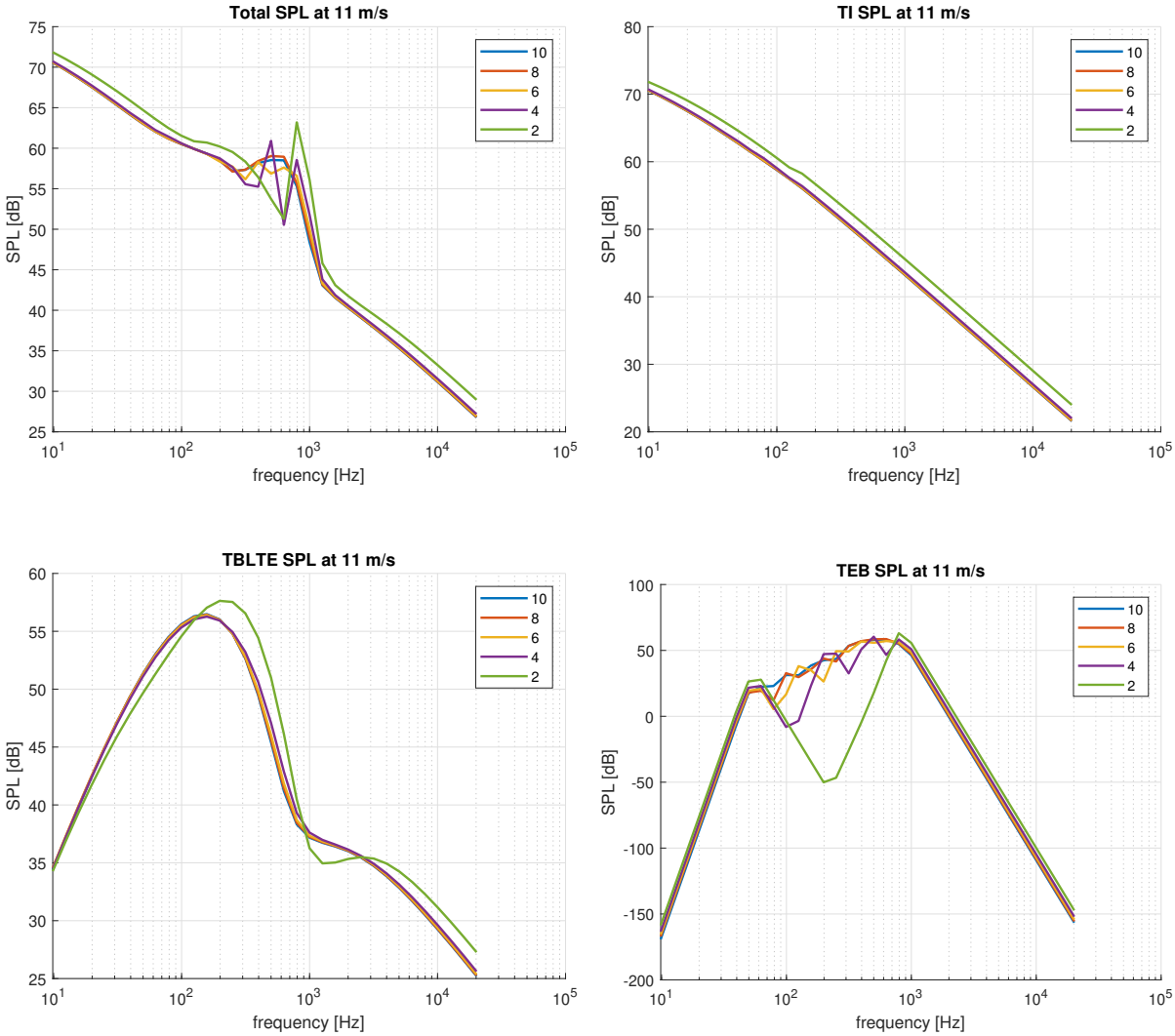

Figure 4.9: SPL spectra varying the number of portions in which the blade is divided between the fixed inner section, η_{inn} = 0.5, and outer section, η_{out} = 0.95

Finally, the starting point of the blade portion considered is moved towards the tip. The results are interesting because the total spectra of the whole second half of the blades is very similar to the one deriving from considering only the last 30 % of the blades. Still, in Fig. 4.10 differences can be seen by analyzing only the turbulent boundary layer - trailing edge contribution and the trailing edge bluntness one.

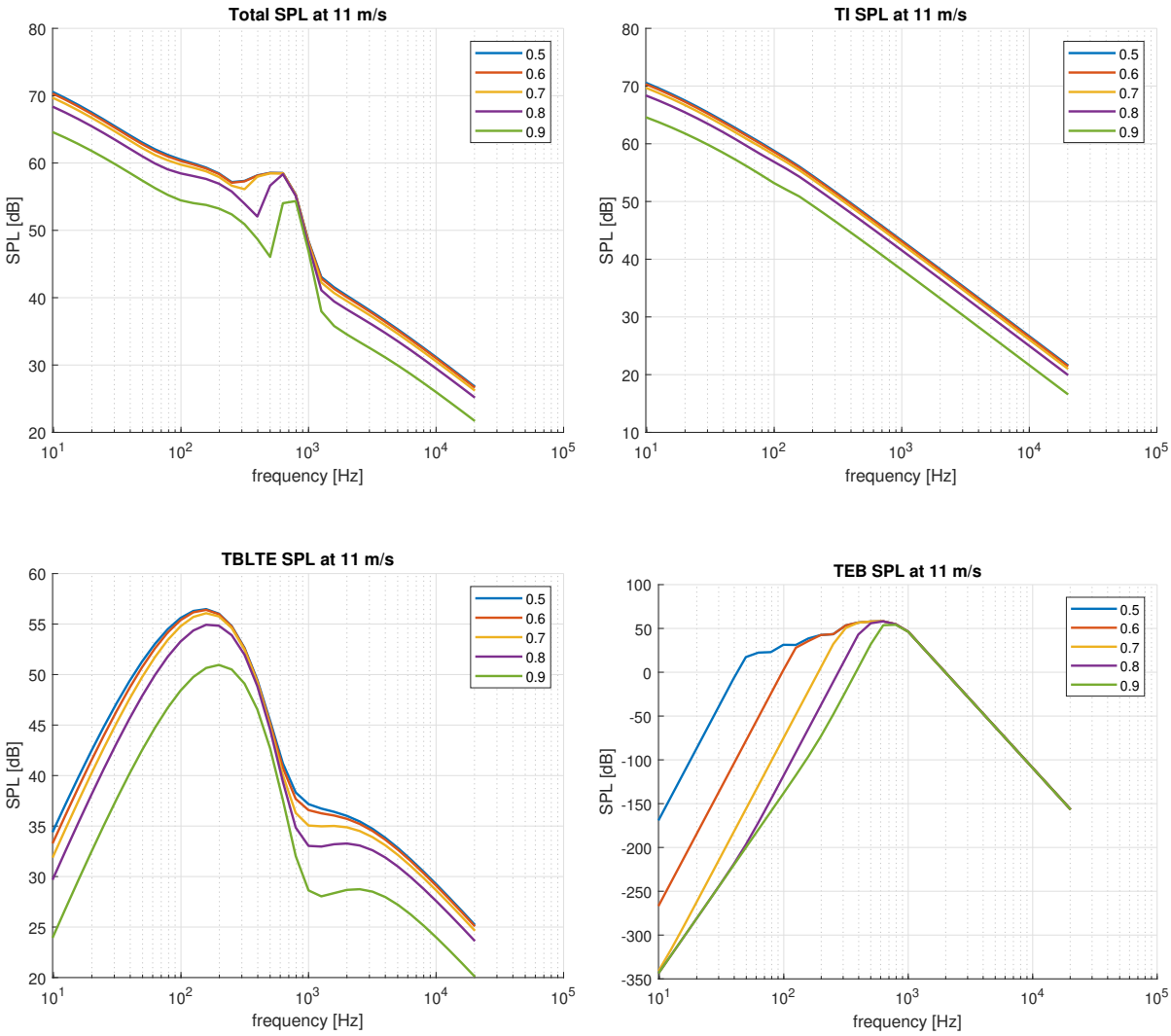

Figure 4.10: SPL spectra moving the outer section and fixing $\Delta\eta$ = 0.05, η_{inn} = 0.5

After having tested different configurations, it is decided to consider:

- 1 Mach and Reynolds number, which corresponds to the middle value between the minimum and the maximum
- 6 angles of attack, more than 4 to ensure that simulations converge for at least three different values avoiding the crash of the code and producing accurate results
- 8 airfoil stations not equally distributed, η = [0.5, 0.6, 0.7 : 0.05 : 0.95], in order to catch accurately the results from the tip of the blade but, also, to include the portion before without adding too many profiles

The comparison with the baseline can be seen in Fig. 4.11. As it is clear the values are very similar, but the computational time is strongly reduced, indeed from 5000 the

simulations are lowered to only 48, which, also, decreases the time from nearly three hours to just five or six minutes.

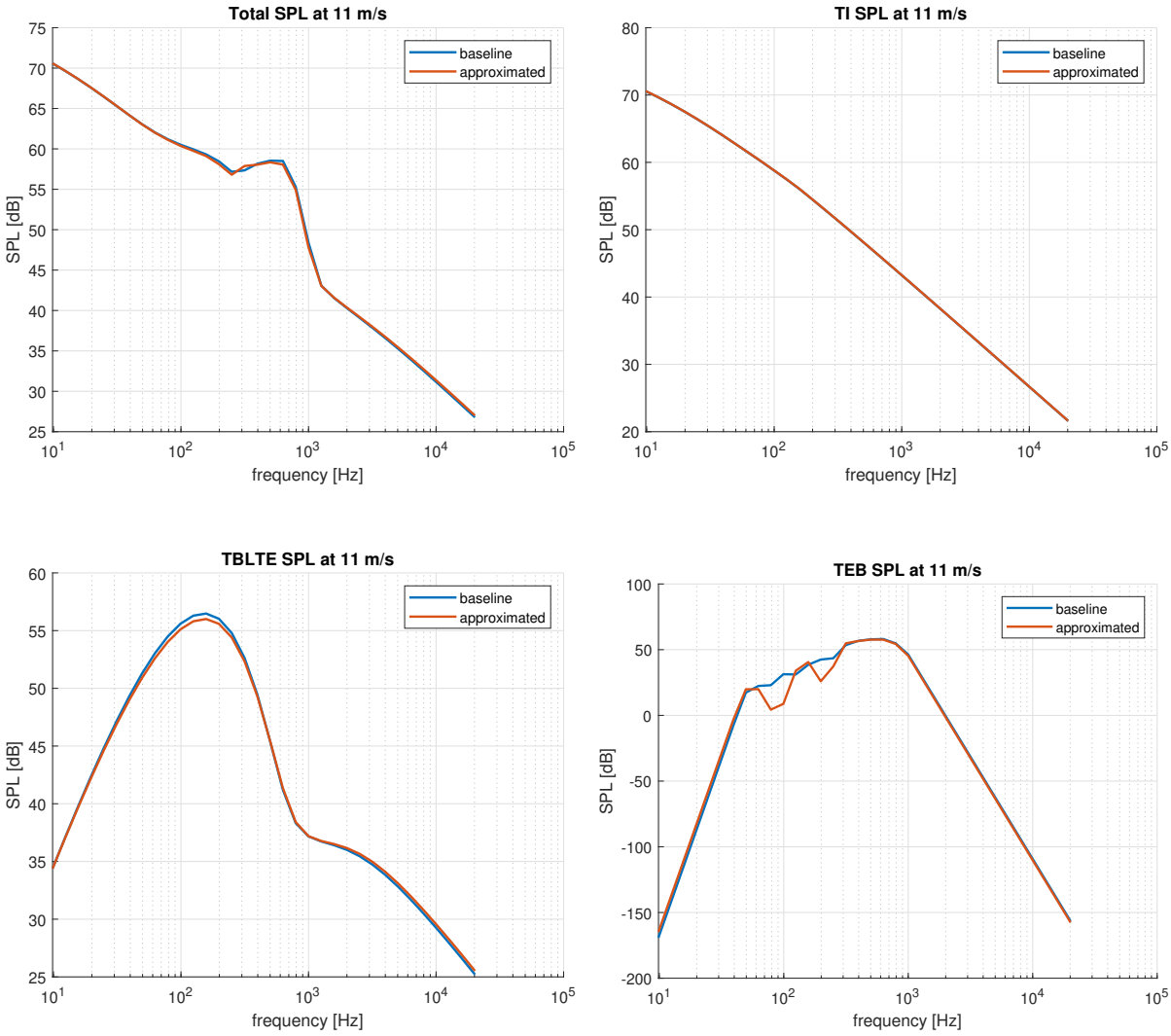

Figure 4.11: SPL spectra comparison between baseline and final configuration

4.3 Aerodynamic cycle

Finally, the noise analysis can be introduced inside the aerodynamic cycle. As said, the first idea is to create a new constraint for the optimization, so that the blade geometry can be influenced by noise emissions. First, the modification of the coordinates of the airfoils must be felt also by the noise tool, so it is important to update the values not only in cost evaluation function but also inside constraints computation one. It is now possible to describe new limits, which, to simplify the formulation, are imposed for each wind speed selected by the user on the total overall sound pressure level

A-weighted, since it is important to reduce noise perceived by human hearing. In this way it is possible to identify a single value for each noise analysis performed, and compare it with the limit, which is fixed by the user. The constraint formulation is:

$$C_{noise,i} = \frac{OASPL_{A,i}}{\overline{OASPL}_{A,i}} - 1 \leq 0 \tag{4.1}$$

where i corresponds at each wind speed selected for the analysis and $\overline{OASPL}_A$ is the maximum limit imposed for each velocity.

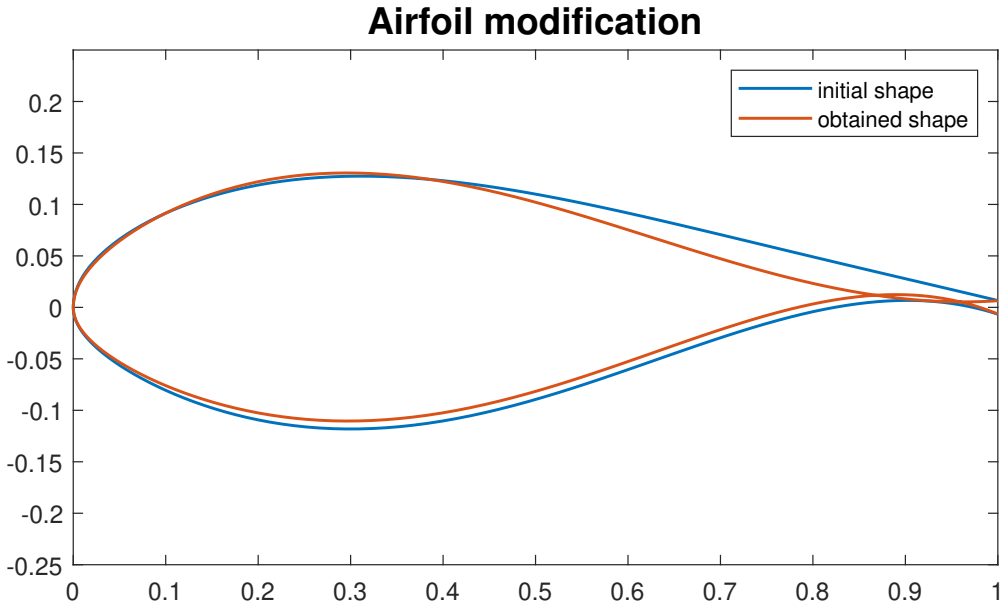

Figure 4.12: Airfoil shape modification without a constraint on the minimum thickness

Furthermore, it is introduced, also, a new constraint on the minimum thickness of the airfoils, from the middle point to the trailing edge, since every airfoil has a null thickness at leading edge. This is done to avoid the overlapping of suction and pressure side and to leave enough space inside the section for structural components. Indeed, permeation may happen during the optimization cycle, due to the strong influence of noise constraint on the *free-form* definition of the blade. As it can be seen in Fig. 4.12, the code may crash in trying to quickly reduce noise emissions, while using a new constraint increases the robustness of the algorithm avoiding unphysical solutions, particularly permeation. The latter has not been a problem in the normal *free-form* method due to the lower aerodynamic performances produced by lowering so much

the zone next to the trailing edge. When noise limits are imposed, on the contrary, the code tries to reduce it in order to satisfy noise limits, which initially are the most important constraint. For these reasons, by imposing a new boundary on the minimum thickness, it is possible to limit the decreasing trend imposed by the algorithm.

$$C_{min\,thick} = 1 - \frac{Thick_{min}}{\overline{Thick}_{min}} < 0 \tag{4.2}$$

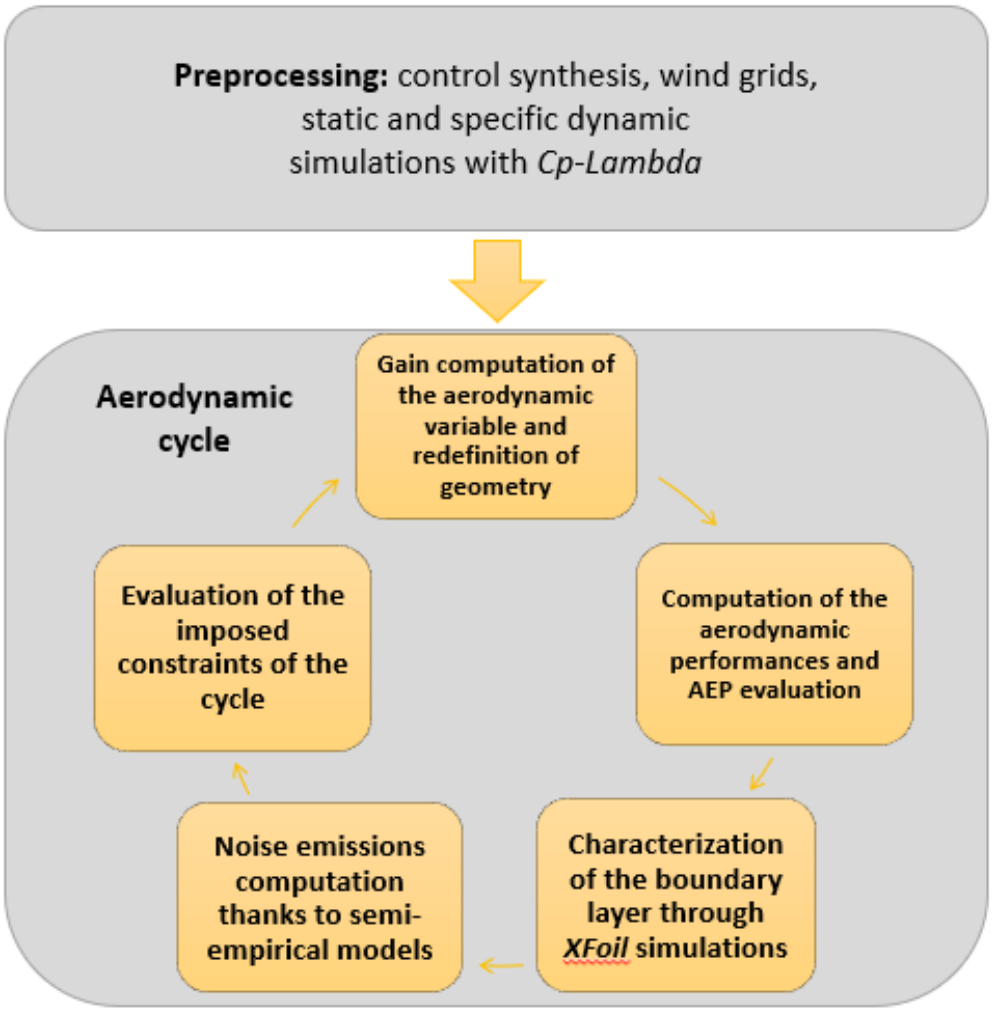

Figure 4.13: Scheme of noise constraint implementation in the aerodynamic cycle

Specific simulations have been created to compute the noise analysis, but now the latter must be introduced inside the aerodynamic optimization. Even with all the modifications done to reduce the computational time, *Cp-Lambda* simulations still require more than half an hour, so it is unfeasible to introduce them inside the aerodynamic cycle. Indeed, the aerodynamic gradient based optimization is divided in iterations

and sub-iterations. In order to find the correct direction of optimization, between two iteration results the algorithm varies one by one the value of each variables of the aerodynamic cycle and for each time it computes the AEP and it evaluates the constraints. Therefore, a noise analysis is performed at each sub-iteration, which can be even more of 100. So it is clearly impossible to introduce *Cp-Lambda* simulations inside the cycle and an alternative way must be found. The idea is to compute the dynamic simulations at the beginning of the aerodynamic submodule, before entering the cycle, and then to consider the results frozen inside it. This possibility is justified by the expected relative small change to rotational speed in the trajectory regulation between the initial configuration and the final one. Indeed, much more influencing parameters, like the solidity, are global variables, so they are fixed for each global iteration and cannot be changed in the aerodynamic cycle. Moreover, data retrieved from the simulations are used to calculate the angle of attack, the Mach number and the Reynolds number, used as input for *XFoil* computations, have little effect on the characterization of the boundary layer. This is due to how the analysis is built, as it has been explained in the previous section. Nevertheless, some errors are still expected and the accuracy of the implementation must be evaluated.

It is now given a formal description of the final optimization cycle, highlighting the modifications introduced.

$$(p_a^*, AEP^*) = \textit{MaxAEP}(p_a, p_s, p_g, D)$$

$$AEP^* = Max_{p\,a}\left(\textit{ComputeAEP}(p_a, p_s, p_g, D)\right)$$

$$p_a^* = arg\left(Max_{p\,a}\textit{ComputeAEP}\right)$$

such that:

$$p_a, = [p_{a\,c}, p_{a\,\theta}, p_{a\,CST}]$$

$$p_g, = [R, H_{hub}, \theta_\pi, \gamma_b, \sigma_c^g, \tau_c^g, t_{air}]$$

$$g_a(p_a, p_g) \leq 0$$

$$\mathbf{C_{min\,thick}}(\mathbf{p_a}, \mathbf{p_g}) \leq \mathbf{0}$$

$$\mathbf{C_{noise}(p_a, p_g) \leq 0}$$

where p_a is the array of the aerodynamic variables, divided on whether they control the chord $p_{a\,c}$, the twist $p_{a\,\theta}$ or the CST coefficients $p_{a\,CST}$. The array p_g, instead, represents the global variables, as the solidity and maximum thicknesses of each airfoils. g_a is the set of constraints already implemented. Their formulation starts from both the variables necessary to fulfill the macro design loop requirements and from some practical limitations, like the max chord. In bold are visible the new constraints on noise emissions and on the minimum thicknesses of the profiles from the mid point towards the trailing edge. Finally, the new architecture of *Cp-Max* can be seen in Fig. 4.14.

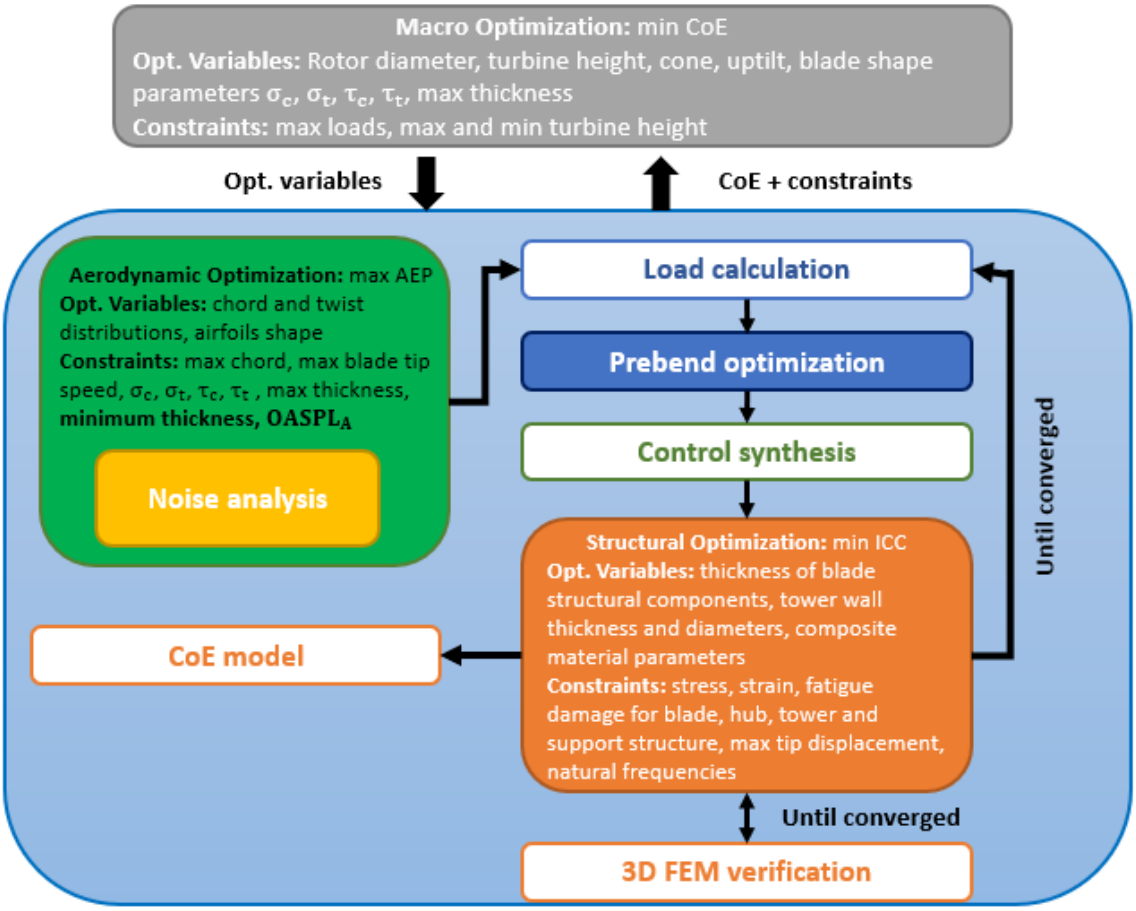

Figure 4.14: New architecture of *Cp-Max*

Chapter 5

Results

In this chapter, after a brief description of the wind turbine considered, are presented the results of the simulations performed. The first two cases are only aerodynamic optimizations, while the last case is a global optimization, so it also includes the structural module. The results are then discussed and compared to reference simulations, in order to discover how the constraint is affecting the geometry of the turbine and its performances. Furthermore, in order to be more clear, the noise contributions are shorten with their acronyms: TI, turbulent inflow; TBLTE, turbulent boundary layer - trailing edge; TEB, trailing edge bluntness.

5.1 Description of the considered DTU-10MW turbine

The machine considered in the present work is a large-size three-bladed wind turbine, which was developed under the Light Weight Rotor project at the Technical University of Denmark and was designed by upscaling a known reference machine, the NREL 5 MW wind turbine. The main characteristics can be seen in Tab. 5.1.

IEC Class	1A
Rotor orientation	Clockwise, upwind
Control type	Variable speed, collective pitch
Drivetrain	Single stage
Cut-In speed	4 m/s
Cut-Out speed	25 m/s
Rated wind speed	11.6 m/s
Rated aero power	10.64 MW
Max tip speed	83,93 m/s
Cone angle	3.5 °
Tilt angle	6 °
Rotor overhang	7.07 m
Rotor radius	89.15 m
Number of airfoil stations	7
Blade prebend	–
Hub height	119 m
Tower height	115.63 m
Hub mass	446 tons
Nacelle mass	105.5 tons
Blade mass	40.7 tons
Tower mass	628.4 tons
Blade cost	281 k$
Tower cost	2071 k$
Generator efficiency	94 %
Cost Of Energy	77.92 $/MWh

Table 5.1: General characteristics of the DTU-10MW turbine

It is, also, important to define the geometry of the initial blade, which is described by a set of 7 airfoils. The latter are shown in Tab. 5.2 and in Fig. 5.1, while the other figures represent distributions of chord, thickness and twist. It is important to remark

that only the chord, which is controlled by four poles at η = [0, 0.261, 0.65, 1], will be changed, particularly only in the global simulation. Then are defined the values of: the static AEP; the maximum C_p and the corresponding TSR for which is found; the rated velocity V_r.

Number	Airfoil	Thickness %	Positioning along the blade %
1	Circle	100	0
2	Circle	100	1.74
3	FFA-W3-480	48	20.80
4	FFA-W3-360	36	29.24
5	FFA-W3-301	30.1	38.76
6	FFA-W3-241	24.1	71.87
7	FFA-W3-241	24.1	100

Table 5.2: Description of blade airfoils

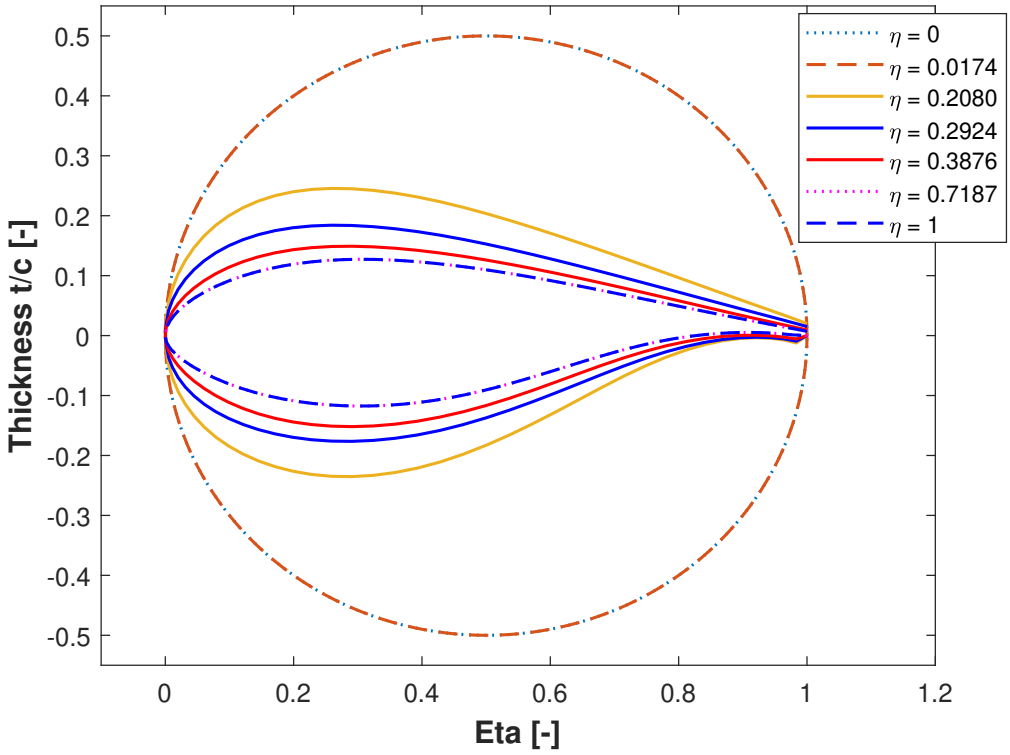

Figure 5.1: Baseline airfoils shape

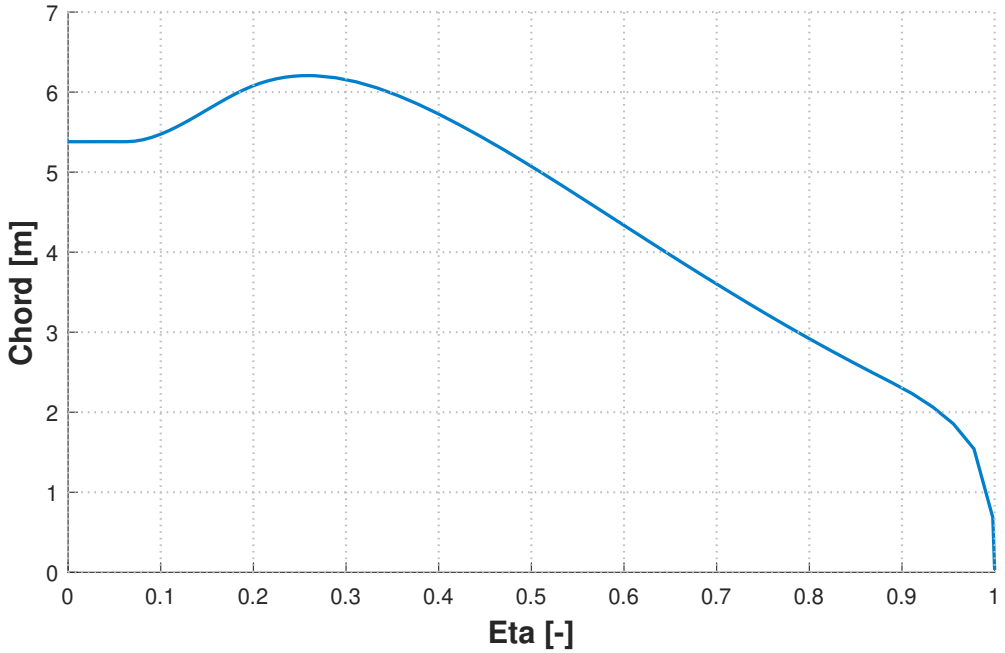

Figure 5.2: Baseline chord distribution along the blade

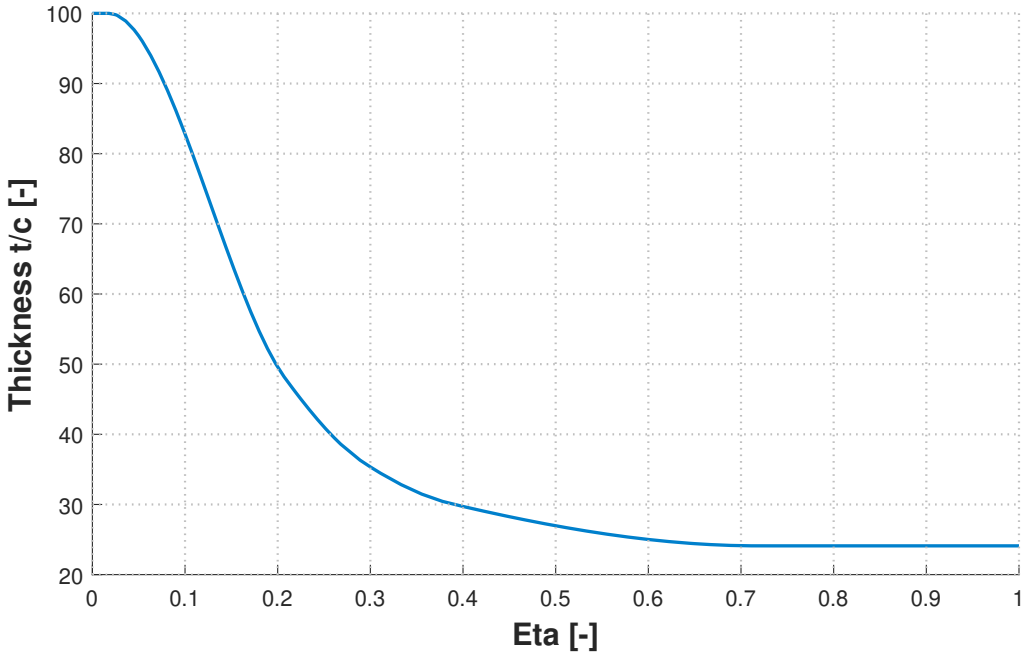

Figure 5.3: Maximum airfoil thickness distribution along the blade

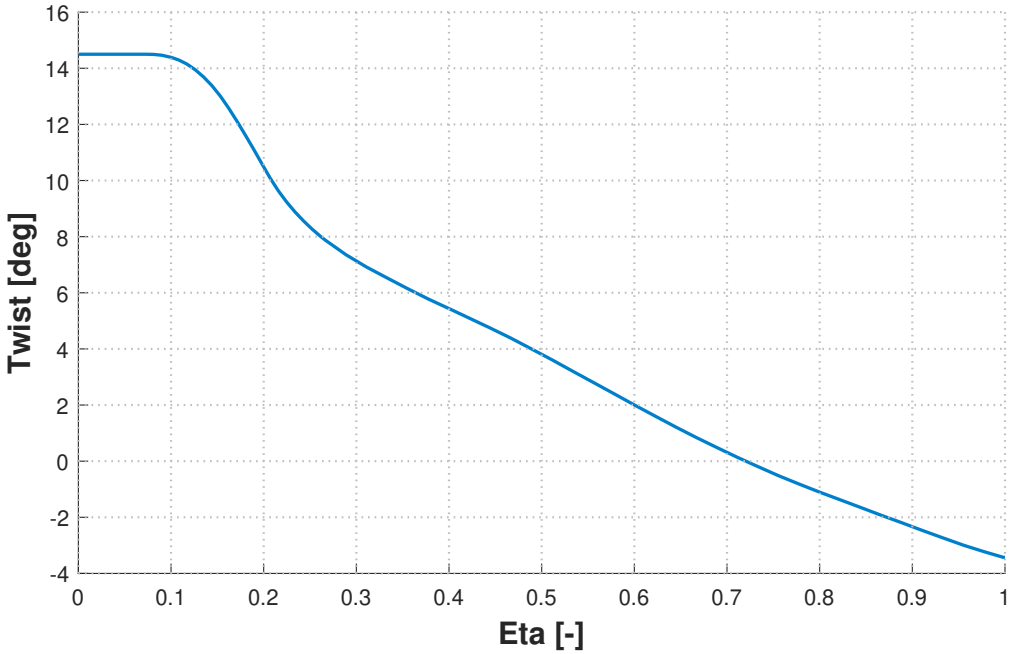

Figure 5.4: Twist distribution along the blade

AEP	Cp*	TSR*	V_r
51390 MWh	0.4542	7.295	11.6 m/s

Table 5.3: Aerodynamic parameters in the baseline

Finally, the structural description of the machine is reported. In Figs. 5.5 and 5.6 and in Tab. 5.4 are presented the thicknesses of structural elements and the area occupied inside the blade. To avoid repetitions, other properties are shown in comparisons made with the obtained reference configuration, section 5.3.1.

Section η	$t_{shell}^{TE,ss}$	$t_{shell}^{LE,ss}$	$t_{shell}^{TE,ps}$	$t_{shell}^{LE,ps}$	t_{rein}^{root}	t_{spar}^{ss}
0	50.00	50.00	50.00	50.00	15.00	-
0.010	50.00	50.00	50.00	50.00	15.00	-
0.050	12.00	12.00	12.00	12.00	8.50	1.00
0.100	5.00	5.00	5.00	5.00	8.33	10.29
0.220	3.01	3.01	3.01	3.01	2.79	99.93
0.356	3.23	3.23	3.23	3.23	2.79	118.02
0.450	3.99	3.99	3.99	3.99	-	116.83
0.650	2.40	2.40	2.40	2.40	-	69.33
0.800	1.01	1.01	1.01	1.01	-	30.94
0.950	1.61	1.61	1.61	1.61	-	5.97
0.978	1.45	1.45	1.45	1.45	-	5.14
Section η	t_{spar}^{ss}	t_{web}^{front}	t_{web}^{rear}	t_{web}^{third}	t_{rein}^{LE}	t_{rein}^{TE}
0	-	-	-	-	-	-
0.010	-	-	-	-	-	-
0.050	1.00	1.00	1.00	-	-	-
0.100	10.29	1.00	1.00	-	0.10	1.00
0.220	99.93	5.00	5.00	4.50	3.50	9.00
0.356	118.02	6.02	6.02	6.00	3.20	11.00
0.450	116.83	7.00	7.00	7.00	3.00	6.00
0.650	69.33	8.15	8.15	4.00	4.38	3.00
0.800	30.94	7.00	7.00	3.75	0.78	1.32
0.950	5.97	5.00	5.00	3.00	0.10	0.10
0.978	5.14	3.50	3.50	-	-	-

Table 5.4: Thicknesses [mm] of the structural components in the baseline

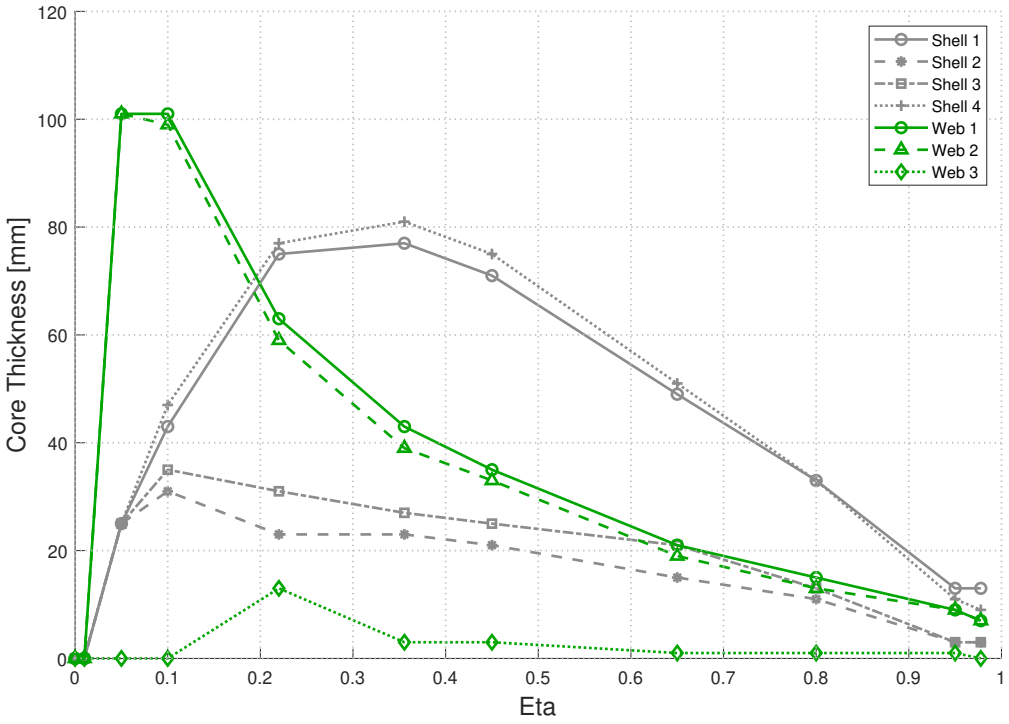

Figure 5.5: Core thickness distribution of baseline components

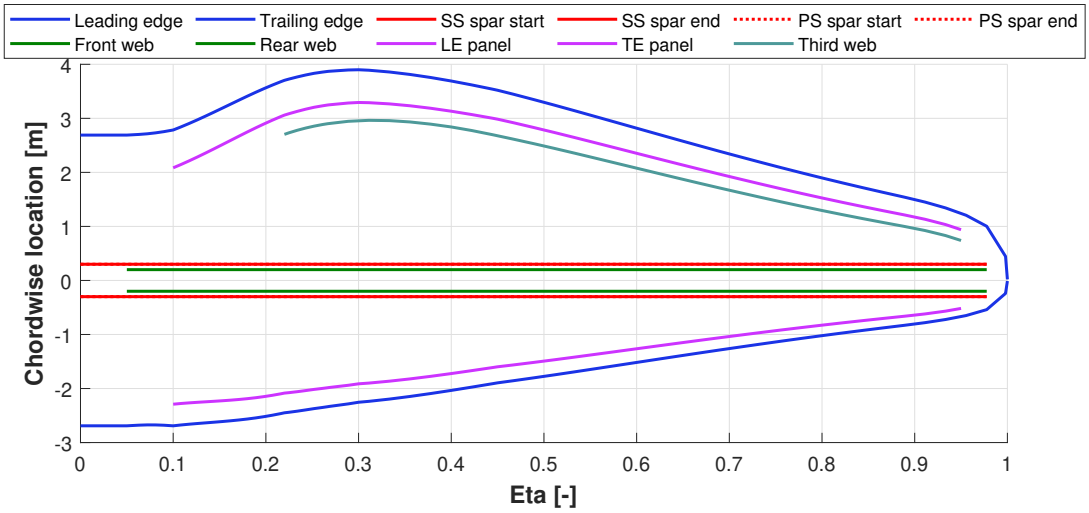

Figure 5.6: Baseline blade planform

5.2 Aerodynamic simulations

The first simulations consist in aerodynamic optimizations, whose active variables are, only, the weights of the 3^{rd} order CST parametrization that describes the final two airfoils, which, since are originally the same profile, are linked and optimized as

one, as explained in section 3.2. Furthermore, the predictive tolerance to exit from the cycle is fixed at 5×10^{-5}, not too low, otherwise the simulations require many iterations, increasing too much the computational time when the noise constraint is active. First an optimization without noise limits is computed, in order to produce reference emissions for the limited simulations. Then, two different setups are tested, the first one includes all the noise contributions, while the second includes only TBLTE and TI. The latter, also, is computed with new updated functions received during the work from the Technische Universität München and developed by *Sucameli*. They mainly modify the computation of the TI noise, as better explained in section 5.2.3.

5.2.1 Aerodynamic reference configuration

As said, firstly it is important to perform a simulation without noise limits to generate a reference configuration. The results of the *free-form* optimization are here presented. It can be noticed how the *free-form* method allows to optimize the tip of the blade. This aspect represents the first goal reached, since the secondary purpose of the work is to show that the recently implemented *free-form* strategy works on turbines different from the 3.35 MW IEA Task 37 used by Bolzoni [3] to test it. As it can be seen, the optimized profile has a more symmetrical shape towards the trailing edge. Indeed, while thicknesses between suction and pressure sides remain similar, it is clear that the camber of the two sides are modified towards a more symmetrical configuration. This has the effect of greatly rise the efficiency of the profile and the AEP of the turbine.

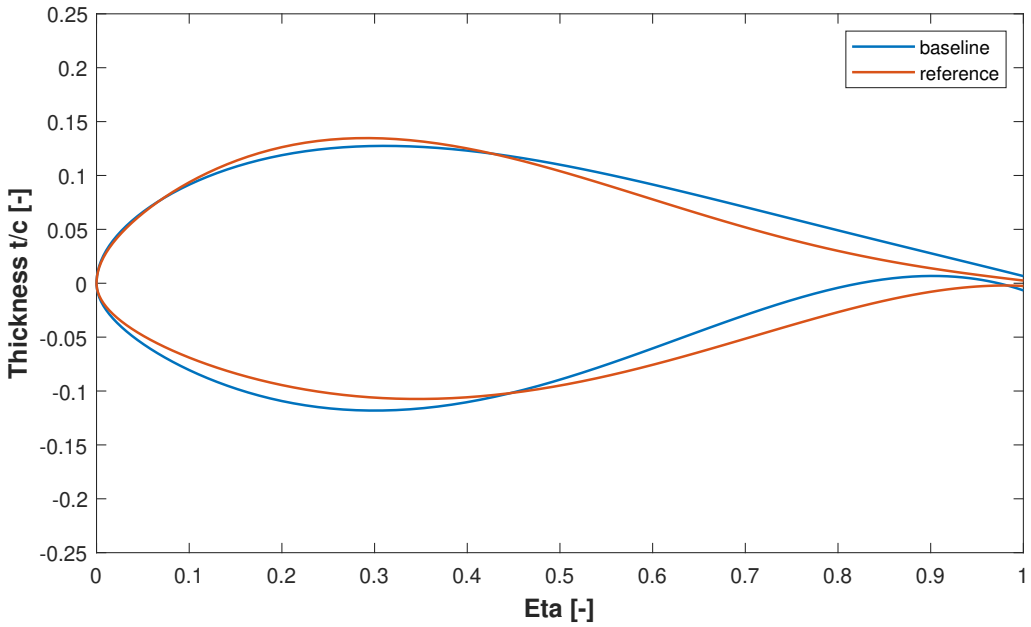

Figure 5.7: FFA-W3-241 airfoil shape optimization in the aerodynamic reference case

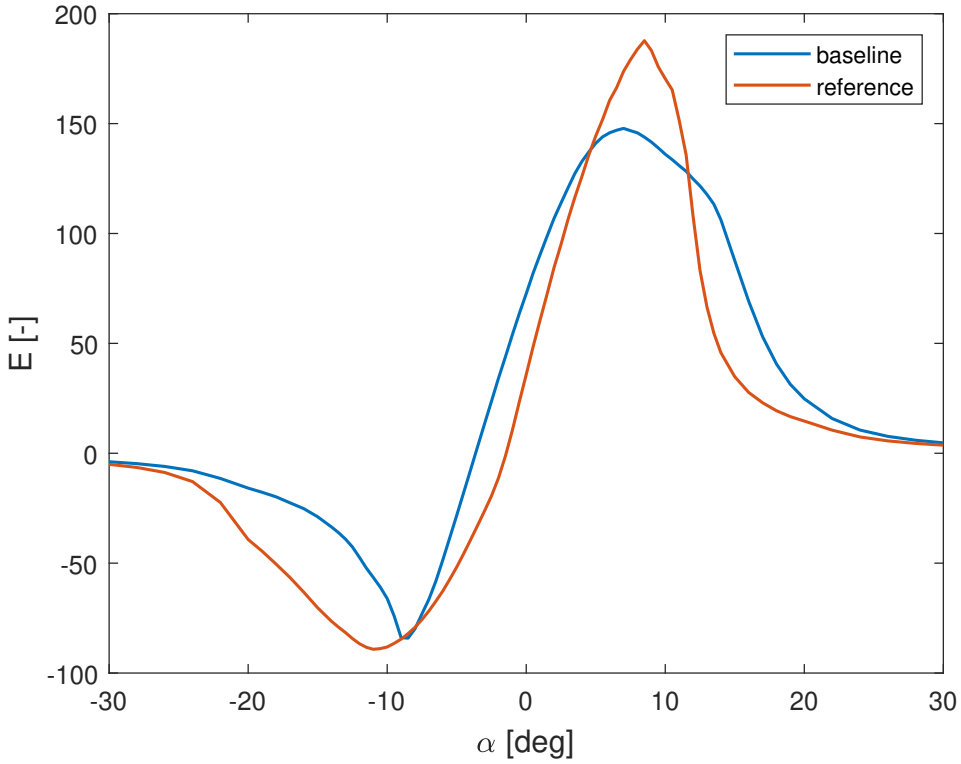

Figure 5.8: Airfoil efficiency comparison between baseline and aerodynamic reference

	AEP	**Cp***	**TSR***	**V**$_r$
final values	51781 MWh	0.4764	8.065	10.4 m/s
variation from	391 MWh	0.0222	0.770	-1.20 m/s
the baseline	0.7608 %	4.89 %	10.56 %	-10.35 %

Table 5.5: Aerodynamic parameters in the aerodynamic reference case

After the aerodynamic cycle is completed, the noise analysis tool is used to evaluate sound emissions. In Fig. 5.9, it is possible to notice the OASPL A-weighted values for each wind speed and noise spectra for V_{wind} = [7 9 11 13 19] in m/s. Those are the speeds for which the noise constraint will be active in the next simulations, as better explained later. In Tab. 5.6 are shown total and specific OASPL A-weighted values for the previous defined set of velocities.

Wind speed	**7 m/s**	**9 m/s**	**11 m/s**	**13 m/s**	**19 m/s**
OASPL$_A$ Total	59.31	63.62	71.19	71.87	72.47
OASPL$_A$ TI	48.84	48.04	52.73	51.28	55.93
OASPL$_A$ TBLTE	41.15	45.48	52.40	52.89	53.94
OASPL$_A$ TEB	58.95	63.46	71.04	71.77	72.30

Table 5.6: OASPL$_A$ [dB] in aerodynamic reference case

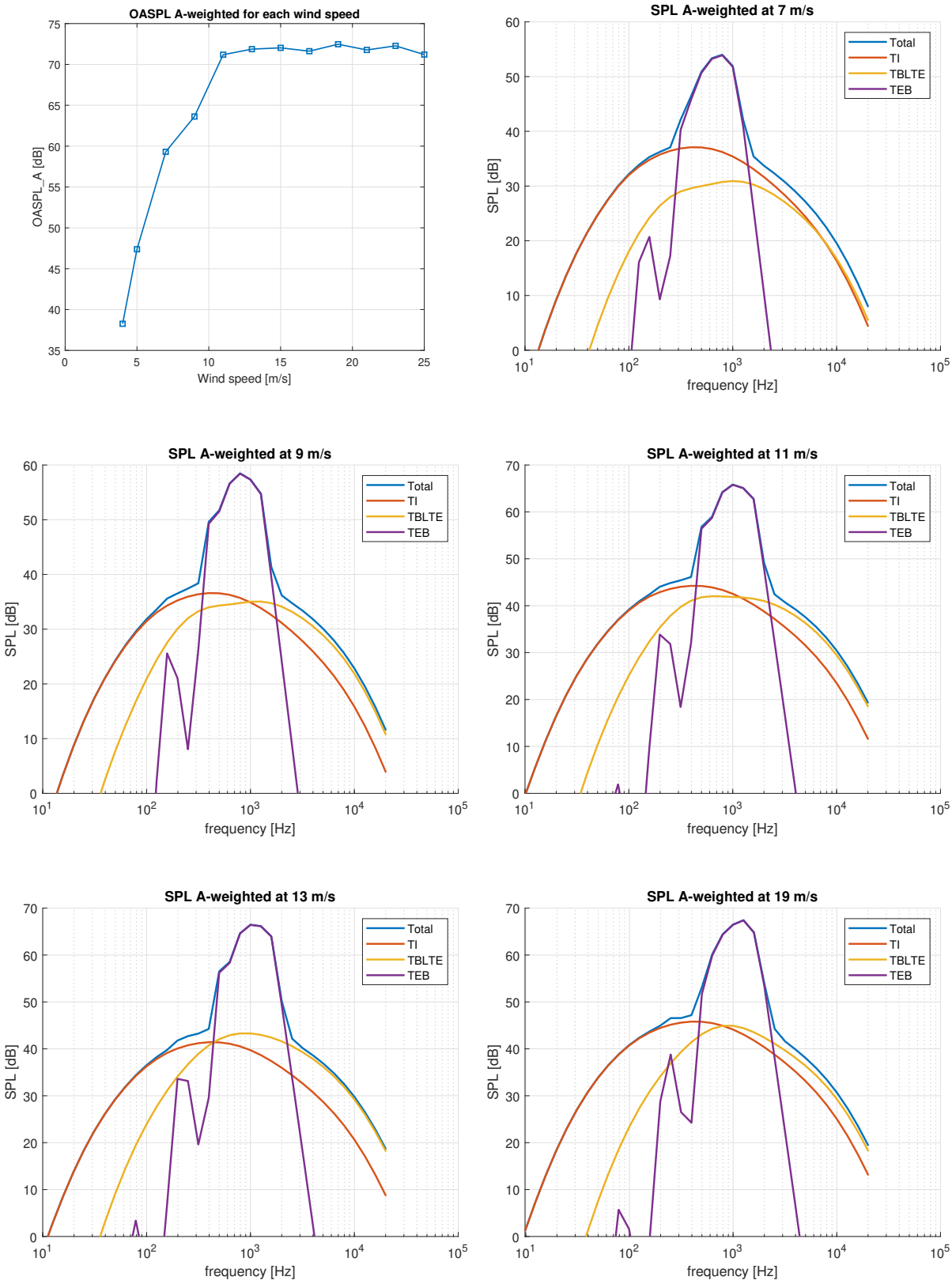

Figure 5.9: $OASPL_A$ values and noise spectra in aerodynamic reference case

As it is clear, for every wind speed TEB noise is by far the most important contribution, followed by TI and TBLTE. Due to the great difference between the contributions,

Cp-Max will mainly try to reduce TEB source when the constraint on noise emissions will be activated.

5.2.2 Aerodynamic optimization with noise constraints

The first simulation includes all the noise contributions. It is performed to see the influence of the airfoils shape on each source, and how the performances are affected by the introduction of the new constraint. Noise analyses are performed for five different wind speeds, $V_{selected}$ = [7 9 11 13 19] m/s. As it can be seen from Fig. 5.9, for a wind velocity higher than the reference one, 10.4 m/s, the emissions are very similar, having a nearly flat behavior. For this reason, it is useless to compute noise spectra for each velocity, but it is sufficient to select only few. The speeds are chosen based on three considerations:

- 19 m/s is included since it produces the highest OASPL A-weighted in the reference case;
- even if they have no impact in respecting a legal norm, low velocities are included to see the influence of the *free-form* method on the emissions of the whole working range;
- are included the velocities next to the rated one, which depends on the aerodynamic optimization, to understand the impact of its variation on noise emissions.

For each wind speed, noise limit on the OASPL A-weighted is fixed 1 dB lower than the reference value, Tab. 5.6, which corresponds to a reduction of noise amplitude around 22 %. While this is not necessary for a real design process, it is done to verify the trend of noise emissions at different velocities, in order to understand if noise is always reduced and if its variations are similar.

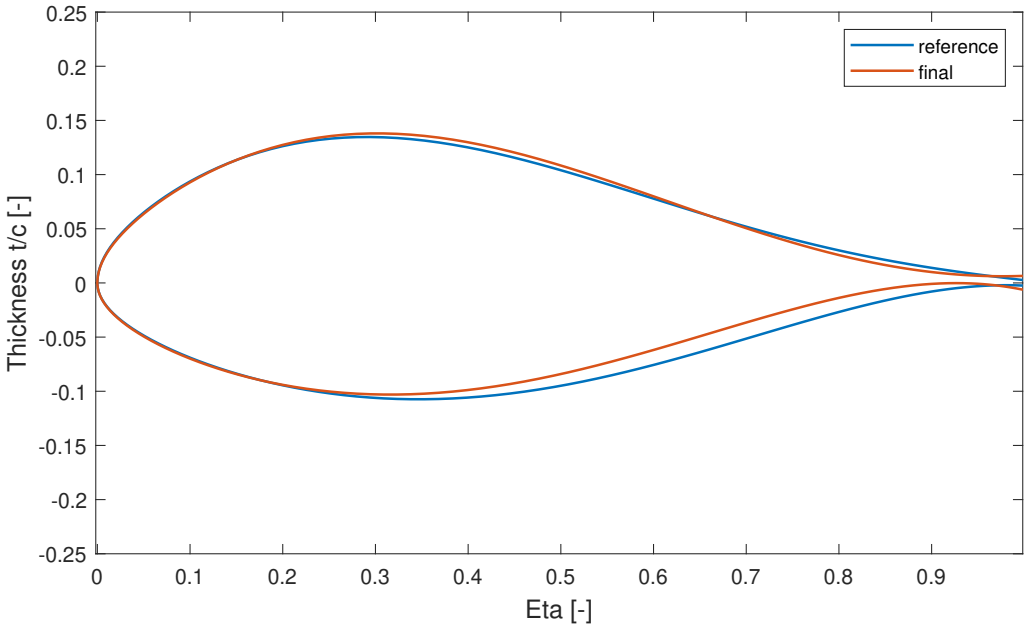

Figure 5.10: FFA-W3-241 airfoil shape optimization considering the first test performed

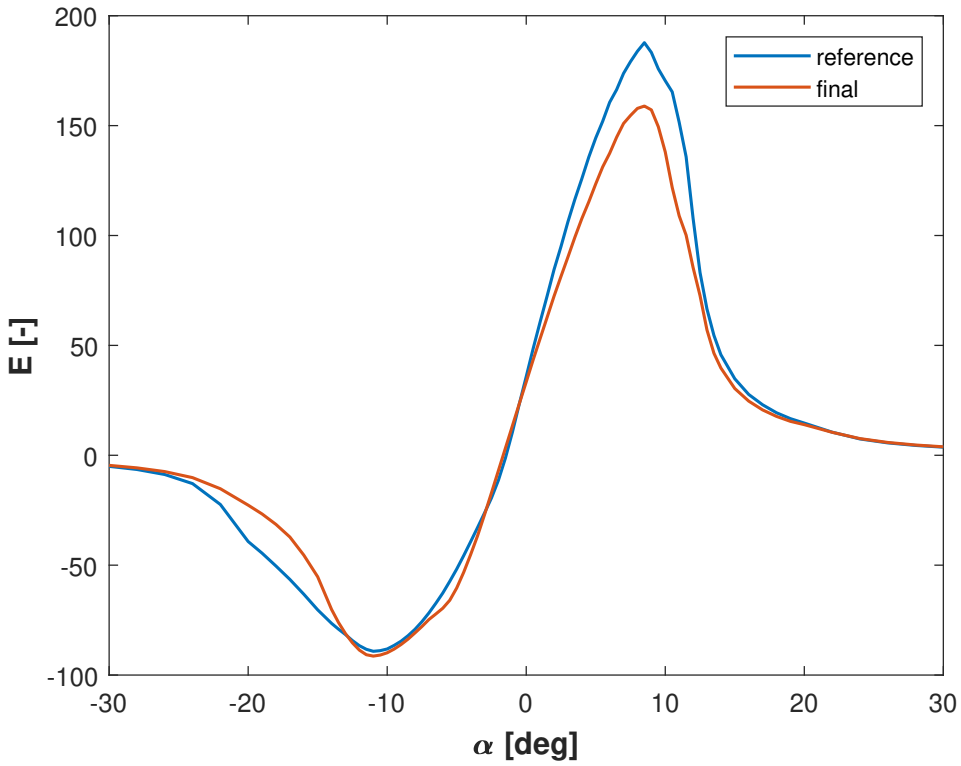

Figure 5.11: Airfoil efficiency comparison considering the first test performed

	AEP	**Cp***	**TSR***	**V**$_r$
final values	51634 MWh	0.4724	7.757	10.8 m/s
variation from reference	-147 MWh -0.28 %	-0.0040 -0.80 %	-0.3080 -3.82 %	0.40 m/s 3.85 %

Table 5.7: Aerodynamic parameters considering the first test performed

As we can see from Fig. 5.10, the profile is mainly modified towards the trailing edge, in particular, the shape is thinner in this region. This was expected, because the TEB contribution, which drives the simulation, can be reduced by limiting the trailing edge thickness. This has an impact on the efficiency of the profile, which is especially reduced for angles of attack between 5° and 10°. Still, as reported in Tab. 5.7, the impact on the aerodynamic variables is little, showing the goodness of the idea at the base of the thesis.

Noise results are now presented. To avoid a long list of figures, overall noise spectra are reported for each wind speeds, while spectra for every specific contribution are shown only for 13 m/s. Moreover three solutions are shown:

- reference spectra;
- approximated results that are computed at the end of the aerodynamic cycle but that retrieve data from *Cp-Lambda* simulations run at the start of the aerodynamic module, as explained in section 4.3;
- final results computed at the end of the optimization, as in the reference case.

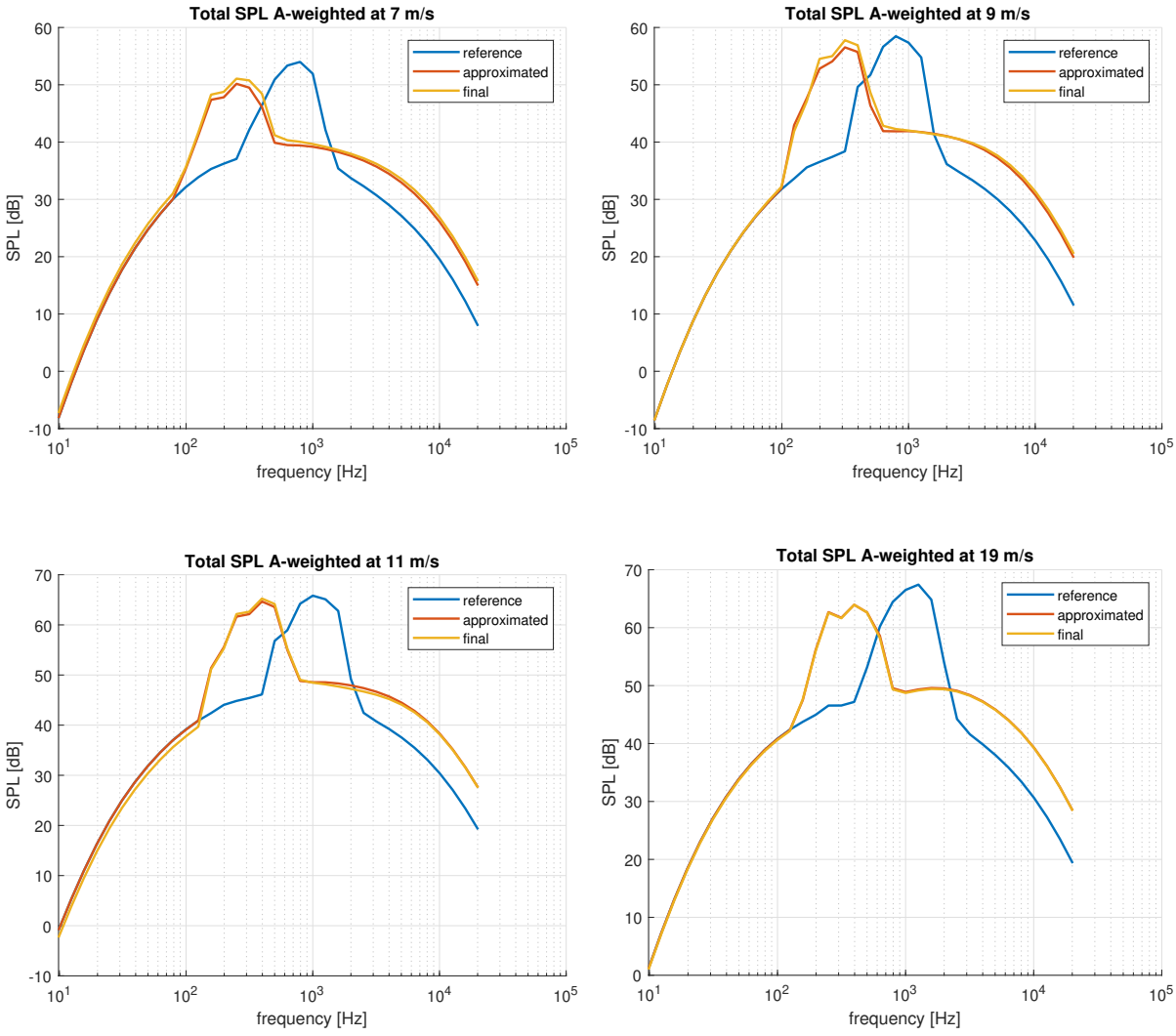

Figure 5.12: Total A-weighted noise spectra considering the first test performed

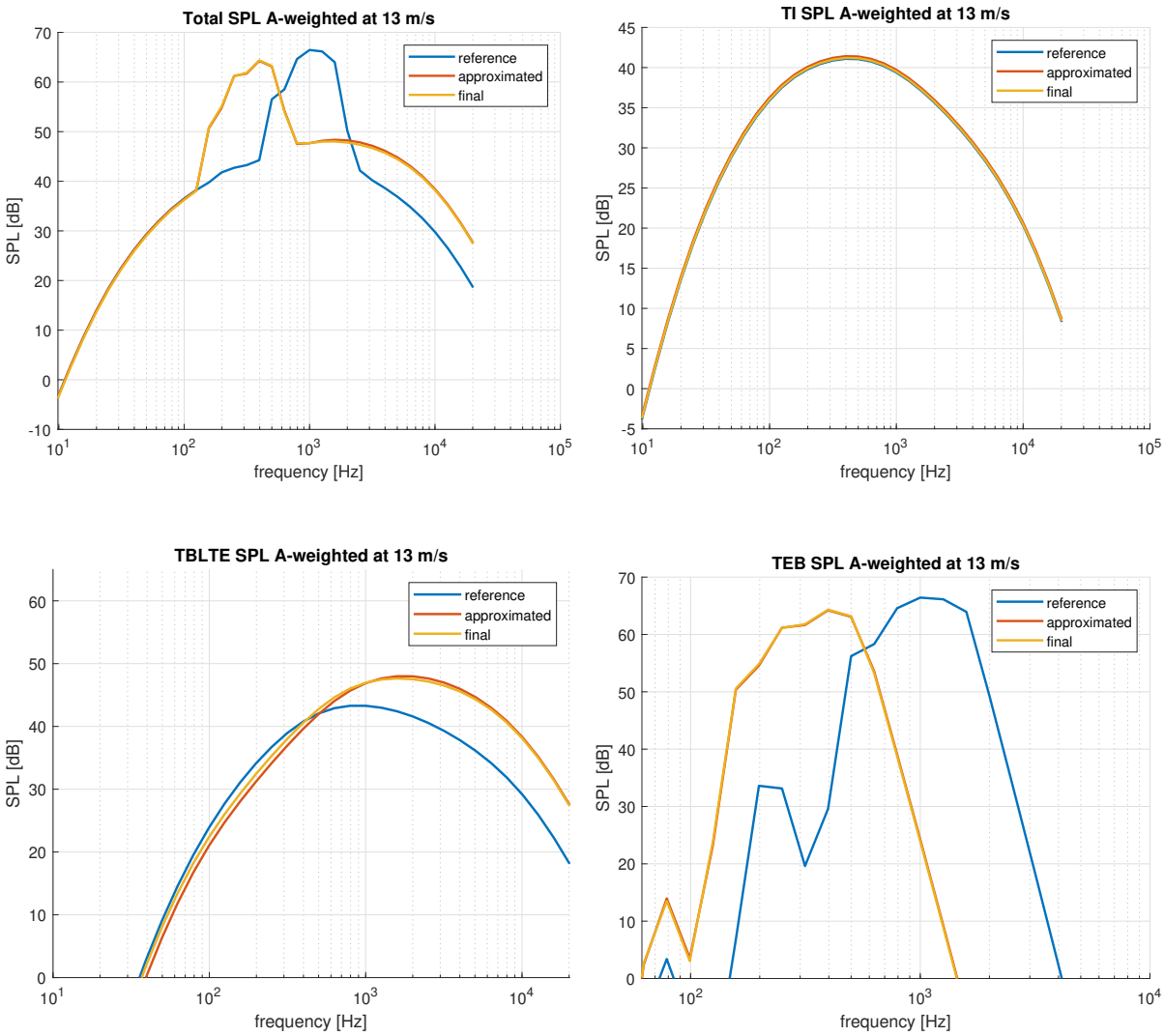

Figure 5.13: Total and specific noise spectra for 13 m/s considering the first test performed

Wind speed	**7 m/s**	**9 m/s**	**11 m/s**	**13 m/s**	**19 m/s**
OASPL$_A$ Total	57.51	62.94	70.32	69.49	69.75
Δ approximated	1.08	1.11	0.45	0.07	-0.08
Δ reference	-1.79	-0.67	-0.87	-2.38	-2.71
OASPL$_A$ TI	48.26	46.79	52.98	51.39	55.85
Δ approximated	-0.16	0.99	0.06	-1.44	-0.22
Δ reference	-0.58	-1.25	0.25	0.11	-0.08
OASPL$_A$ TBLTE	47.61	51.84	57.68	57.27	57.91
Δ approximated	0.63	0.70	0.26	-0.14	-0.11
Δ reference	6.47	6.36	5.28	4.38	3.98
OASPL$_A$ TEB	56.43	62.48	69.99	69.15	69.26
Δ approximated	1.16	1.18	0.51	0.08	-0.07
Δ reference	-2.53	-0.98	-1.05	-2.62	-3.04

Table 5.8: OASPL$_A$ [dB] values and variations considering the first test performed

As it can be seen, the simulation is successful and the maximum OASPL$_A$ of the reference case is reduced by at least 1 dB. It is now possible to make some considerations. As expected the simulation is driven only by TEB contribution due to its greater amplitude respect to the other sources. This is clear by noting the final values of TBLTE, which have now double or quadruple amplitude. Further tests on a machine in which TEB and TBLTE contributions are similar should be performed in order to verify if it is possible to reduce both sources at the same time.

The second observation is that noise is reduced for each wind speeds showing that the shape of the blade has similar impact on the whole working range of the wind turbine. Thus, the reduction is different for each wind speed and now the maximum OASPL$_A$ is found not for 19 m/s but for 11 m/s and, even if the values are close, this aspect is still a little concerning. However, in noise analyses performed for all the twelve wind speeds it is found a nearly flat behavior for velocities higher than the reference one, so it is expected that the other emissions not computed are reduced during the optimization and close to the maximum OASPL$_A$ found for 11 m/s.

Another aspect to underline is how the approximated results are really close to the final values for wind speeds higher than the baseline reference one, whereas for the others the approximation is less reliable. A possible explanation is given by looking at the regulation trajectories that describe approximated and final configurations, Fig. 5.14. The approximated control laws correspond to the baseline ones, since they are determined at the start of the aerodynamic block, before entering the cycle. The optimization has the effect of improving the Cp, of increasing the optimal TSR and of decreasing the rated velocity. Those modifications have the consequence of increasing the optimal rotational velocity in region II of the turbine, for wind speeds lower than the reference one. This proves the strong impact of the rotational speed on noise emissions, but also the direct effect of the shape for high wind speeds. Indeed, in this region the required rotational velocities are the same and the difference in noise emissions is directly linked to the different shape of the airfoil.

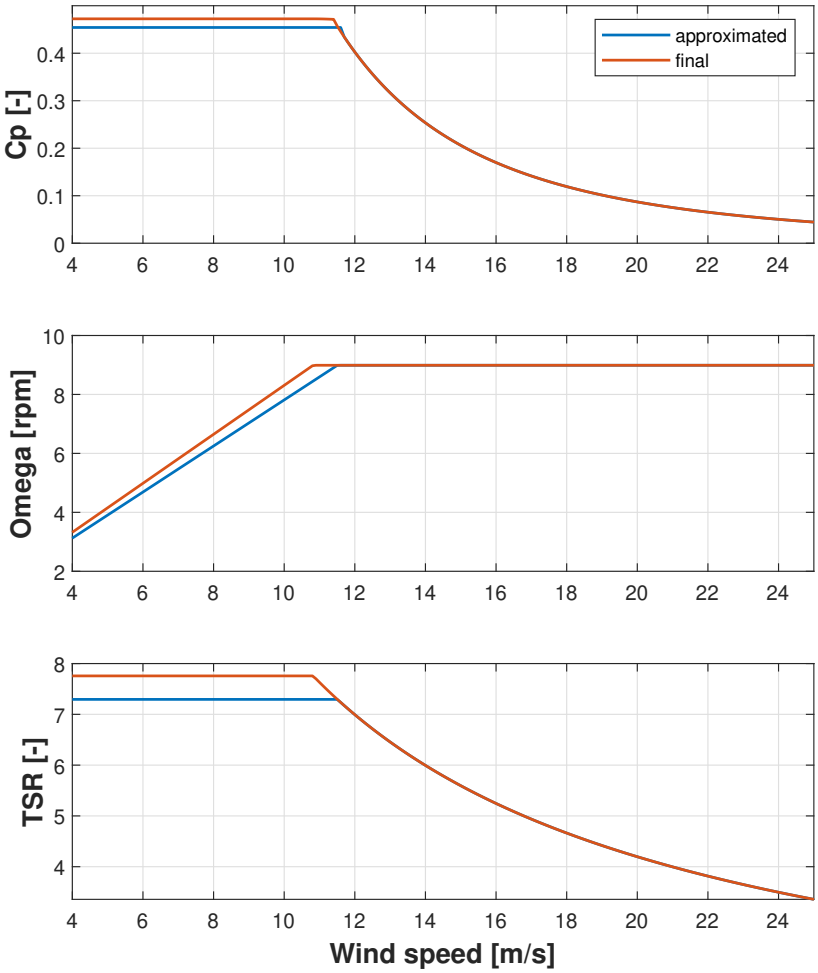

Figure 5.14: Trajectories comparison: approximated and final solution considering the first test performed

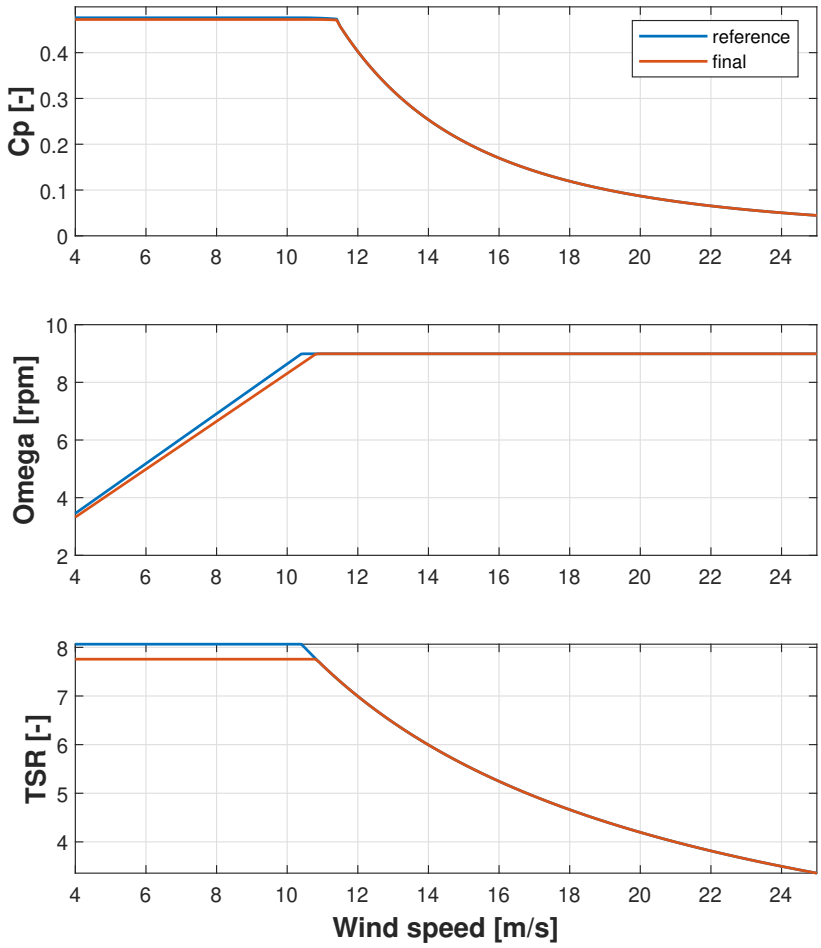

Figure 5.15: Trajectories comparison: reference and final solution considering the first test performed

It is interesting to notice, from Figs. 5.12 and 5.13, that TEB contribution is not simply reduced, but its peak has been shifted to frequencies for which the human hearing is less sensible. Indeed, the OASPL is actually increased, so noise emissions are even higher, but human noise perception is lower. This aspect must be underlined because it shows the complexity of aeroacustic analysis and it represents an innovative solution automatically found by the code.

It must be noted, also, the effect of the airfoil shape modification on the noise emissions computed inside the aerodynamic cycle, when the data retrieved from *Cp-Lambda* simulations are always the same. In Figs. 5.16 and 5.17 are represented noise spectra in first and last iteration. As it can be seen, the *free-form* optimization has already reduced the noise emissions of the profile. This can be justified

by considering that noise emissions are reduced for thinner boundary layers, which also improves the aerodynamic performances. Moreover, as it is expected, while TEB and TBLTE are affected by the shape modification, TI contributions are not modified. Nevertheless, as previously shown, the TI final emissions are different both from the approximated and reference ones. In fact, the airfoil shape does not influence directly the contribution but it impacts the regulation trajectories and the turbine behavior in dynamic simulations, which have an influence into it. In the implemented architecture TI contribution cannot be controlled, since regulation trajectories and dynamic simulations are computed only before and after noise constraint computation. This is an expected limit of the architecture, but it is important to notice that the contribution, in this case, is slightly reduced. This trend must be check in the following simulations. The consideration proves, also, the complexity of designing a wind turbine and how each parameter can be influenced and can influence other aspects of the turbine in a direct or indirect manner.

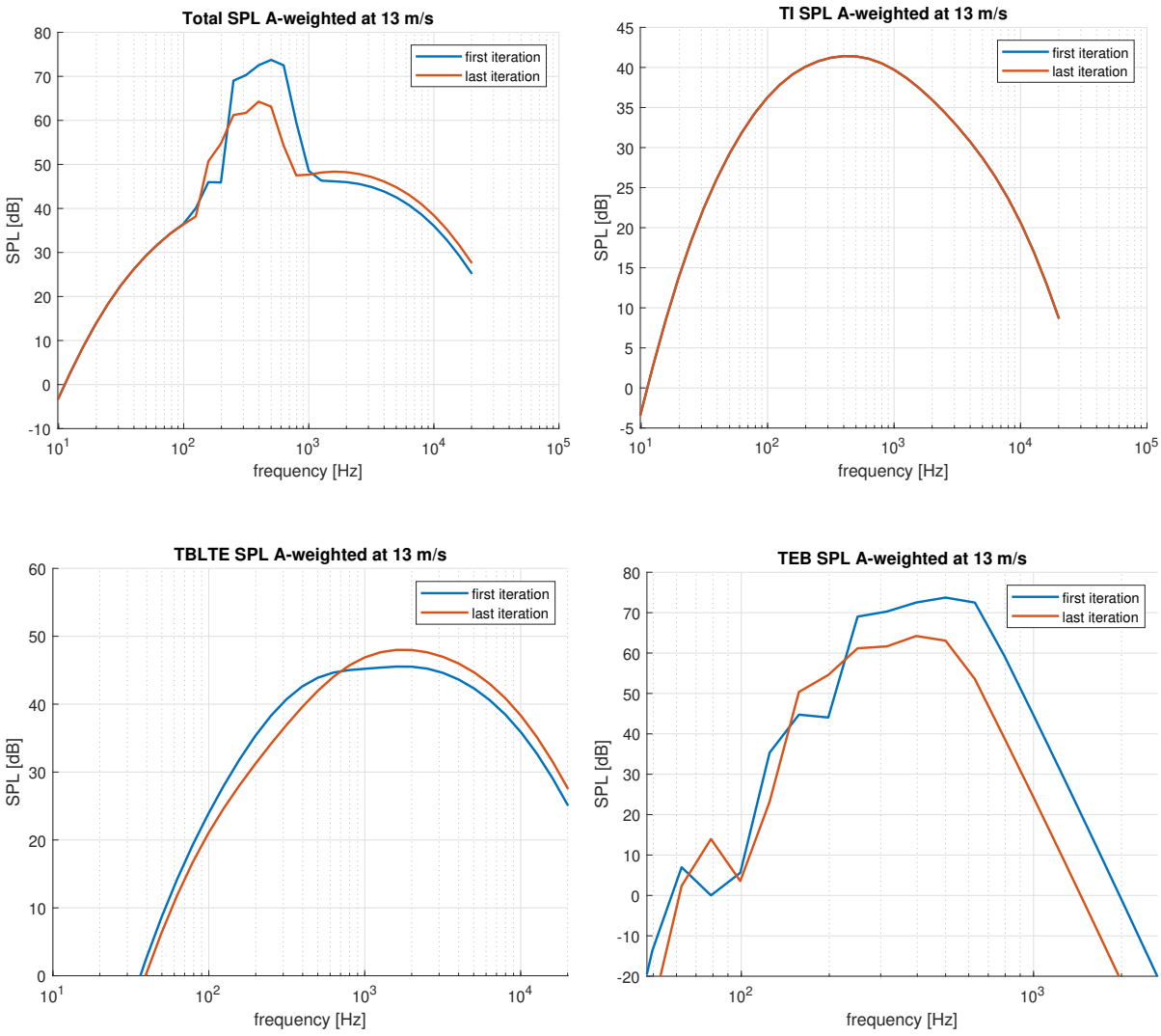

Figure 5.16: Comparison between noise spectra in first and last iteration considering the first test performed

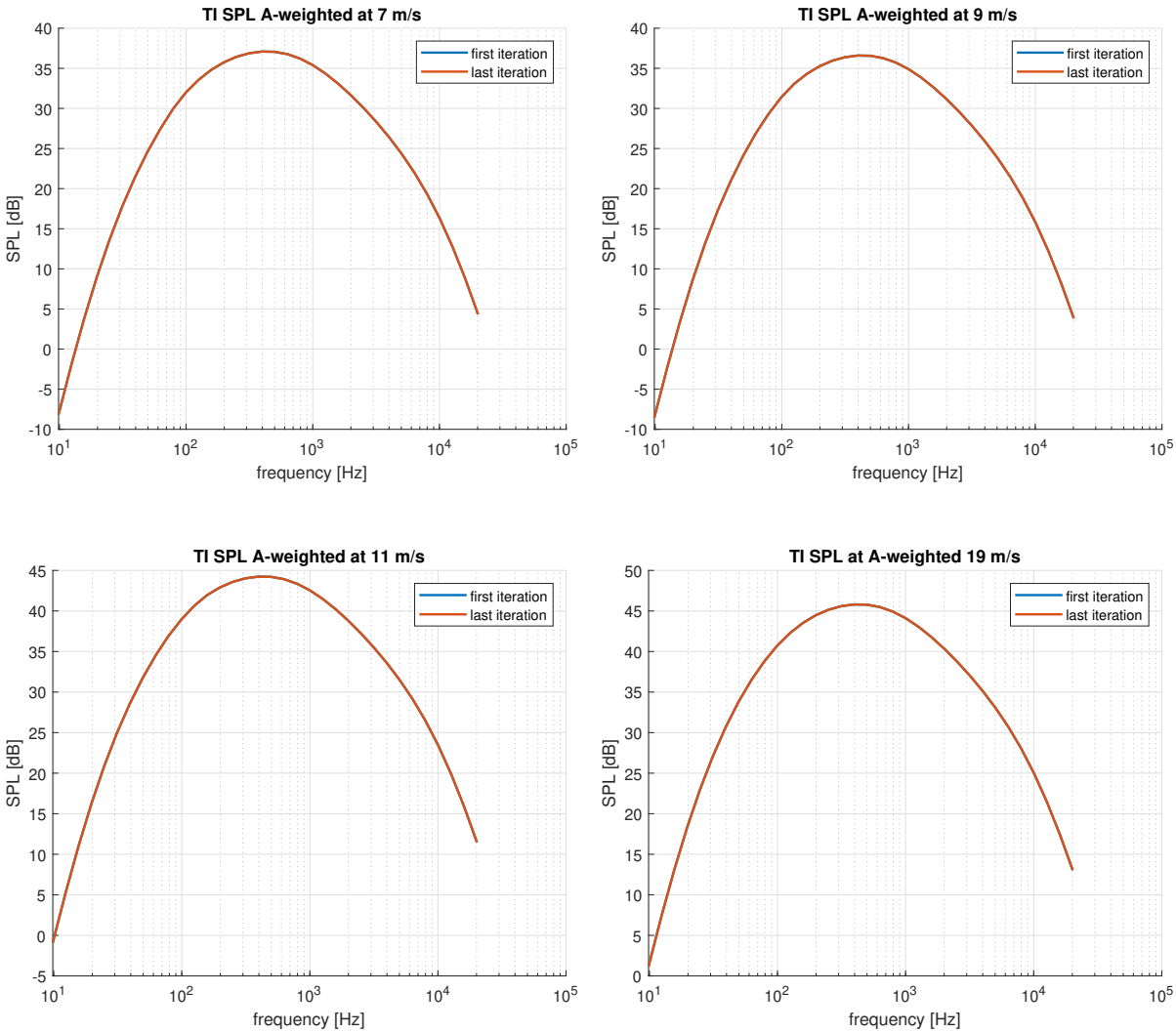

Figure 5.17: Comparison between TI noise spectra in first and last iteration considering the first test performed

5.2.3 Aerodynamic optimization with updated functions

During the last two weeks of the work, a new update of the noise analysis tool is received from the Technische Universität München. The new implementations, done by *Sucameli*, fixed some little computation errors and more importantly modify how the turbulent inflow noise is computed. In particular, a new definition to the turbulence computation is given. The latter is evaluated always on the same revolution sector of the wind turbine, in order to eliminate effects caused by wind shear and asymmetries. This is particularly important because, while TBLTE and TEB noise are not changed, the TI contribution is strongly reduced. In Fig. 5.18 are compared the TI noise spectra of the reference case with old and new functions, while in Fig. 5.19 are shown the new noise reference spectra. The reduction has little influence on the total SPL A-weighted

when all the contributions are considered, due to the high values of the TEB noise. However, it must be noted that now the TI noise is smaller than the TBLTE.

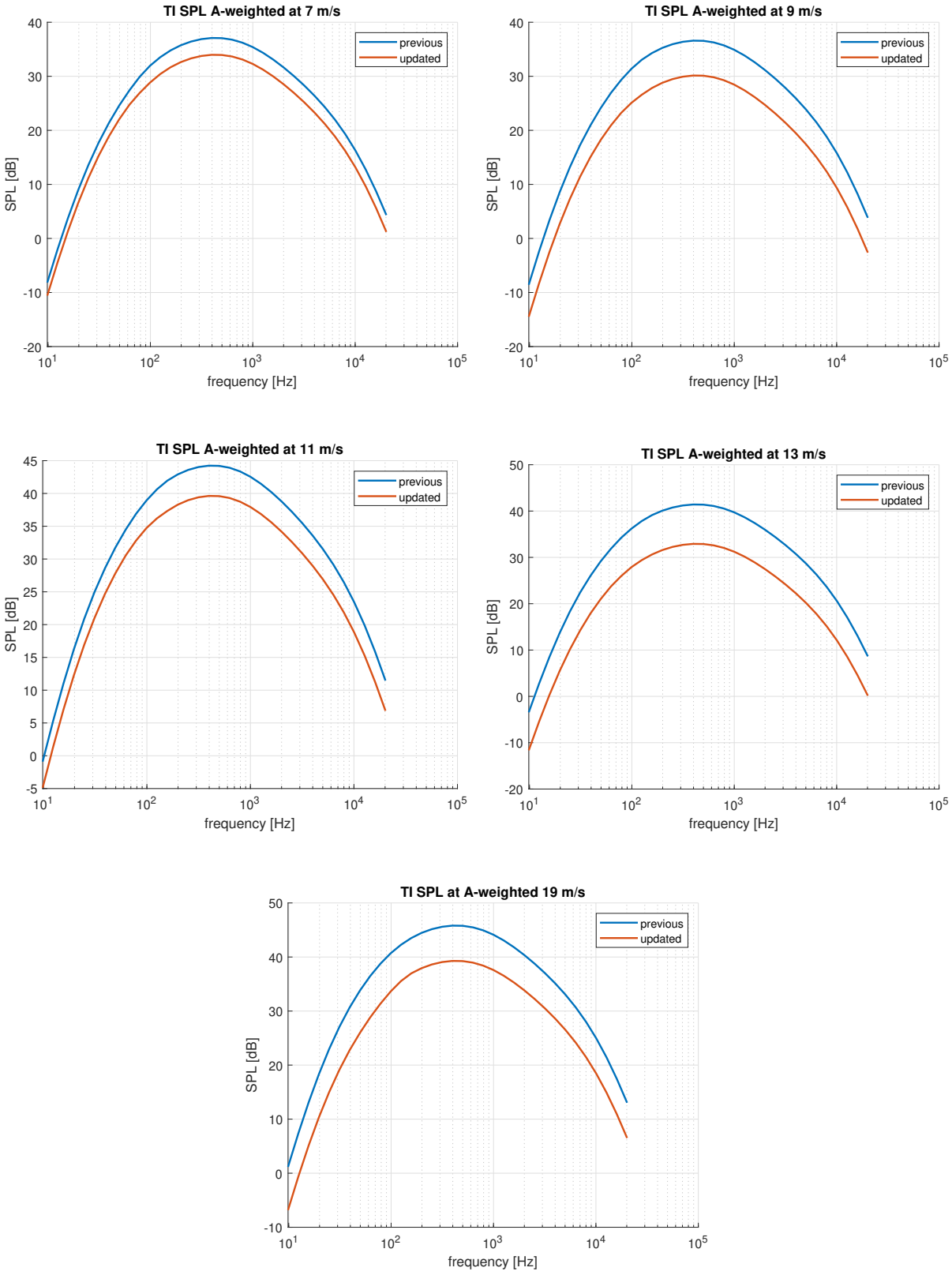

Figure 5.18: TI noise spectra comparison between old and new functions

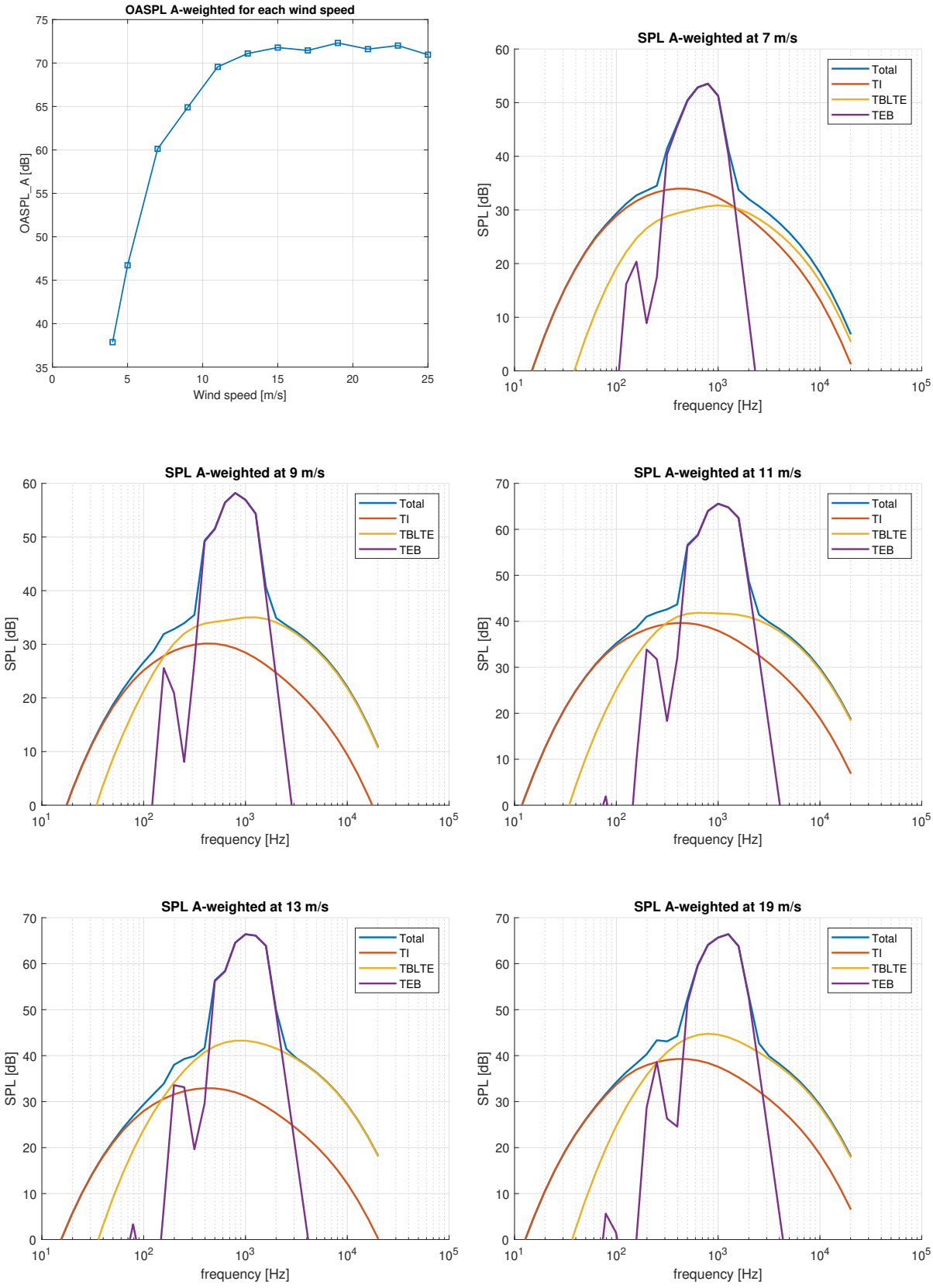

Figure 5.19: Reference spectra recomputed with updated functions

Wind speed	7 m/s	9 m/s	11 m/s	13 m/s	19 m/s
OASPL $_A$ Total	47.57	48.26	52.65	52.75	54.73
OASPL $_A$ TI	45.78	41.59	45.48	41.65	46.64
OASPL $_A$ TBLTE	42.85	47.21	51.72	52.40	53.99

Table 5.9: OASPL $_A$ [dB] reference values with updated functions

As said, the TEB noise may be overestimated and is usually of secondary importance in smaller machines. For these reasons, during this simulation it is not considered. This is done, also, to study if it is possible to reduce noise emissions and how the shape of the airfoil is modified when the driving contribution is the TBLTE noise. Wind speeds considered are always the same, $V_{selected}$ = [7 9 11 13 19] m/s, and the goal is to reduce by 1 dB not all the noise emissions, as in the previous case, but only the maximum reference one, 54.73 dB. It must be remarked, also, that only the shape of the last airfoil is modified, while the other geometry properties, as the chord and the twist, are not included inside the cycle.

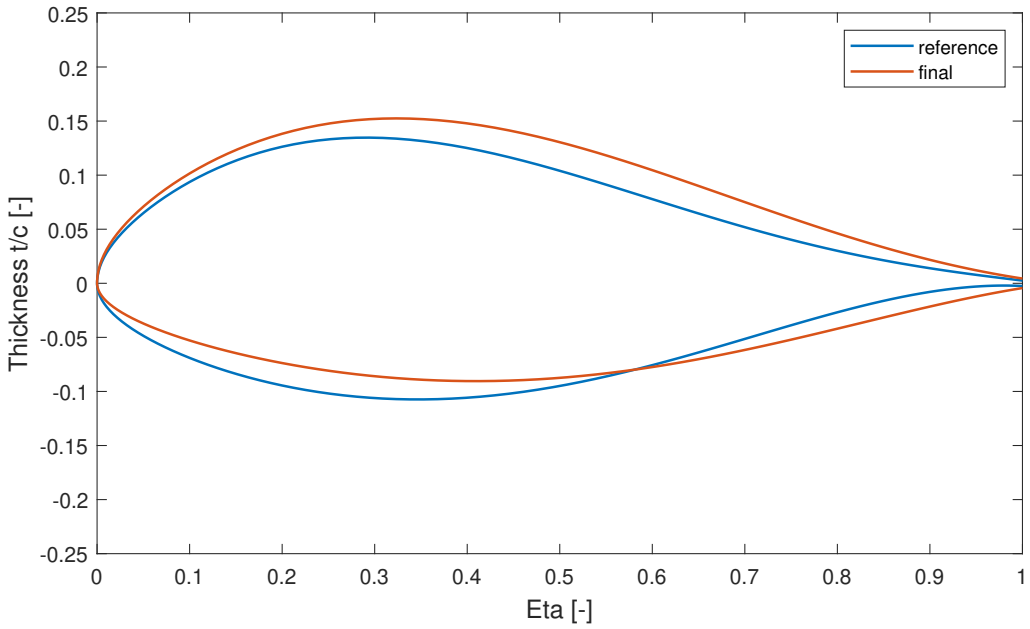

Figure 5.20: FFA-W3-241 airfoil shape modification considering the second test performed

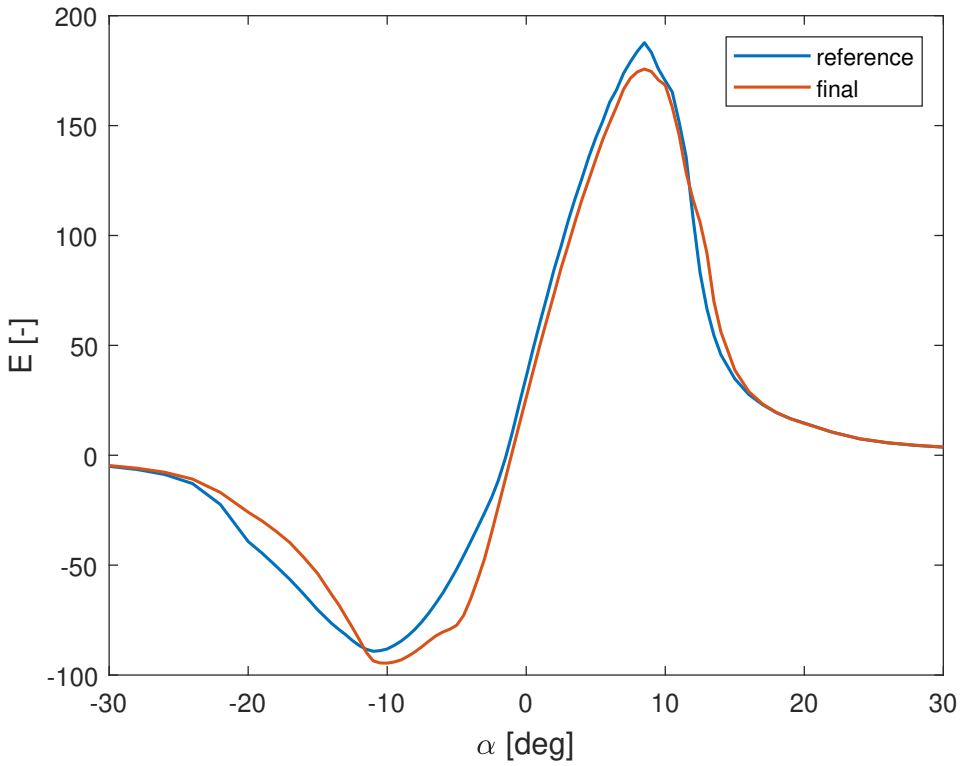

Figure 5.21: Airfoil efficiency considering the second test performed

	AEP	**Cp***	**TSR***	**V_r**
final value	51774 MWh	0.4762	8.0047	10.4 m/s
variation from reference	-7 MWh -0.01 %	-0.0002 -0.04 %	-0.0018 -0.22 %	0 m/s 0 %

Table 5.10: Aerodynamic parameters considering the second test performed

As we can see the profile is modified in a much different way than in the previous case. Indeed, the profile is now thicker near the trailing edge and the pressure side is more transformed towards a flat plate. This difference between the two cases shows, again, that further simulations should be performed to find if it is possible to reduce at the same time both TEB and TBLTE. It is interesting to notice that the AEP is almost exactly the same found in the reference case. This is probably due to the high tolerance of the aerodynamic cycle, which stops the optimization before it is able to find the unique most performing airfoil shape. Nevertheless, the similarity of the aerodynamic results proves again that is possible to reduce noise emissions without

strongly impacting the aerodynamic performances, as it happens when the maximum tip velocity is reduced.

Wind speed	**7 m/s**	**9 m/s**	**11 m/s**	**13 m/s**	**19 m/s**
$OASPL_A$ Total	46.50	46.46	51.65	51.64	53.26
Δ approximated	1.31	1.58	-1.65	-0.33	-0.98
Δ reference	-1.07	-1.80	-1.00	-1.12	-1.47
$OASPL_A$ TI	45.30	40.13	45.08	41.62	45.79
Δ approximated	1.13	-0.22	-4.77	-1.51	-3.63
Δ reference	-0.48	-1.46	-0.40	-0.03	-0.85
$OASPL_A$ TBLTE	40.31	45.31	50.57	51.18	52.40
Δ approximated	1.92	2.32	-0.12	-0.18	-0.10
Δ reference	-0.80	-0.14	-1.74	-1.69	-1.59

Table 5.11: $OASPL_A$ values and variations in dB considering the second test performed

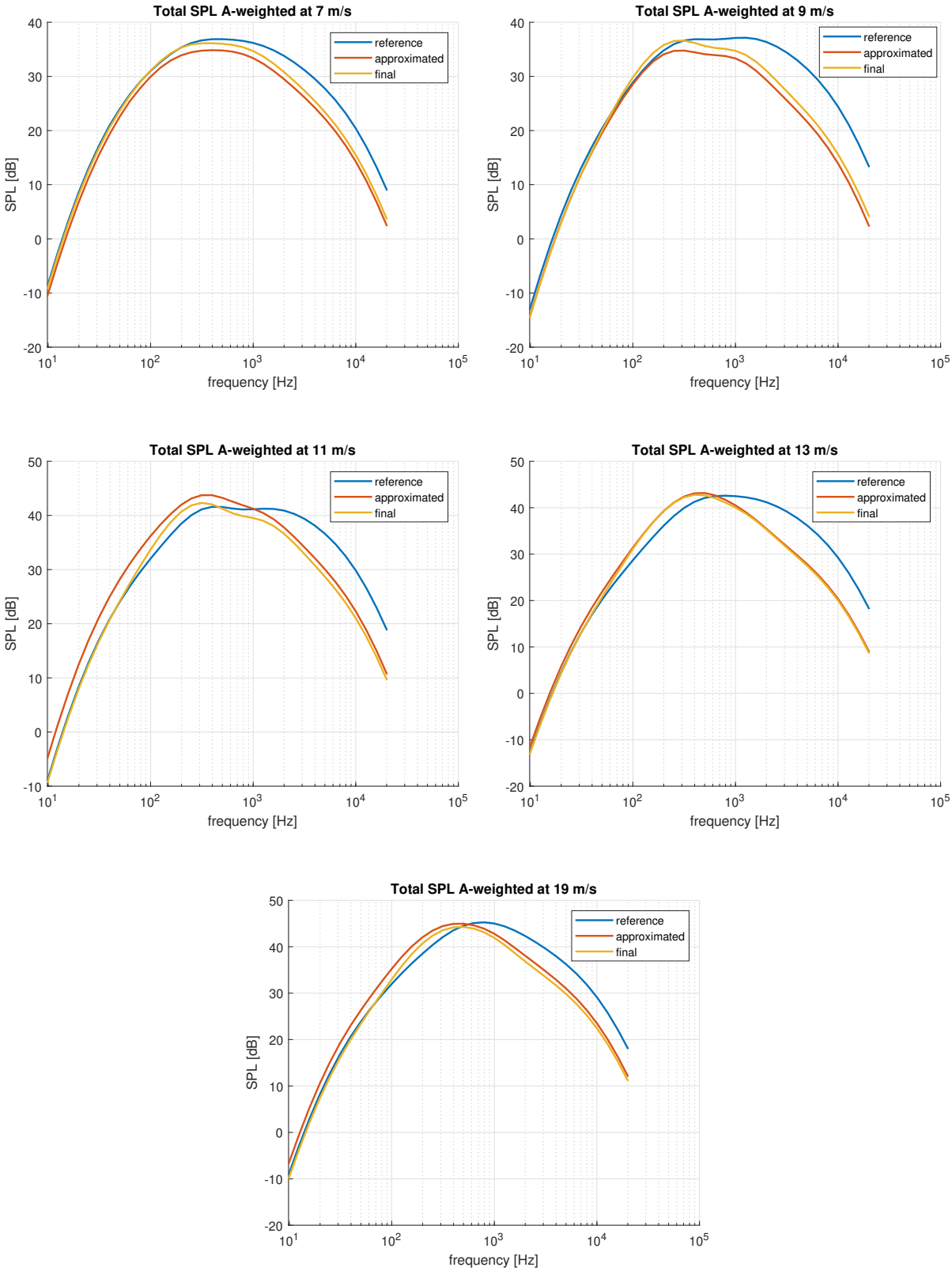

Figure 5.22: Total A-weighted noise spectra considering the second test performed

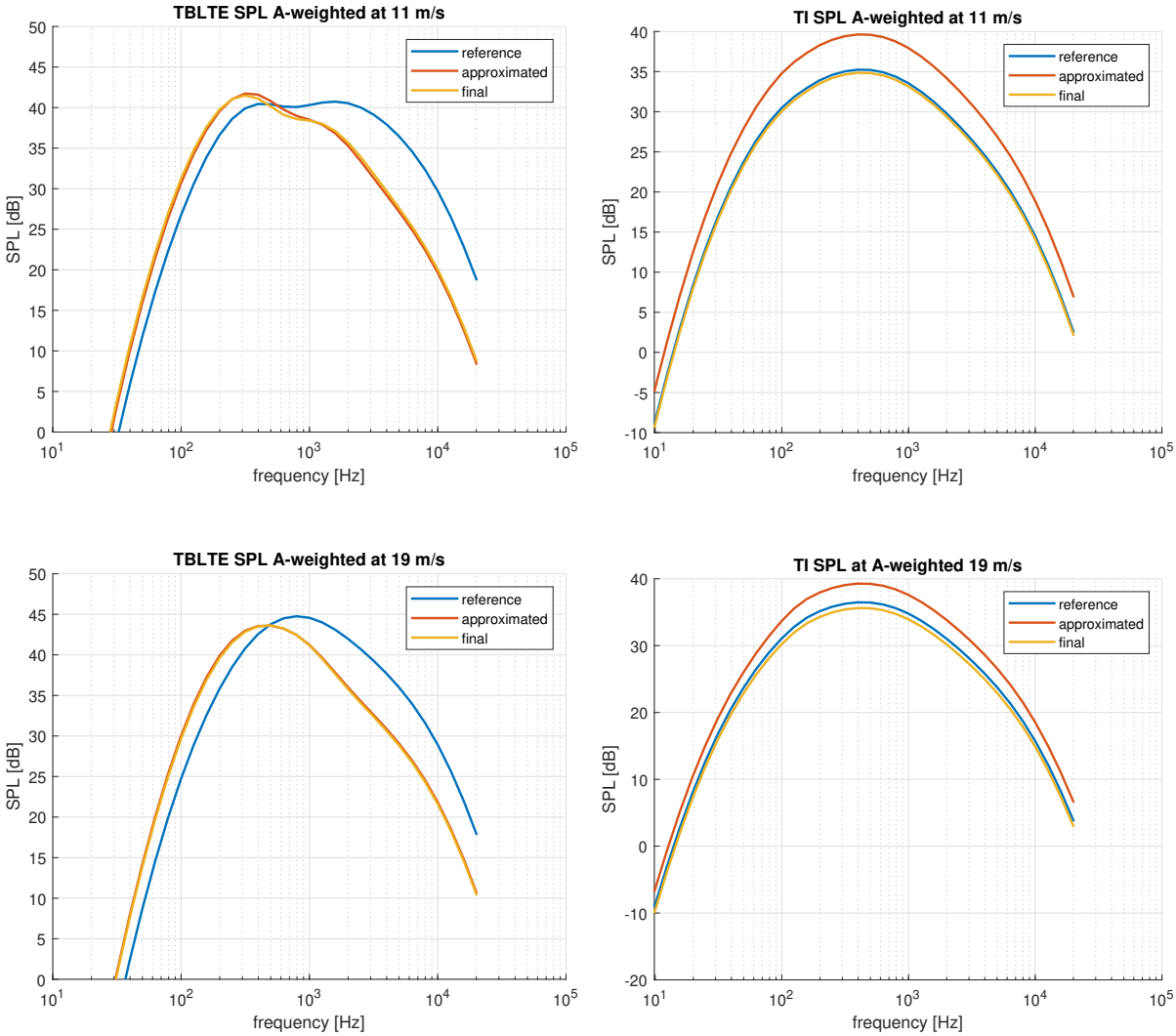

Figure 5.23: Specific noise spectra for 11 m/s and 19 m/s considering the second test performed

OASPL A-weighted are shown in Tab. 5.11. As in the previous case, the noise emissions are reduced for each wind speed, proving that the shape of the blade has a general effect on the whole working range of the machine. The TBLTE is the only driving contribution of the optimization, since due to the architecture of the implementations, inside the cycle the TI is always computed in the same way. The differences between the TBLTE approximated results and final one can be explained once again by looking at the regulation trajectories, Fig. 5.24. Also in this case, for low velocities the optimal rotational speed of the machine is increased, which has the effect of also increasing noise emissions, whereas for high wind speeds the differences are much smaller since the required rotational speed is the same. Moreover, the regulation trajectories of the final and the reference case are nearly identical, Fig. 5.25. From this

aspect is possible to conclude that the noise emissions are mainly reduced by the direct influence of the shape on noise production, proving again how powerful and flexible is the *free-form* method.

More analyses should be performed to better understand the newly implemented TI contribution. Indeed, the variations between the approximated results and the final ones are sensible and it does not exist a real trend. Instead, the results between the reference emissions and the final ones are closer and similar for each wind speed. Nevertheless, also in this case the final emissions are lower than reference values.

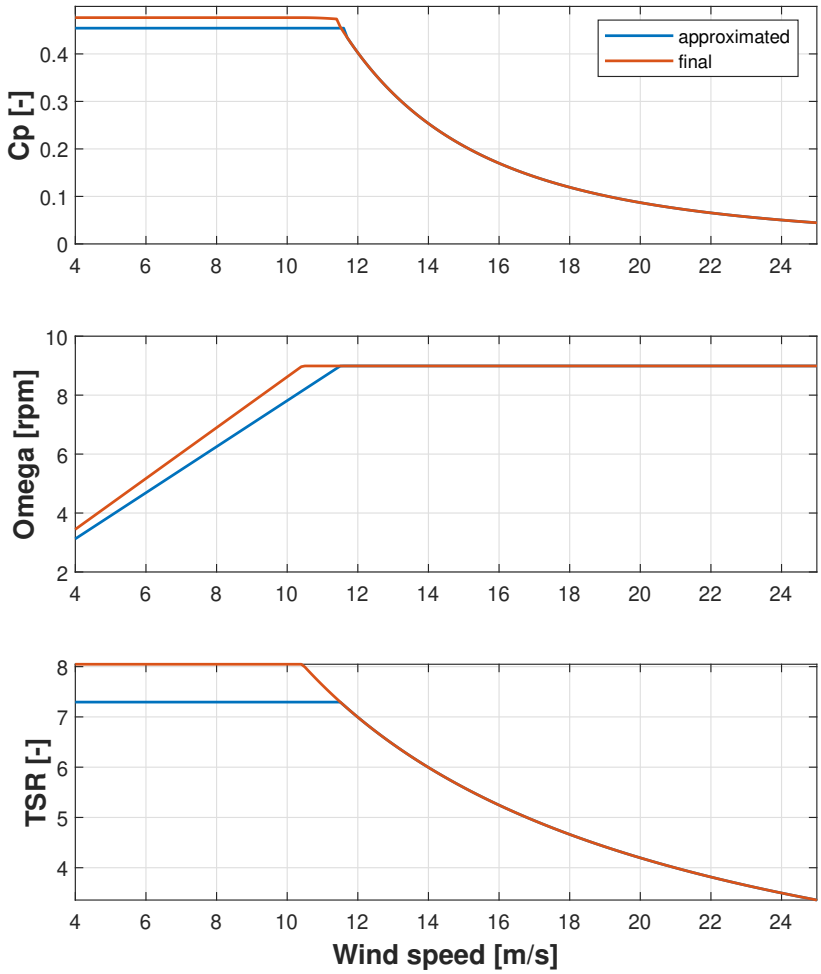

Figure 5.24: Trajectories comparison: approximated and final solution considering the second test performed

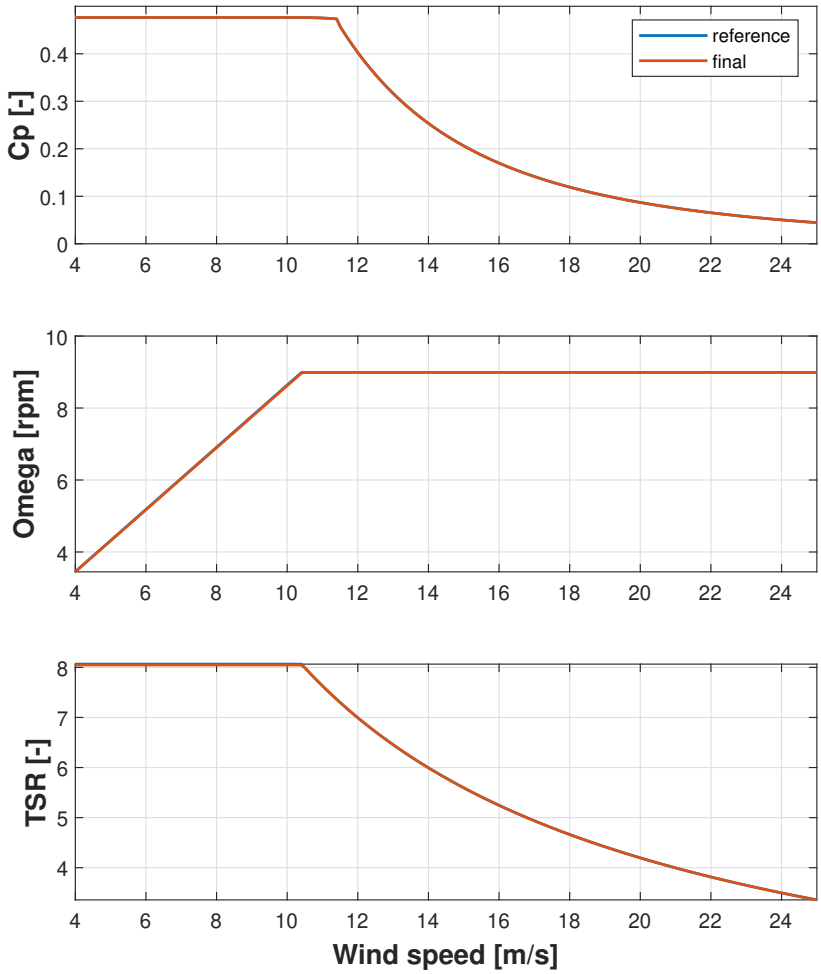

Figure 5.25: Trajectories comparison: reference and final solution considering the second test performed

5.3 Global simulations

In the second set of simulations are performed macro design optimizations. This time, also the second and third poles, η = [0.261, 0.65], of the piece-wise cubic hermite interpolating polynomials that describe the chord distribution are activated, meanwhile the twist one is still considered frozen, since its optimization increases a lot the computational time. Moreover, structural components are also modified, but are run only DLCs 1.1, so normal power production, and DLCs 2.3, corresponding at a grid fail during an extreme wind gust that is probable to happen once a year, EOG 1 visible in Fig. 5.26. This is done to reduce the computational time, but at the same time,

to include a condition that generates strong bending loads on the rotor. Moreover, the structural submodule is included mostly to see if it has any impact on final noise emissions and to be able to compute the CoE of the machine. For these reasons, an accurate and complete analysis is not performed. Also, as said, *WTPerf* cannot be used with prebent blades, so prebend optimization is excluded. Furthermore, similar structural components are linked together and optimized in the same way. In particular: shell panels have the same thickness; the two spar caps have the same distribution; front and rear webs are identical, while the rear web is optimized independently. Also in this case, the first simulation is computed without the noise constraint and it will be considered as the reference configuration. Finally, the emissions are evaluated once the optimization processes are concluded.

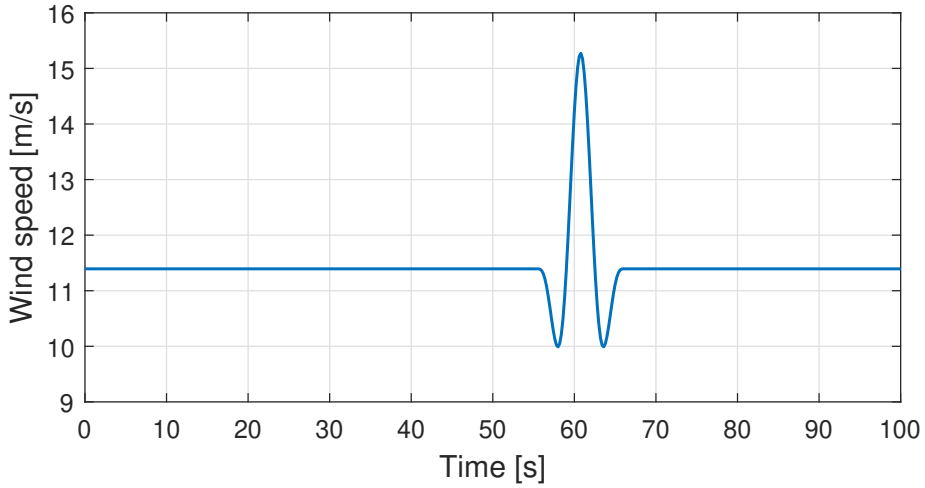

Figure 5.26: Wind gust EOG 1

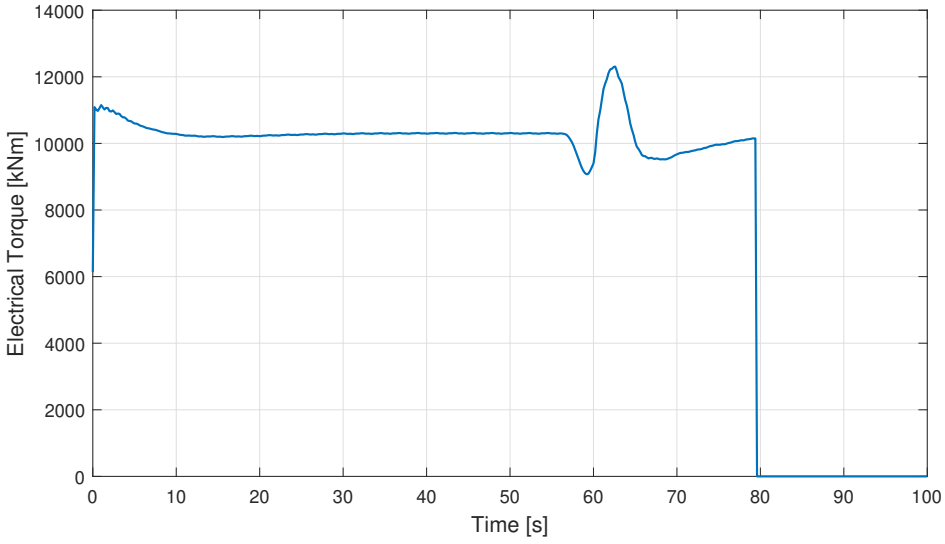

Figure 5.27: Electrical torque required with the visible grid fail

5.3.1 Global reference configuration

The reference configuration shows once again how powerful is the *free-form* method implemented. Indeed, even if considered as variable, the chord is not modified during the cycle, while the improved performances are produced by the change of the shape of airfoil FFA-W3-241. It is interesting to notice, that, due to the activation of the structural submodule, the aerodynamic optimization of the blade is different respect to the previous case. This is mainly caused by the relative high tolerance of the cycle. Indeed, the whole description of the blade generates some little differences in the numerical calculation, causing the cycle to stop in fewer iterations, which has the consequence of modifying less the airfoil shape, as it can be seen in Fig. 5.28. This explains, also, the smaller AEP found in this case and the lower efficiency of the profile, Fig. 5.29.

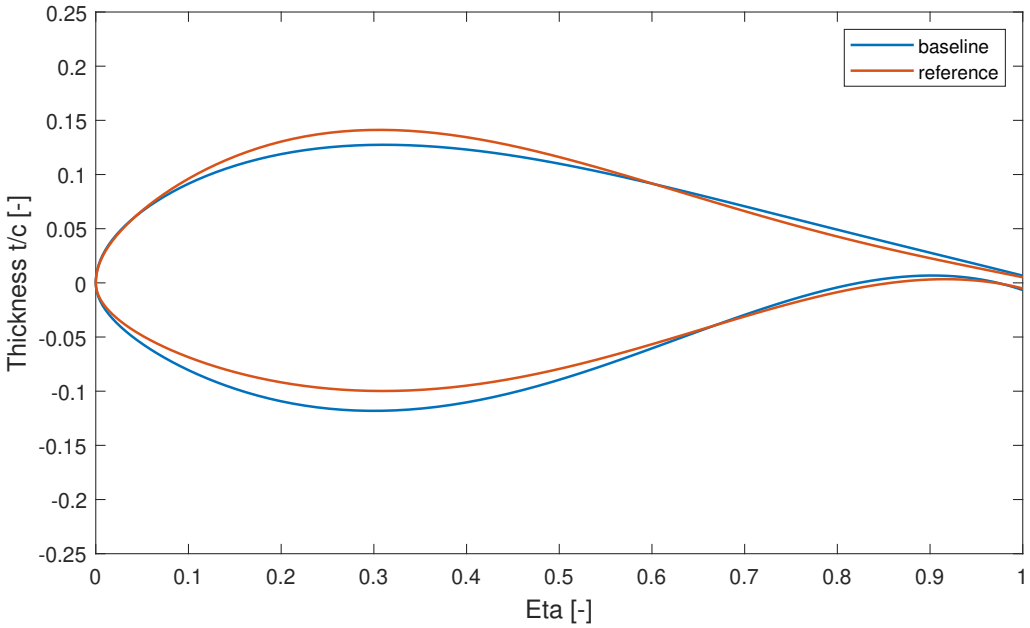

Figure 5.28: FFA-W3-241 airfoil shape optimization for the global reference case

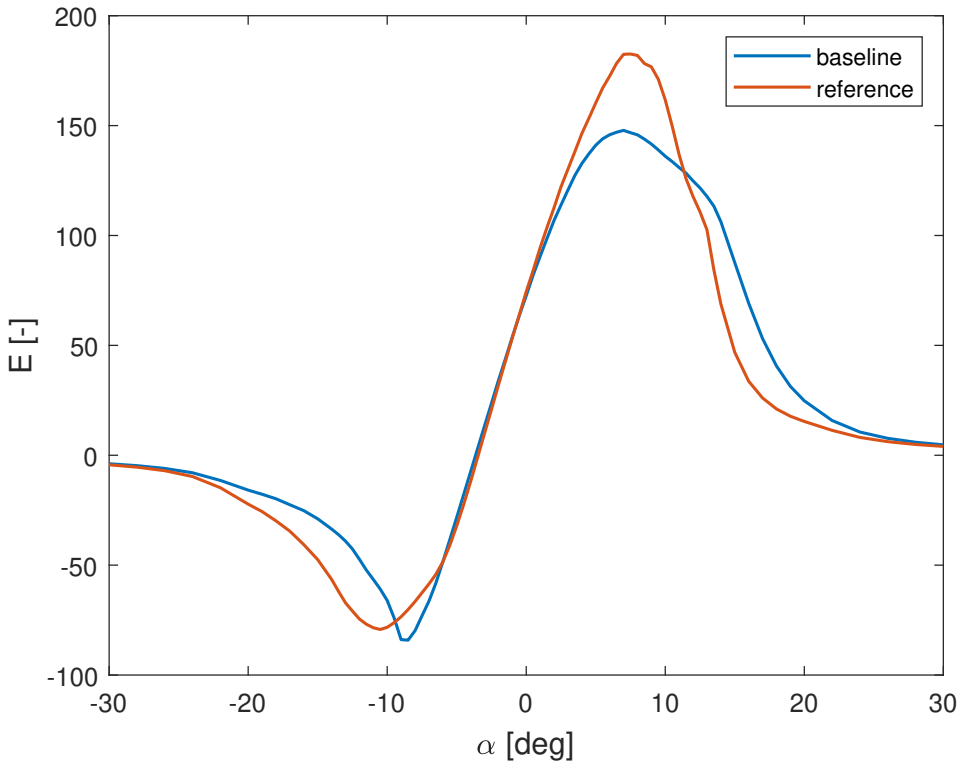

Figure 5.29: Airfoil efficiency comparison between baseline and global reference

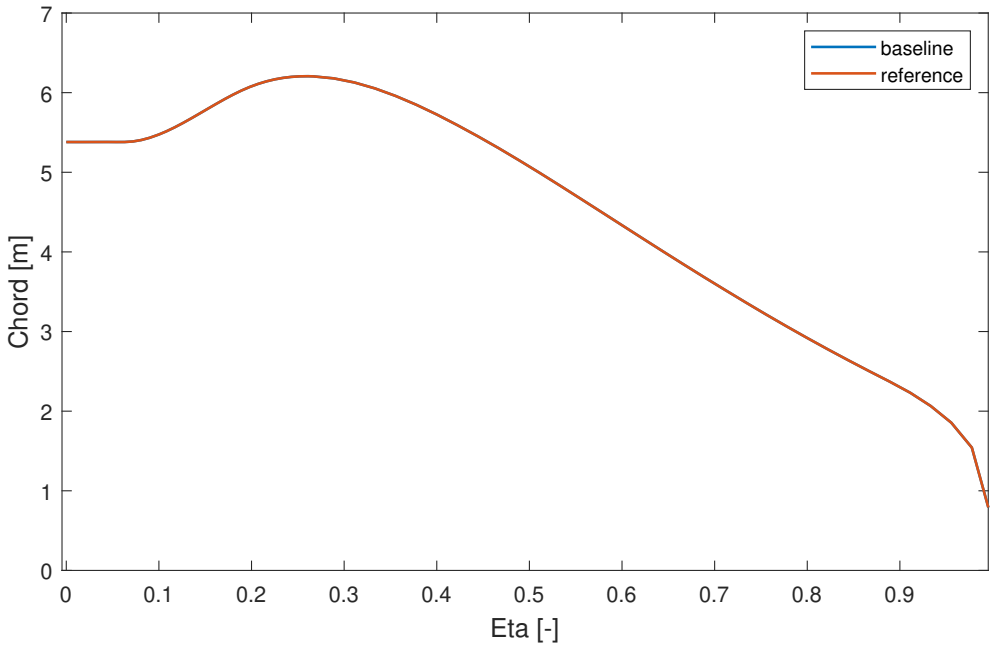

Figure 5.30: Chord distribution comparison between baseline and reference

	static AEP	**Cp***	**TSR***	**V**$_r$
final value	51575 MWh	0.4708	7.4841	11.2 m/s
variation from	185 MWh	0.0166	0.1896	-0.4 m/s
baseline	0.36 %	3.66 %	2.60 %	-3.45 %

Table 5.12: Aerodynamic parameters in the global reference case

Due to the increased aerodynamic performances, the blade is subjected at higher loads. For this reason, the thicknesses of the components are higher, especially near the tip, where the blade has been optimized. In particular, three different components are strongly changed: the leading edge reinforcement and the two spar caps. The first is not increased for structural reasons but because its distribution must now be the same of the trailing edge reinforcement. This probably adds useless additional mass and has the consequence of increasing the edgewise stiffness. Spar caps, instead, are thicker to be able to sustain the higher loads now experimented by the machines. In Tab. 5.14 and Fig. 5.33 is possible to see the new distributions of structural components. Then the CoE is computed, as it can be seen it is well reduced from the baseline value of 77.92 $/MWh, showing the goodness of the *free-form* method. At the end is possible to see the final noise emissions of the machine. As it can be seen from Tab. 5.15, they are higher than the ones found for the aerodynamic reference case, Tab. 5.8.

AEP	**Total mass**	**CoE**
44841 MWh	43633 kg	74.31 $/MWh

Table 5.13: Key performance indicator of the reference case

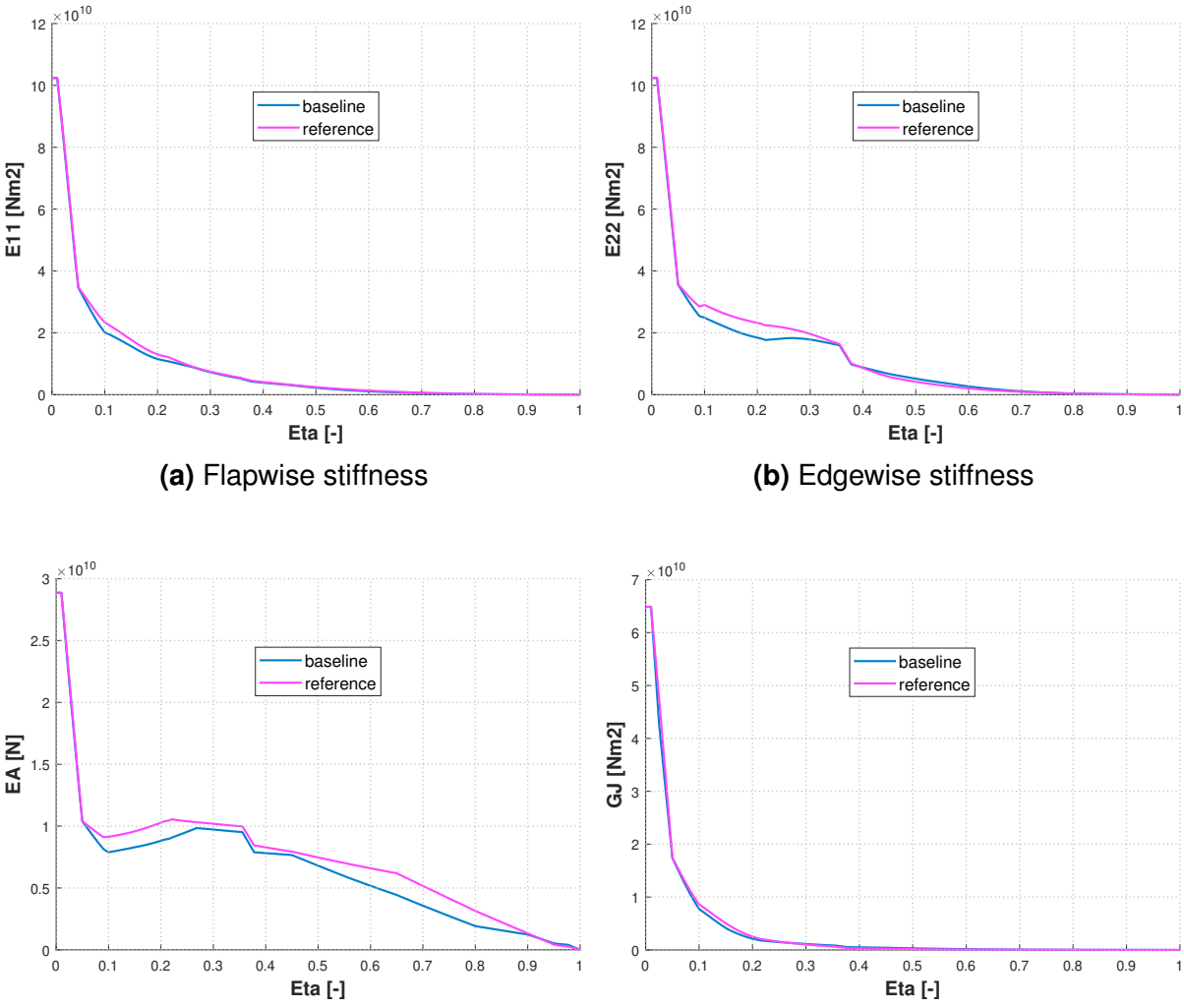

(a) Flapwise stiffness

(b) Edgewise stiffness

(c) Axial stiffness

(d) Torsional stiffness

Figure 5.31: Stiffness properties comparison between baseline and reference blade

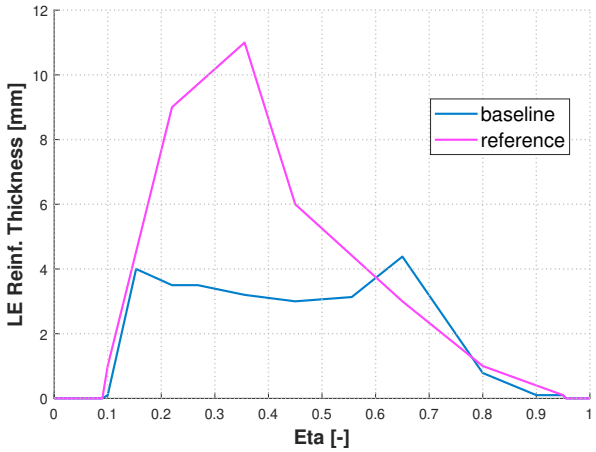

(a) Leading edge reinforcement

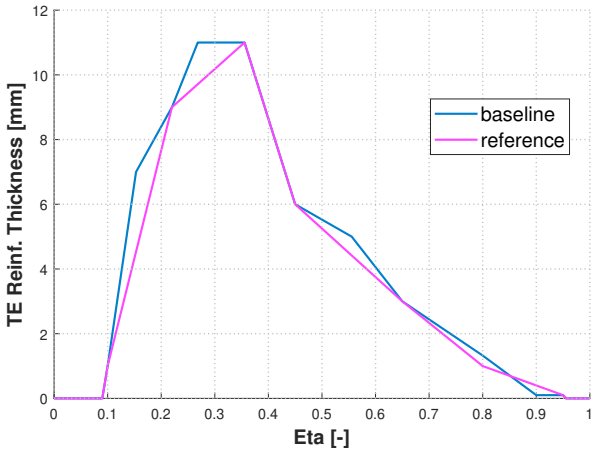

(b) Trailing edge reinforcement

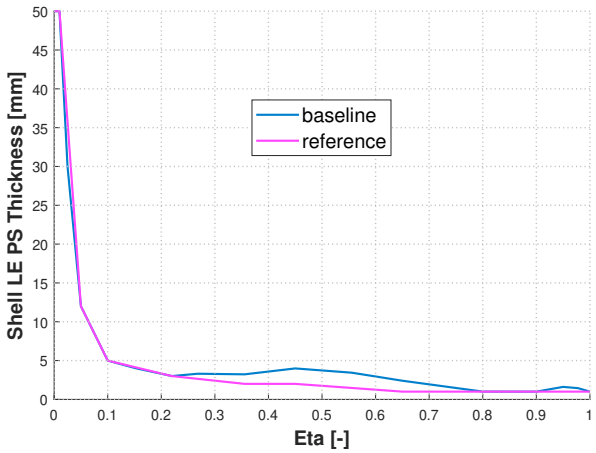

(c) Shell panels

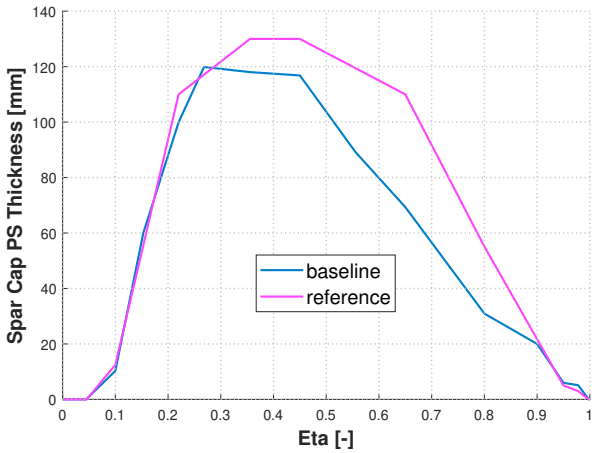

(d) Spar caps

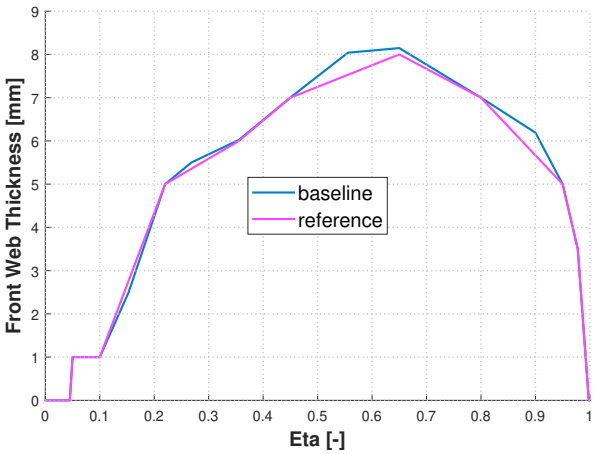

(e) Front and rear web

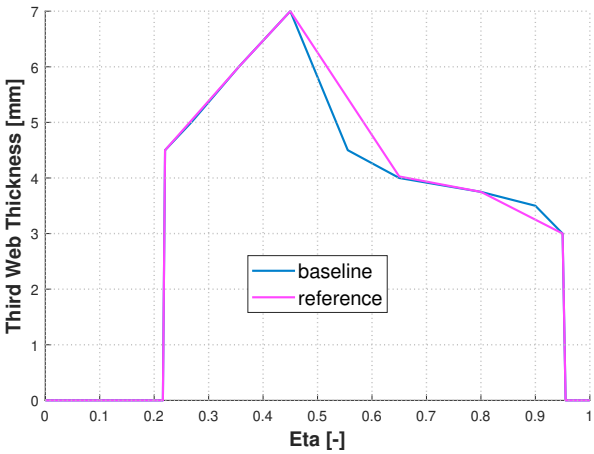

(f) Third web

Figure 5.32: Thickness distribution comparison between baseline and reference case

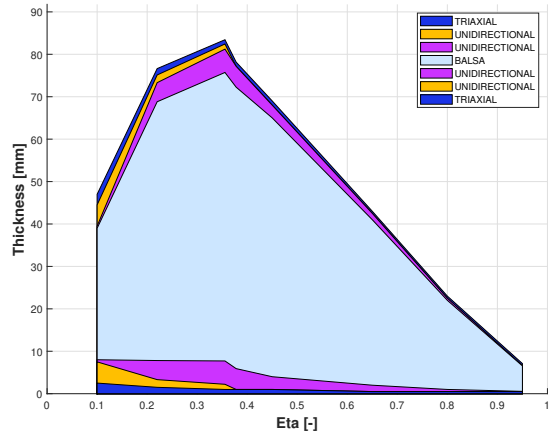

(a) Leading and trailing edge reinforcement

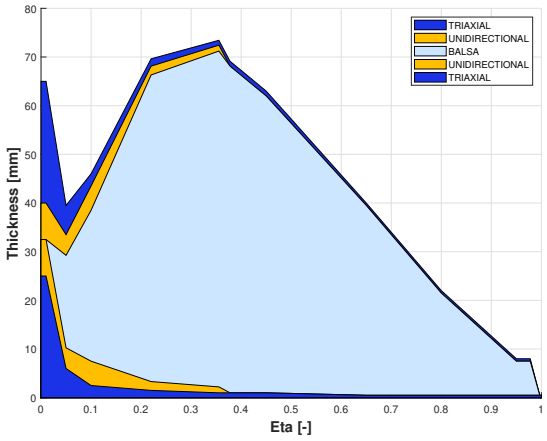

(b) Shell panels

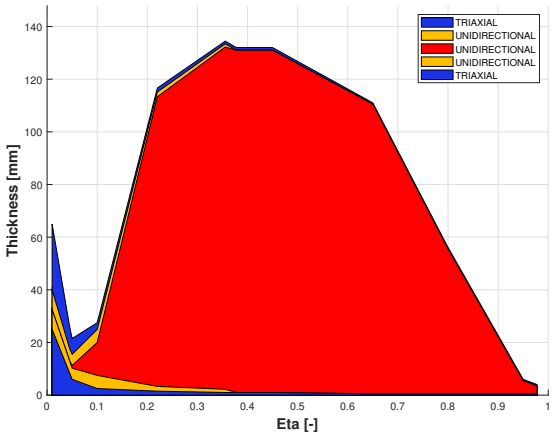

(c) Suction side spar cap

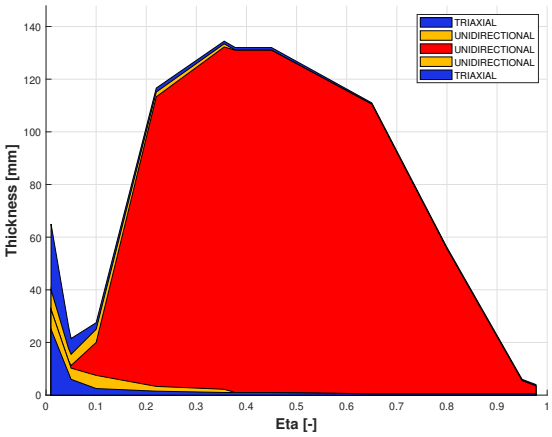

(d) Pressure side spar cap

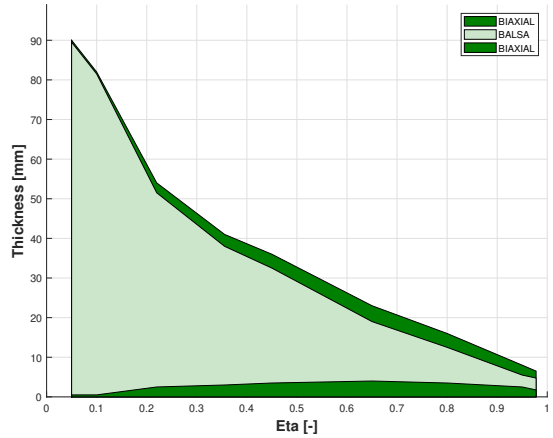

(e) Front and rear web

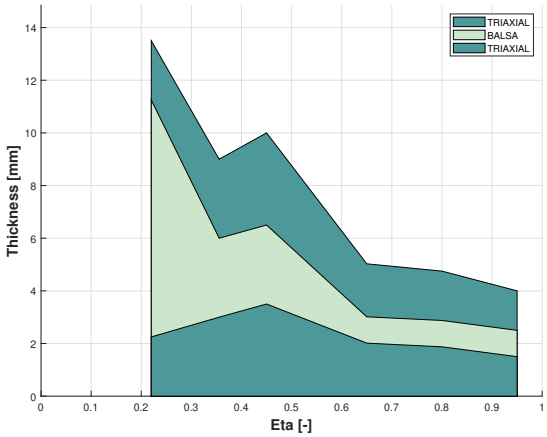

(f) Third web

Figure 5.33: Lamination sequence of the reference configuration

Section η	$t_{shell}^{TE,ss}$	$t_{shell}^{LE,ss}$	$t_{shell}^{TE,ps}$	$t_{shell}^{LE,ps}$	t_{rein}^{root}	t_{spar}^{ss}
0	50.00	50.00	50.00	50.00	15.00	-
0.010	50.00	50.00	50.00	50.00	15.00	-
0.050	12.00	12.00	12.00	12.00	8.50	1.00
0.100	5.00	5.00	5.00	5.00	10.00	12.49
0.220	3.00	3.00	3.00	3.00	3.63	110.00
0.356	2.00	2.00	2.00	2.00	2.43	130.00
0.450	2.00	2.00	2.00	2.00	-	130.00
0.650	1.00	1.00	1.00	1.00	-	110.00
0.800	1.00	1.00	1.00	1.00	-	55.10
0.950	1.00	1.00	1.00	1.00	-	5.00
0.978	1.00	1.00	1.00	1.00	-	3.00
Section η	t_{spar}^{ss}	t_{web}^{front}	t_{web}^{rear}	t_{web}^{third}	t_{rein}^{LE}	t_{rein}^{TE}
0	-	-	-	-	-	-
0.010	-	-	-	-	-	-
0.050	1.00	1.00	1.00	-	-	-
0.100	12.49	1.00	1.00	-	1.00	1.00
0.220	110.00	5.00	5.00	4.50	9.00	9.00
0.356	130.00	6.00	6.00	6.00	11.00	11.00
0.450	130.00	7.00	7.00	7.00	6.00	6.00
0.650	110.00	8.00	8.00	4.03	3.00	3.00
0.800	55.10	7.00	7.00	3.75	1.00	1.00
0.950	5.00	5.00	5.00	3.00	0.10	0.10
0.978	3.00	3.50	3.50	-	-	-

Table 5.14: Thicknesses [mm] of the structural components in reference configuration

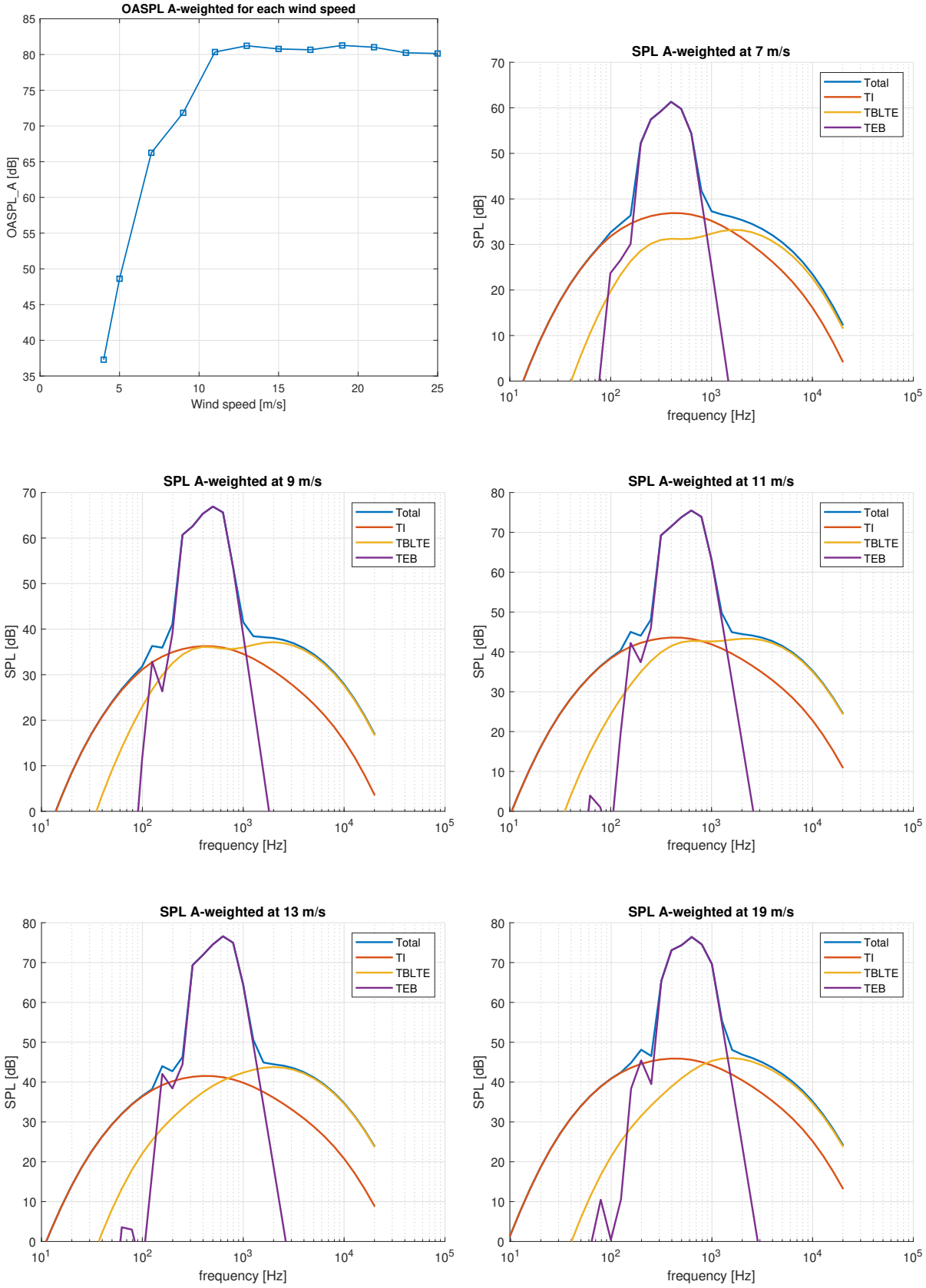

Figure 5.34: $OASPL_A$ values and noise spectra in the global reference case

Wind speed	7 m/s	9 m/s	11 m/s	13 m/s	19 m/s
$OASPL_A$ Total	66.25	71.85	80.36	81.23	81.26
$OASPL_A$ TI	47.08	46.45	53.78	51.73	56.11
$OASPL_A$ TBLTE	47.99	43.76	54.15	53.46	55.30
$OASPL_A$ TEB	66.17	71.82	80.34	81.22	81.24

Table 5.15: $OASPL_A$ [dB] in the global reference case

5.3.2 Global optimization with noise constraints

As said, an entire design cycle is computed, in order to notice the impact of the structural optimization on noise emissions and eventually on the quality of the architecture implemented. Noise limits are imposed as in the first case, by reducing of 1 dB the results found at the end of the reference case, Tab. 5.15. As it can be seen, the reference limits are higher than the values found in the aerodynamic reference case. Therefore, it is expected that the code is able to reduce noise emissions, but it is still important to check if the rise is due to the structural optimization or due to a less optimized blade. Furthermore, it must be checked the impact of the structural module on the difference between approximated and final results, in order to verify the accuracy of the architecture implemented.

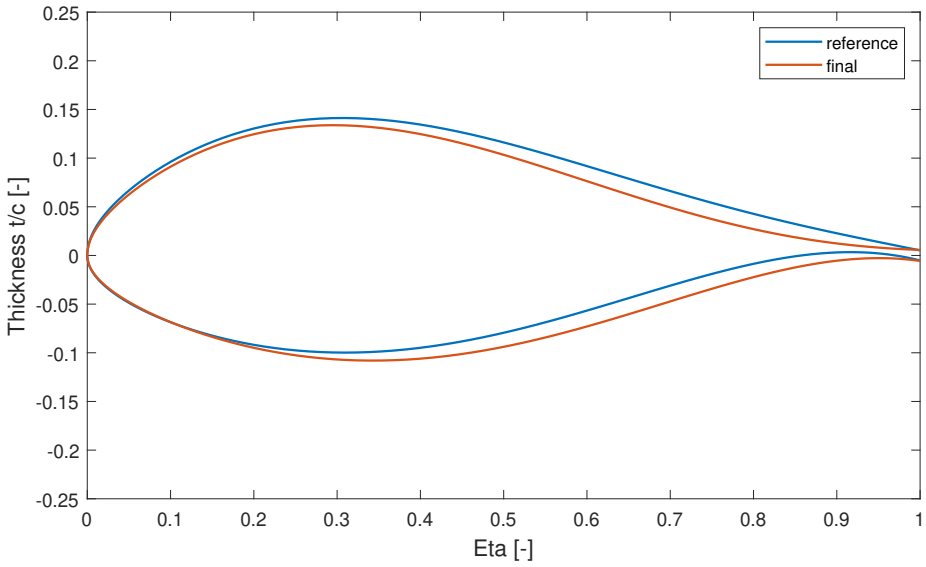

Figure 5.35: FFA-W3-241 airfoil shape modification considering the third test performed

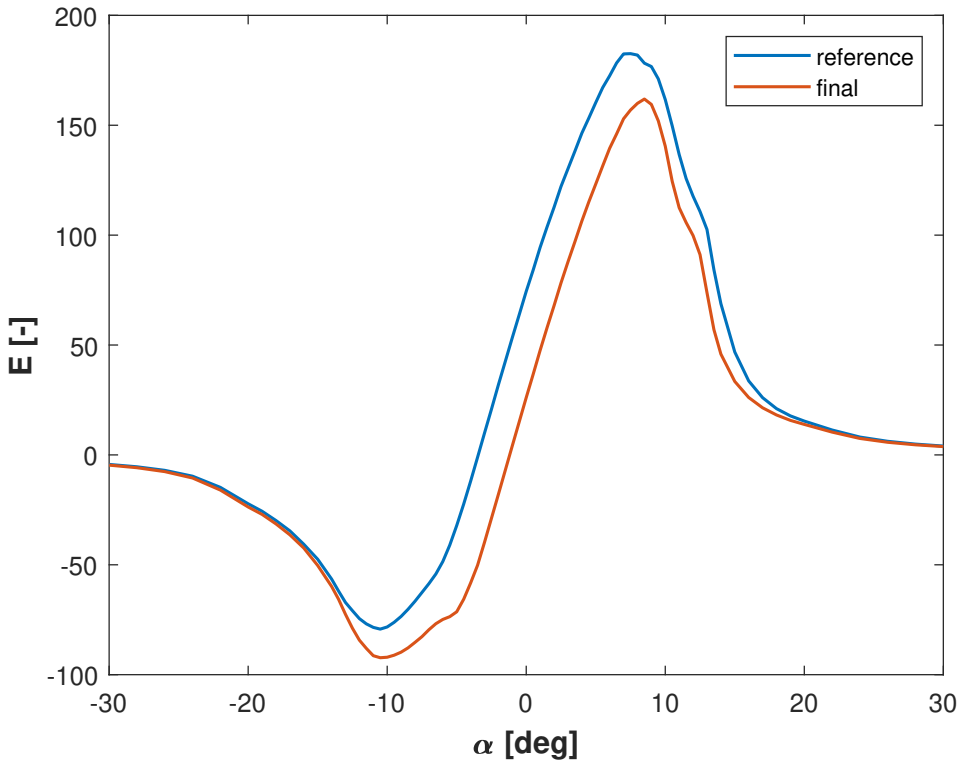

Figure 5.36: Airfoil efficiency considering the third test performed

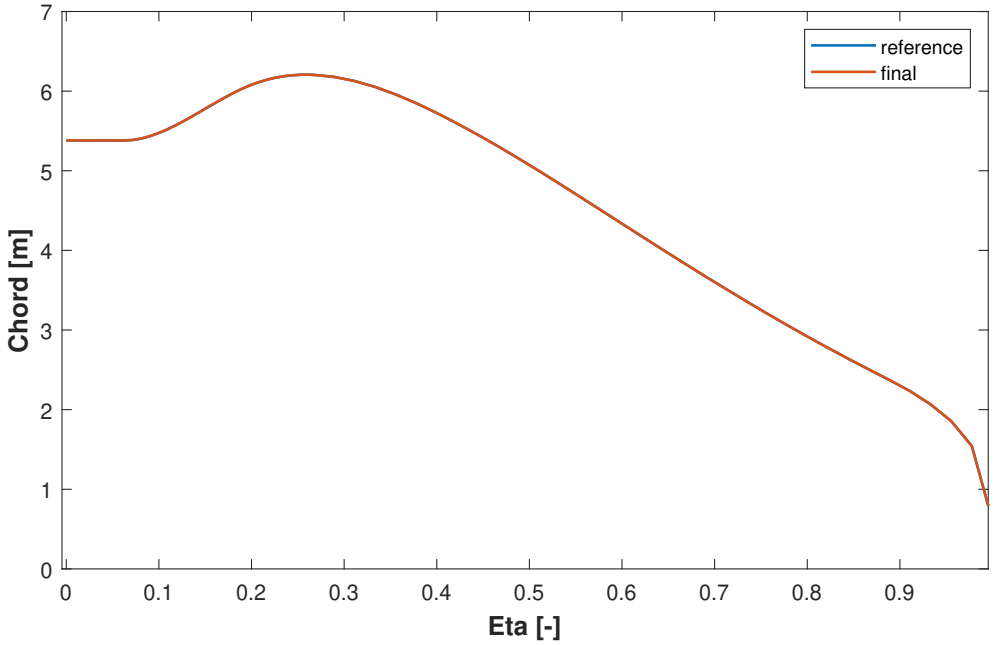

Figure 5.37: Chord distribution considering the third test performed

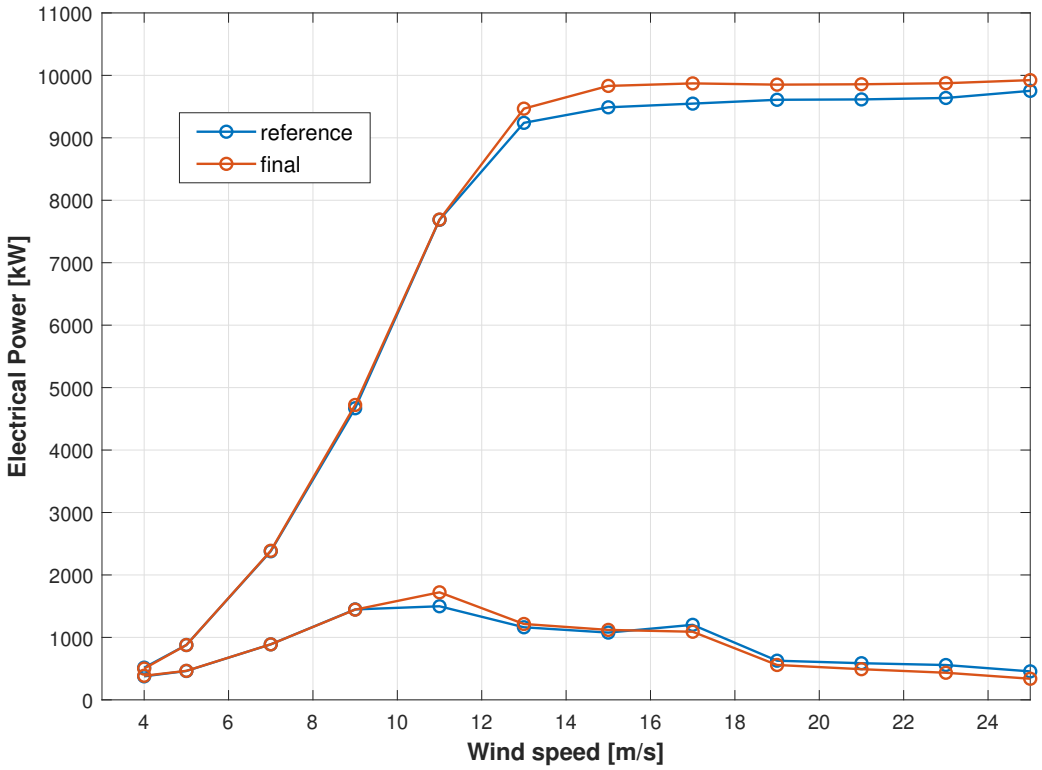

Figure 5.38: Comparison between reference and final turbulent power production and its standard deviation

	static AEP	**Cp***	**TSR***	**V**$_r$
final value	51688 MWh	0.4739	7.9468	10.6 m/s
variation from reference	113 MWh 0.22 %	0.0031 0.65 %	0.4626 6.18 %	-0.6 m/s -5.36 %

Table 5.16: Aerodynamic parameters considering the third test performed

It is interesting to notice that the final value of the AEP is higher than the reference case one. As said, this is due to the relative high tolerance of the aerodynamic cycle. Indeed, the addition of noise constraints has the effect to force the code to do more aerodynamic iterations, in order to satisfy all the limits imposed. This aspect is still significant because it shows once again how the reduction of noise has little impact on the aerodynamic performances of the turbine. It also proves that the initial shape not only is not optimally designed but, also, produces more noise than the optimized one. The profile found is closer to a symmetrical profile, which also explain why the efficiency of the profile is higher, form an absolute point of view, for negative angles of attack. Furthermore, the chord is left untouched also in this case, proving that the code is able to reduce emissions and maximize performances only by modifying the airfoil shape.

From a structural point of view, the two solutions have similar properties. As expected, due to the more aerodynamically performing blade, loads and thicknesses are slightly higher in this case respect to the reference one. It is possible to conclude similar considerations already done for the reference case in comparison with baseline. It is important to remark, instead, that the final CoE of the machine is lightly reduced, Tab. 5.17. An accurate structural analysis is out of the scope of the present work, however results are shown in details after the noise ones for completeness.

	AEP	**Blade mass**	**CoE**
final value	45769 MWh	44374 Kg	74.16 $/MWh
variation from reference	928 MWh 2.07 %	741 kg 1.70 %	-0.15 $/MWh -0.2 %

Table 5.17: Key performance indicators considering the third test performed

Much more important is to analyze the noise results. As it can be seen from Figs. 5.39 and 5.40 and Tab. 5.18, the simulation is performed successfully. Moreover, the trends are very similar to the ones previously found, Tab. 5.8, showing how the structure optimization has little influence on noise production. There is only one additional aspect to underline. The differences between approximated and final results are more similar than the first case. This can be explained by the higher stiffness of the blade respect to the baseline configuration, which mitigates the rise in rotational velocity, Figs. 5.41 and 5.42, by limiting the intensity of the vibrations of the wind turbine. It must be remarked that the approximated solution is computed with data retrieved from dynamic simulation run before entering the aerodynamic cycle, so with regulation trajectories and structural components identical to the baseline. This aspect proves that the architecture implemented is not only still valid, but it is more precise when structural module is included. Of course, conclusions must be verified

for different and more complete setups.

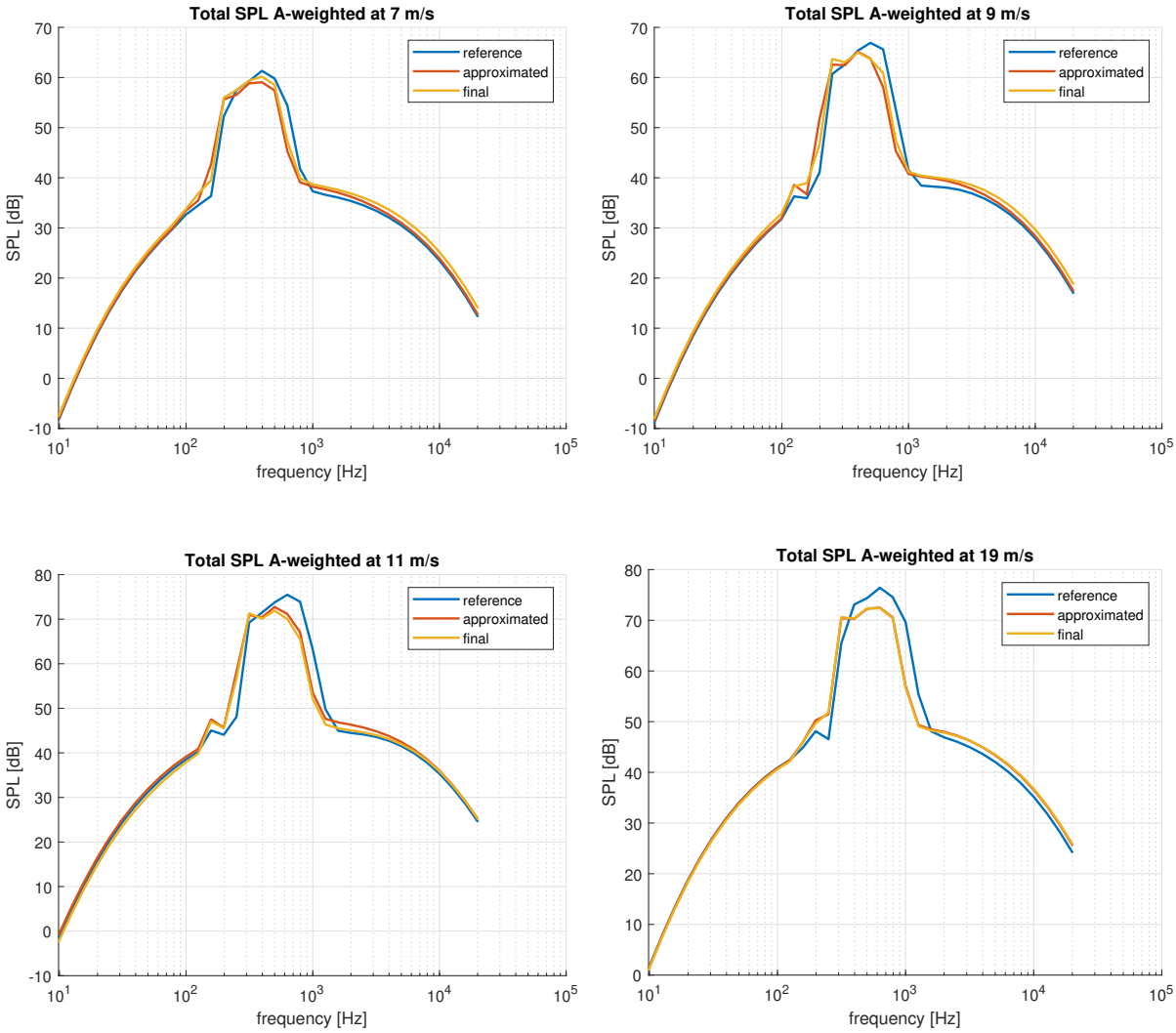

Figure 5.39: Total A-weighted noise spectra considering the third test performed

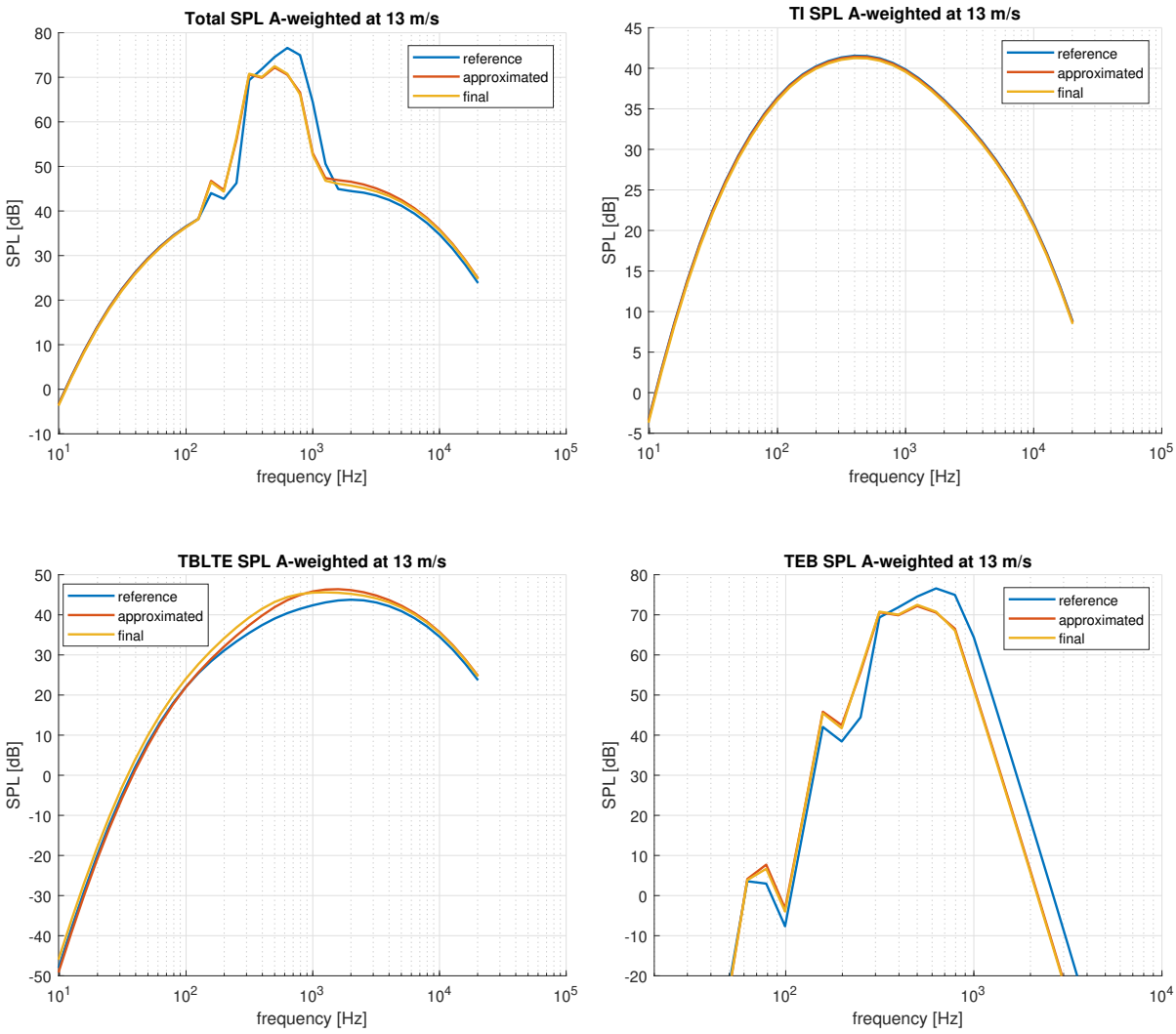

Figure 5.40: Total and specific noise spectra for 13 m/s considering the third test performed

Wind speed	**7 m/s**	**9 m/s**	**11 m/s**	**13 m/s**	**19 m/s**
OASPL $_A$ Total	65.68	70.52	77.31	77.56	78.39
Δ approximated	0.86	0.46	-0.58	0.16	0.01
Δ reference	-0.57	-1.32	-3.04	-3.67	-2.88
OASPL $_A$ TI	47.98	47.35	52.93	51.44	55.85
Δ approximated	0.70	0.58	-1.51	-0.18	-0.21
Δ reference	0.90	0.89	-0.85	-0.29	-0.26
OASPL $_A$ TBLTE	46.35	50.63	56.09	55.67	56.42
Δ approximated	1.06	1.13	0.20	-0.22	-0.08
Δ reference	2.59	2.64	1.94	2.21	1.13
OASPL $_A$ TEB	65.56	70.46	77.26	77.52	78.33
Δ approximated	0.8564	0.4485	-0.5782	0.1681	0.0134
Δ reference	-0.62	-1.36	-3.07	-3.70	-2.90

Table 5.18: OASPL $_A$ [dB] values and variations considering the third test performed

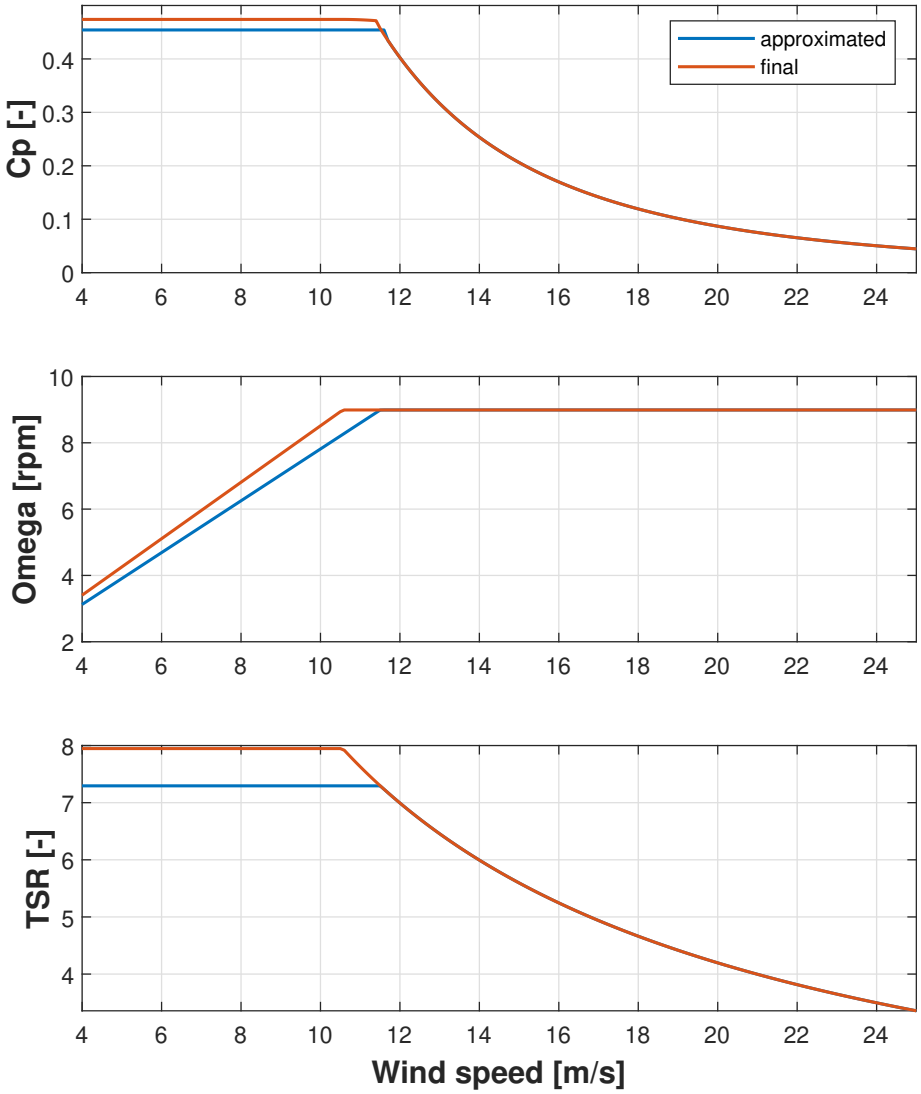

Figure 5.41: Trajectories comparison: approximated and final solution considering the third test performed

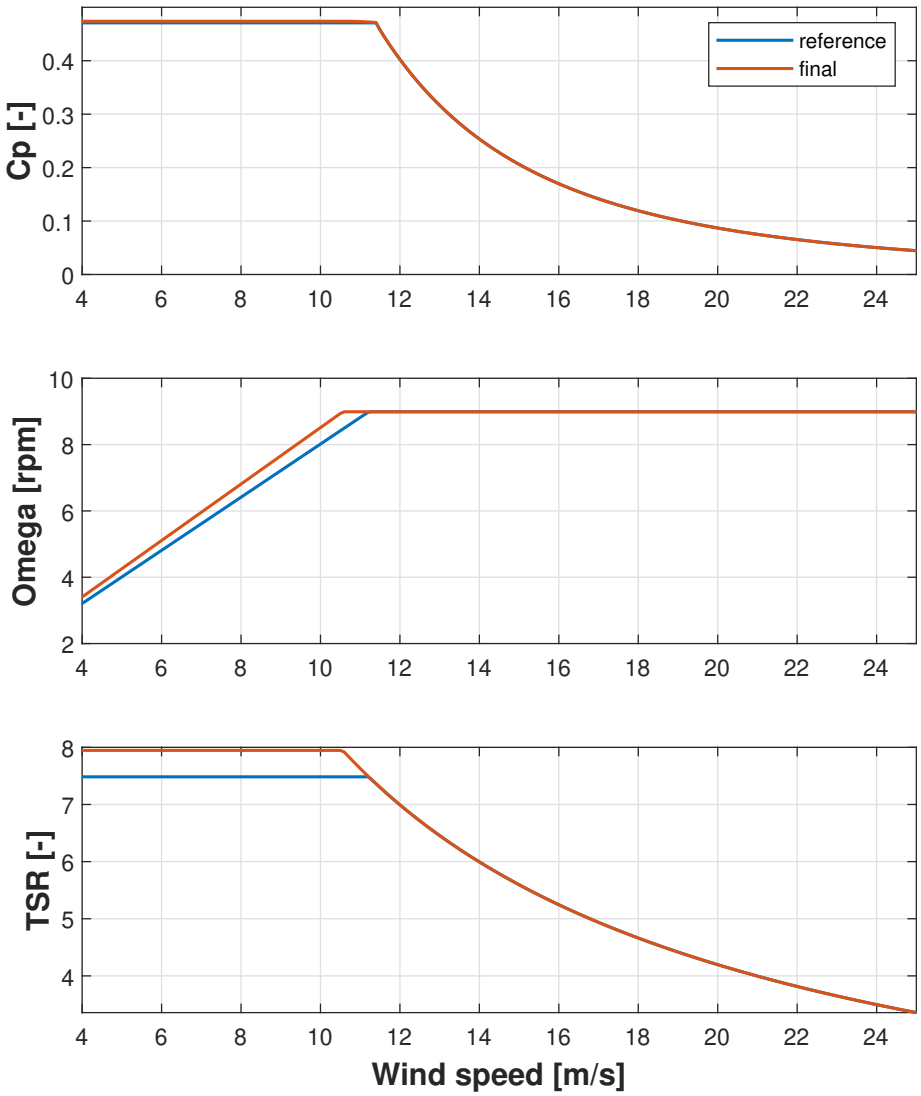

Figure 5.42: Trajectories comparison: reference and final solution considering the third test performed

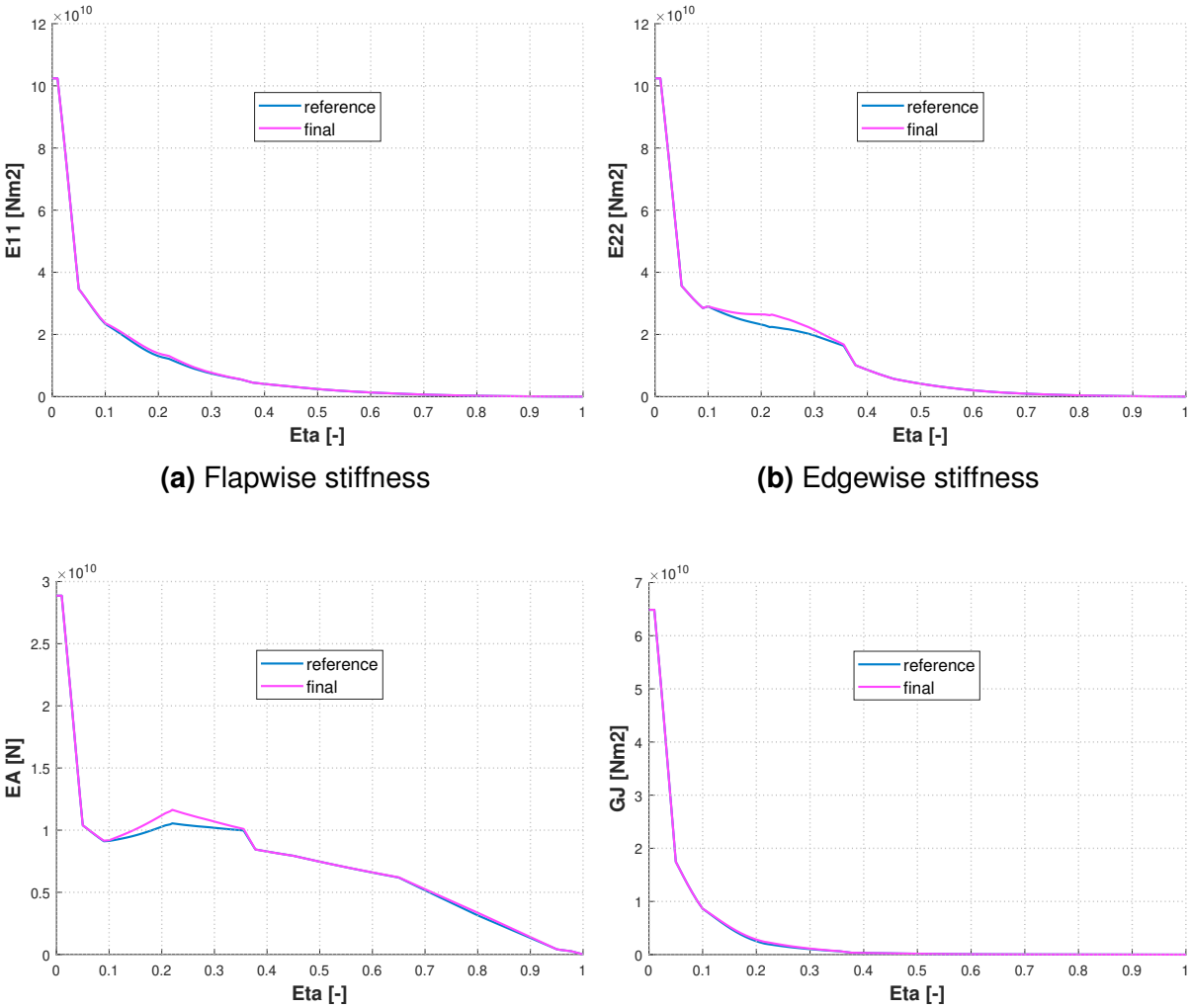

(a) Flapwise stiffness

(b) Edgewise stiffness

(c) Axial stiffness

(d) Torsional stiffness

Figure 5.43: Stiffness properties of the final blade

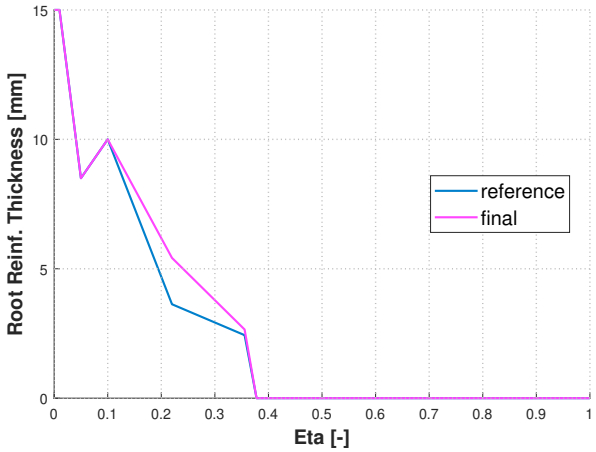

(a) Root reinforcement

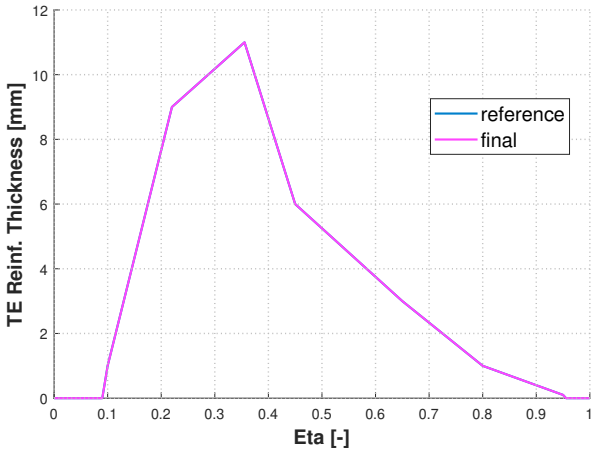

(b) Leading and trailing edge reinforcement

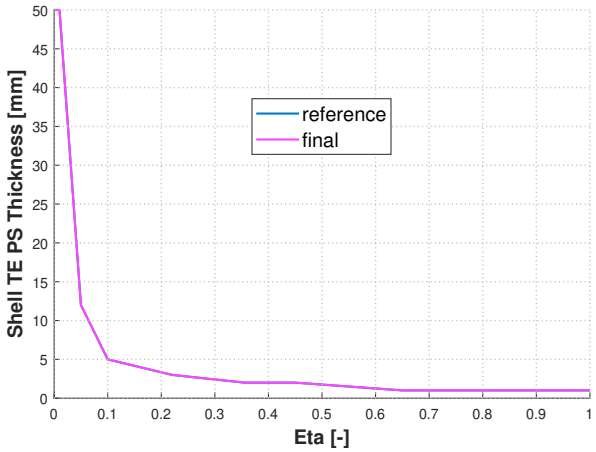

(c) Shell panels

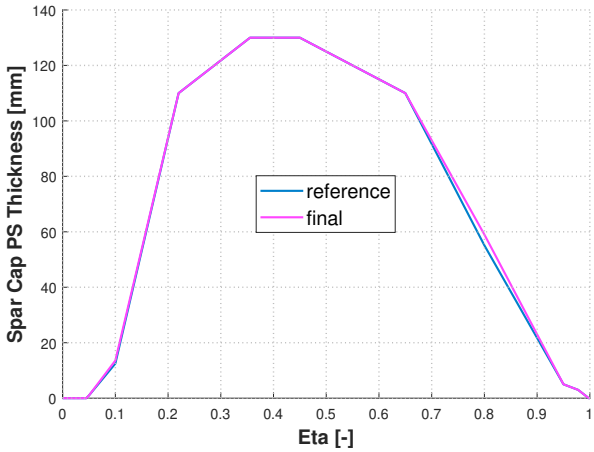

(d) Spar caps

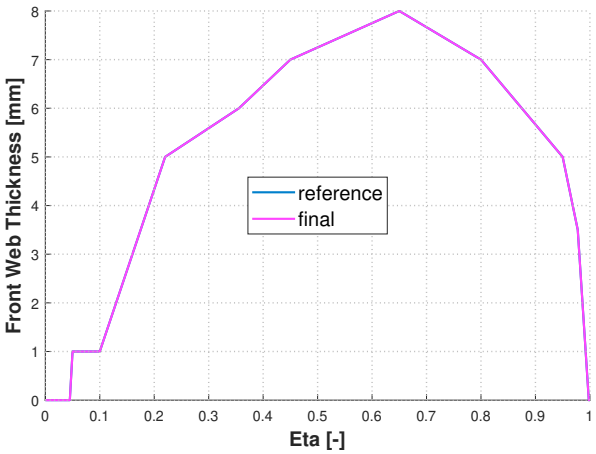

(e) Front and rear web

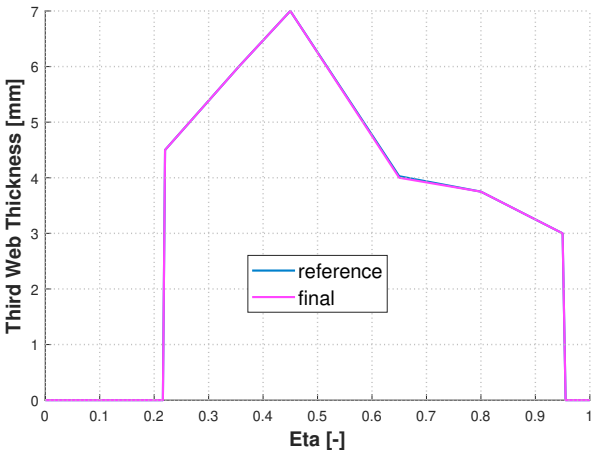

(f) Third web

Figure 5.44: Thickness distribution comparison between reference and final case

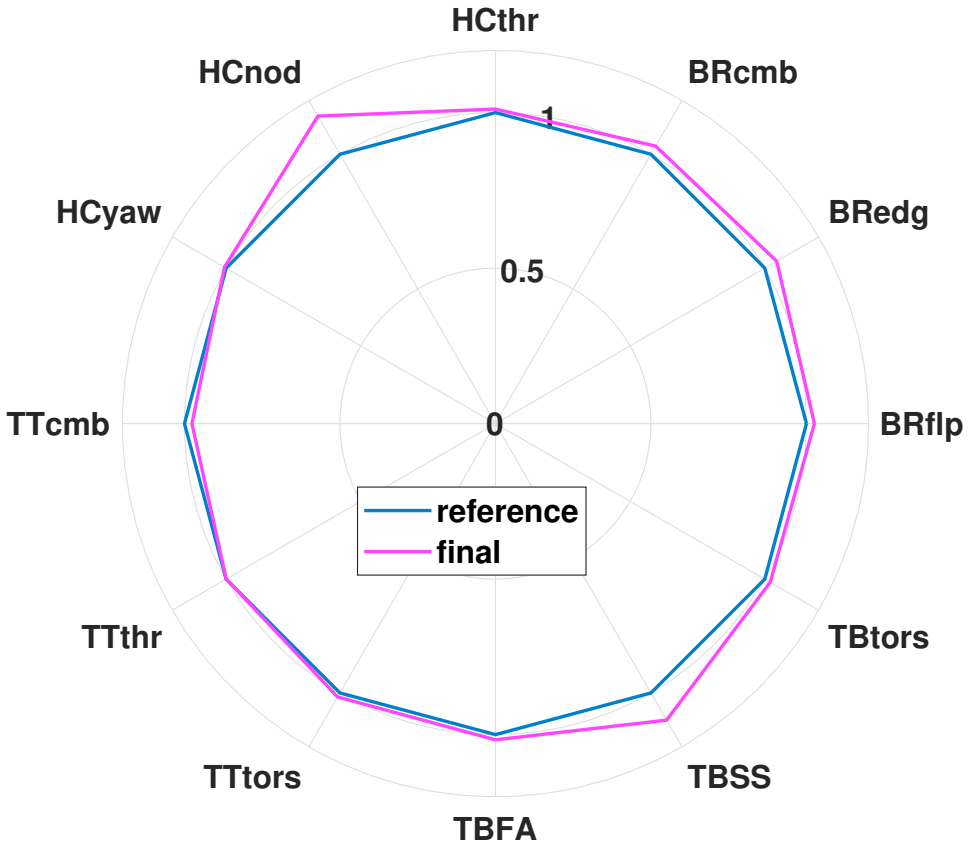

Figure 5.45: Summary of the ultimate loads variations

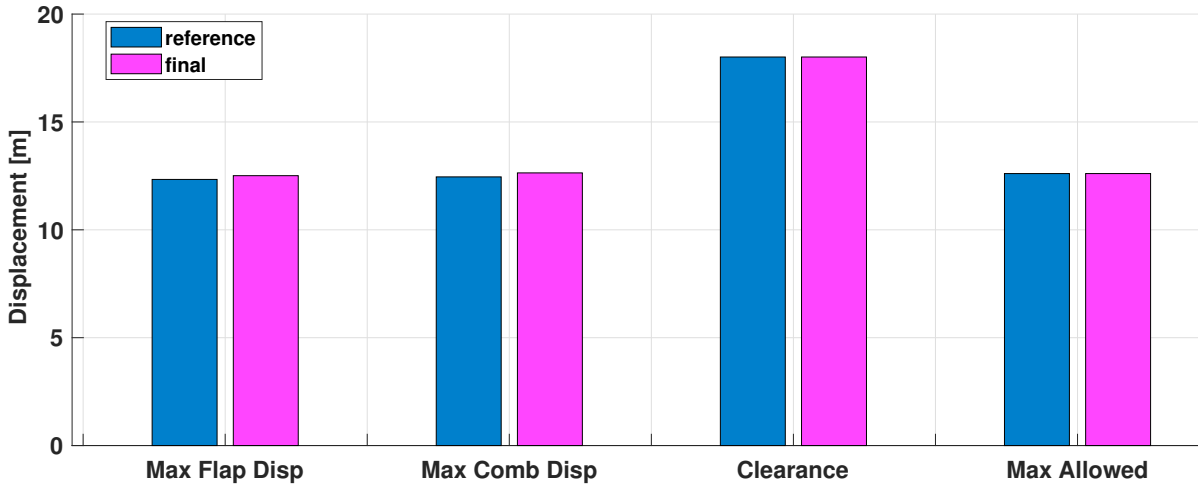

Figure 5.46: Maximum tip displacement in reference and final case

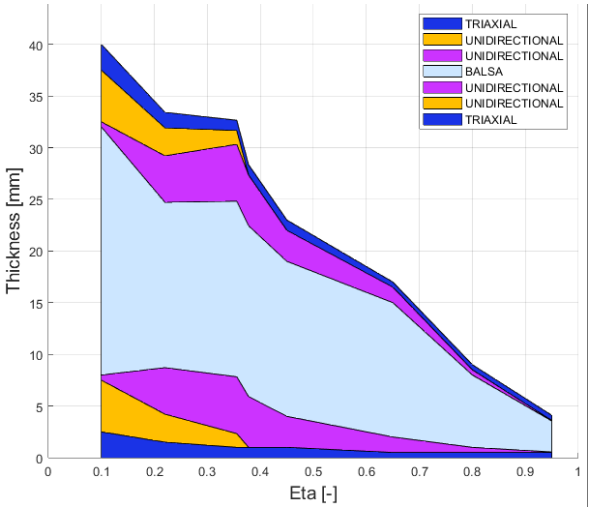

(a) Leading and trailing edge reinforcement

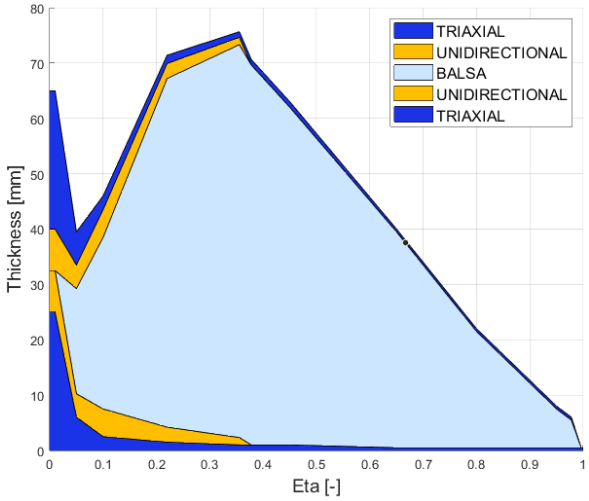

(b) Shell panels

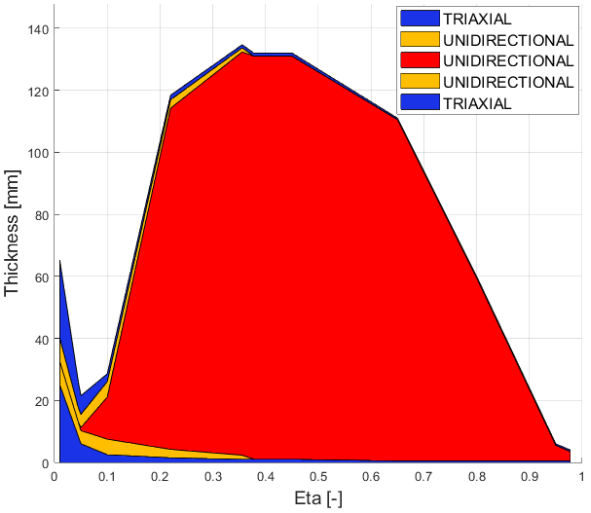

(c) Suction side spar cap

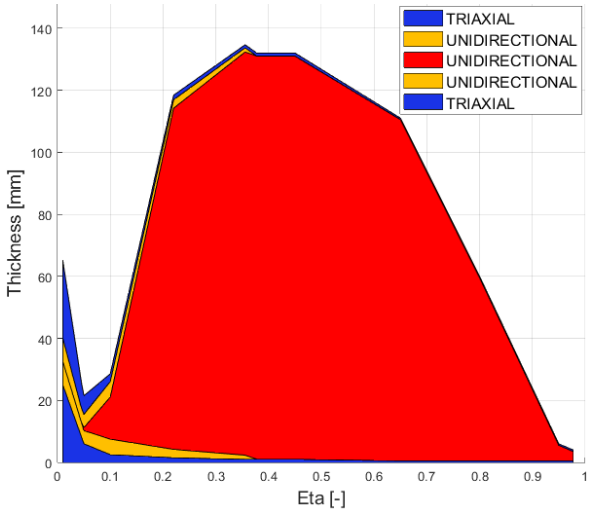

(d) Pressure side spar cap

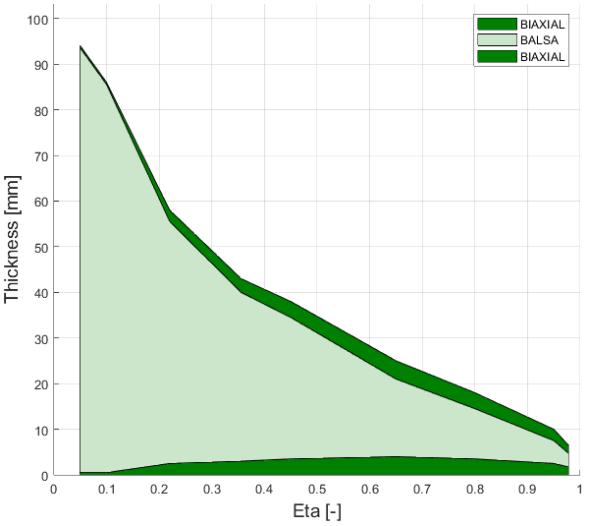

(e) Front and rear web

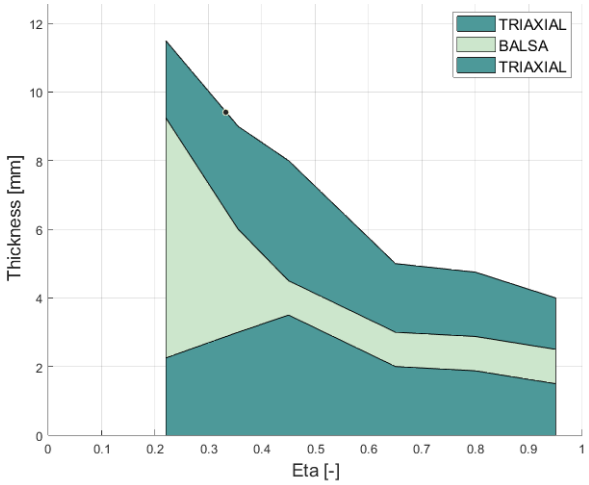

(f) Third web

Figure 5.47: Lamination sequence of the final configuration

Section η	$t_{shell}^{TE,ss}$	$t_{shell}^{LE,ss}$	$t_{shell}^{TE,ps}$	$t_{shell}^{LE,ps}$	t_{rein}^{root}	t_{spar}^{ss}
0	50.00	50.00	50.00	50.00	15.00	-
0.010	50.00	50.00	50.00	50.00	15.00	-
0.050	12.00	12.00	12.00	12.00	8.50	1.00
0.100	5.00	5.00	5.00	5.00	10.00	13.57
0.220	3.00	3.00	3.00	3.00	5.42	110.00
0.356	2.00	2.00	2.00	2.00	2.65	130.00
0.450	2.00	2.00	2.00	2.00	-	130.00
0.650	1.00	1.00	1.00	1.00	-	110.00
0.800	1.00	1.00	1.00	1.00	-	58.99
0.950	1.00	1.00	1.00	1.00	-	5.00
0.978	1.00	1.00	1.00	1.00	-	3.00
Section η	t_{spar}^{ss}	t_{web}^{front}	t_{web}^{rear}	t_{web}^{third}	t_{rein}^{LE}	t_{rein}^{TE}
0	-	-	-	-	-	-
0.010	-	-	-	-	-	-
0.050	1.00	1.00	1.00	-	-	-
0.100	13.57	1.00	1.00	-	1.00	1.00
0.220	110.00	5.00	5.00	4.50	9.00	9.00
0.356	130.00	6.00	6.00	6.00	11.00	11.00
0.450	130.00	7.00	7.00	7.00	6.00	6.00
0.650	110.00	8.00	8.00	4.00	3.00	3.00
0.800	58.99	7.00	7.00	3.75	1.00	1.00
0.950	5.00	5.00	5.00	3.00	0.10	0.10
0.978	3.00	3.50	3.50	-	-	-

Table 5.19: Thicknesses [mm] of the structural components in final configuration

Chapter 6

Conclusions

As it has been shown, it is possible to include a predictive aeroacustic analysis inside the aerodynamic design cycle to limit noise produced by a wind turbine. The efficacy of the method depends on the main source contribution. Indeed, while trailing edge bluntness and turbulent boundary - layer noise can be reduced and controlled by changing the shape of the profiles near the tip of the blade, the turbulent inflow contribution is not controllable with the implemented architecture. This source is not directly influenced by the modification of the airfoil shape. However, blade geometry affects the regulation trajectories and the structural definition of the rotor, which have a strong impact on the turbine behavior during dynamic simulations, and they eventually influence turbulent inflow noise. Moreover, it must be remarked that the turbine under analysis is of class 1A, which represents the worst case of turbulence intensity, therefore, also, of turbulent inflow noise production. Still, with the new update recently received, this contribution is the least relevant, so it should be possible to reduce noise emissions by control the other sources. Nevertheless, the improved formulation of turbulent inflow noise needs to be better investigated, so further analyses and tests should be performed to fully understand the new behavior of the source.

Another aspect to underline is the flexibility of the *free-form* method that, not only is able to reduce the emissions, but it is also able to optimize the blade geometry with the new constraint, in order to maximize the AEP, which remains at least comparable to the one obtained without the constraint. This aspect shows the goodness of the idea of the work. However, it must be remarked that preliminary simulations with few active variables and high tolerances have been performed. Still the new architecture

implemented has proved to be a good compromise between the computational time required and the accuracy of the results, even if the latter are not validated from a quantitative point of view.

6.1 Future developments

Possible future developments of the method can be based on two different approaches. First, studies can be conducted in order to improve the semi-empirical models used in the tool to compute noise emissions. Particularly, experiments should be performed to developed a new turbulent inflow model, which accounts for the shape of the airfoils. Tests should, also, be realized on airfoils with comparable size to the one used in the work. This aspect is key, in order to improve the accuracy of the results, in particular for the trailing edge bluntness noise contribution. The scope of the implementation is to limit noise emission to satisfy legal norms. Therefore, in order to use the code for real applications, it is important to certify that the values found by the models are comparable to real emissions.

The second approach, instead, concerns the development of *Cp-Max* architecture. As well documented in literature, the rotational speed is a very important parameter to strongly reduce noise emissions. Even nowadays, the value imposed on the maximum tip velocity is not automatically found by the algorithm, but it is imposed after some simulations. A new cycle, which has as only variable the tip speed, could be introduced at the beginning of the aerodynamic module. It should include the whole noise analysis tool, so also the dynamic simulations performed with *Cp-Lambda*, in order to evaluate correctly all the contributions and automatically find the higher tip velocity for which noise emissions are lower than the imposed ones. This process would help find the most performing configuration when noise emissions could not be lowered only by acting on the airfoil shape.

Dynamic *Cp-Lambda* simulations could be taken inside the aerodynamic optimization to have even more accurate results. This is possible only if the computational time is reduced, for example by acting on the number of finite elements describing the blade, or on the converging tolerance. Otherwise, a new lighter software should

be found, similar to the introduction of *WTPerf* instead of *Cp-Lambda* for the computation of the aerodynamic performances of the rotor when the *free-form* method is used. This is particularly important in case more complex simulations reveal too much discrepancy between approximated results and final ones.

Lastly, more tests of the introduced implementation should be performed. Indeed, the positive results of the present work open the road to a new unexplored space of the design process. Multiple parameters can be changed to inspect the possibilities granted by the implementation, and to find the corresponding limits. The simulations have been computed on a typical laptop, whereas the use of more powerful computers has to be considered for more complete simulations. Indeed, the twist distribution can also be included and a simulation of multiple complete design cycles can be performed. Moreover, the tool can be tested on a different machine, where noise sources have a different relevance. Also, it is important to understand if it is possible to reduce at the same time both turbulent boundary layer - trailing edge and trailing edge bluntness noise. Another important aspect to investigate is when it is convenient to activate the noise limit constraint. For example, in the present work, the starting configuration has always been the same, whereas it would be interesting to notice what happens if the constrained optimization starts from the configuration found using the *free-form* method without limiting noise emissions.

Bibliography

[1] Technical report of WindEurope, *Wind energy in Europe 2020 Statistics and the outlook for 2021-2025*, February 2021

[2] Technical report of Iec-61400-11, *Wind turbine generator systems – part 11: Acoustic noise measurement techniques*, edition 2, 2002

[3] G. Bolzoni, *Integration of airfoil design within a system-level optimization framework*, Master thesis at Politecnico di Milano, 2019

[4] C. R. Sucameli, *Development and implementation of an aeroacoustic module for wind turbine noise prediction*, Master thesis at Politecnico di Milano, 2017

[5] R. K. Amiet, *Acoustic radiation from an airfoil in a turbulent stream*, Journal of Sound and Vibration, Volume 41, Issue 4, p. 407-420, 1975

[6] R. W. Paterson and R. K. Amiet, *Acoustic radiation and surface pressure characteristics of an airfoil due to incident turbulence*, 3rd AIAA Aero-Acoustics Conference, Palo Alto CA, 1976

[7] P. Fuglsang et al., *Site-specific Design Optimization of Wind Turbines*, Wind Energy 5.4, pp. 261–279, 2002

[8] K. Maki, R. Sbragio, and N. Vlahopoulos, *System design of a wind turbine using a multi-level optimization approach*, Renewable Energy 43, pp. 101–110, 2012

[9] J. Zhu, X. Cai, and R. Gu, *Aerodynamic and Structural Integrated Optimization Design of Horizontal-Axis Wind Turbine Blades*, Energies 9.2, 2016

[10] F. Grasso, *Design of a family of new advanced airfoils for low wind class turbines*, Journal of Physics: Conference Series 555, 2014

[11] T. Zhang et al., *A study of airfoil parameterization, modeling, and optimization based on the computational fluid dynamics method*, Journal of Zhejiang University-SCIENCE A 17.8, pp. 632–645, 2016

[12] T. H. Hansen, *Airfoil optimization for wind turbine application*, Wind Energy 21.7, pp. 502–514, 2018

[13] L. Sartori et al., *Integration of airfoil design during the design of new blades*, ICOWES2013, International Conference on Aerodynamics of Offshore Wind Energy Systems and Wakes, 2013

[14] C. L. Bottasso et al., *Free-form design of rotor blades*, Journal of Physics: Conference Series, June 2014

[15] M. J. Lighthill, *On sound generated aerodynamically. I. General theory*, The Royal Society, vol. 211, pp. 564–587, 1952

[16] N. Curle, *The influence of solid boundaries upon aerodynamic sound*, The Royal Society, vol. 231, pp. 505–514, 1955

[17] J. F. Williams and D. L. Hawkings, *Sound generation by turbulence and surfaces in arbitrary motion*, Philosophical Transactions of the Royal Society of London A: Mathematical, Physical and Engineering Sciences, vol. 264, no. 1151, pp. 321–342, 1969

[18] J. F. Williams and L. Hall, *Aerodynamic sound generation by turbulent flow in the vicinity of a scattering half plane*, Journal of Fluid Mechanics, vol. 40, no. 4, pp. 657–670, 1970

[19] K. S. Brentner and F. Farassat, *Modeling aerodynamically generated sound of helicopter rotors*, Progress in Aerospace Sciences, vol. 39, no. 2, pp. 83–120, 2003

[20] F. Farassat, *Theory of noise generation from moving bodies with an application to helicopter rotors*, National Aeronautics and Space Administration, 1975

[21] K. S. Brentner, *Prediction of helicopter rotor discrete frequency noise: a computer program incorporating realistic blade motions and advanced acoustic formulation*, 1986

[22] K. S. Brentner, L. Lopes, H.-N. Chen, and J. F. Horn, *Near real-time simulation of rotorcraft acoustics and flight dynamics*, Journal of aircraft, vol. 42, no. 2, pp. 347–355, 2005

[23] S. Oerlemans, P. Sijtsma, and B. M. Lopez, *Location and quantification of noise sources on a wind turbine*, Journal of Sound and Vibration, vol. 299, no. 4–5, pp. 869 – 883, 2007

[24] C. Arakawa, O. Fleig, M. Iida, and M. Shimooka, *Numerical approach for noise reduction of wind turbine blade tip with earth simulator*, Journal of the Earth Simulator, vol. 2, no. 3, pp. 11–33, 2005

[25] F. W. Grosveld, *Prediction of broadband noise from horizontal axis wind turbines*, Journal of Propulsion and Power, ISSN 0748-4658, vol. 1, pp. 292–299, 1985

[26] S. Glegg, S. Baxter, and A. Glendinning, *The prediction of broadband noise from wind turbines*, Journal of sound and vibration, vol. 118, no. 2, pp. 217– 239, 1987

[27] A. S. H. Lau, J. W. Kim, J. Hurault, and T. Vronsky, *A study on the prediction of aerofoil trailing-edge noise for wind-turbine applications*, Wind Energy, vol. 20, no. 2, pp. 233–252, 2017

[28] M. Kamruzzaman, T. Lutz, A. Herrig, and E. Kraemer, *Rans based prediction of airfoil trailing edge far-field noise: Impact of isotropic and anisotropic turbulence*, No. 2008-2867, 2008

[29] P. Fuglsang and H. Aagaard Madsen, *Implementation and verification of an aeroacoustic noise prediction model for wind turbines*, 1996

[30] J. Schepers, A. Curvers, S. Oerlemans, K. Braun, T. Lutz, A. Herrig, W. Wuerz, A. Mantesanz, L. Garcillan, M. Fischer, et al., *Sirocco: silent rotors by acoustic optimisation*, vol. 2021, 2007

[31] G. Guidati, R. Bareiss, S. Wagner, T. Dassen, and R. Parchen, *Simulation and measurement of inflow-turbulence noise on airfoils*, American Institute of Aeronautics and Astronautics Paper, pp. 97–1698, 1997

[32] P. Moriarty, G. Guidati, and P. Migliore, *Prediction of turbulent inflow and trailing-edge noise for wind turbines*, AIAA Paper of the 11th AIAA/CEAS Aeroacoustics Conference, Monterey, CA, 2005

[33] M.V.Lowson, *Assessment and prediction of wind turbine noise*, Flow Solutions Report 92/19, 1993

[34] P. Moriarty and P. Migliore, *Semi-empirical aeroacoustic noise prediction code for wind turbines*, technical report, National Renewable Energy Lab, Golden, CO, US, 2003

[35] W. J. Zhu, N. Heilskov, W. Z. Shen, and J. N. Sørensen, *Modeling of aerodynamically generated noise from wind turbines*, Journal of Solar Energy Engineering, vol. 127, no. 4, pp. 517–528, 2005

[36] K. Boorsma and J. Schepers, *Enhanced wind turbine noise prediction tool silant*, technical report ECN-M-12-004, 2011

[37] W. K. Blake, *Mechanics of Flow-Induced Sound and Vibration, Volume 1: General Concepts and Elementary Sources*, Academic press, 2017

[38] R. Parchen, *Progress report draw : a prediction scheme for trailing edge noise based on detailed boundary layer characteristics*, 1998

[39] M. S. Howe, *A review of the theory of trailing edge noise*, Journal of Sound and Vibration, 1978

[40] F. Bertagnolio, *Trailing edge noise model applied to wind turbine airfoils*, technical report, Danmarks Tekniske Universitet, Risø Nationallaboratoriet for Bæredygtig Energi, 2008

[41] F. Bertagnolio, H. Aagaard Madsen, and C. Bak, *Experimental validation of TNO trailing edge noise model and application to airfoil optimization*, 2009 European Wind Energy Conference and Exhibition, 2009

[42] K. G. Hermann Schlichting, *Boundary-Layer Theory*, Springer Verlag Berlin Heidelberg, ninth edition, 2017

[43] F. Bertagnolio, A. Fischer, and W. Zhu, *Tuning of turbulent boundary layer anisotropy for improved surface pressure and trailing-edge noise modeling*, Journal of Sound and Vibration, vol. 333, no. 3, pp. 991–1010, 2014

[44] T. F. Brooks, D. S. Pope, and M. A. Marcolini, *Airfoil self-noise and prediction*, NASA Reference Publication 1218, 1989

[45] T. F. Brooks and T. H. Hodgson, *Trailing edge noise prediction from measured surface pressures*, Journal of Sound and Vibration, 1981

[46] P. K. Chaviaropoulos et al., *INNWIND Deliverable 1.2.3 PI-based assessment of innovative concepts (methodology)*, technical report INNWIND.EU, 2014

[47] C. L. Bottasso and A. Croce, *Cp-Lambda a Code for Performance, Loads, Aeroelasticity by Multi-Body Dynamics Analyis*, technical report Politecnico di Milano, 2010-2018

[48] C. L. Bottasso et al, *Aeroservo-elastic modeling and control of wind turbines using finite-element multibody procedures*, pp. 291–308, 2006

[49] F. Gualdoni, *Design optimization of wind turbines*, PhD thesis at Politecnico di Milano, 2014

[50] B. Jonkman and L. Kilcher, *Turbsim user's guide*, technical report, NREL, National Renewable Energy Laboratory, 2012

[51] L. Sartori, *System design of lightweight wind turbine rotors*, PhD thesis at Politecnico di Milano, 2019

[52] B. M. Kulfan, *A universal parametric geometry representation method - CST*, 45th AIAA Aerospace Sciences Meeting and Exhibit, Reno, Nevada, Jan. 2007

[53] F. Bertagnolio, H. Aagaard Madsen, C. Bak, and A. Fischer, *Validation of an aeroacoustic wind turbine noise model using advanced noise source measurements of a 500 kw turbine*, 2016 Proceedings of 16th International Symposium on Transport Phenomena and Dynamics of Rotating Machinery, 2016

[54] W. J. Zhu, W. Z. Shen, J. N. Sørensen and G. Leloudas, *Improvement of airfoil trailing edge bluntness noise model*, research article, Advances in Mechanical Engineering, Jan. 2016

[55] P. Hewitt and S. Marques, *Aerofoil optimisation using CST parameterisation in SU2*, Royal Aeronautical Society Biennial Applied Aerodynamics Research Conference, Bristol, July 2014

[56] J. Jonkman et al., *Definition of a 5-MW reference wind turbine for offshore system development*, Technical report NREL, Golden, Colorado, 2009.

[57] A. Croce, *Wind turbine control*, presentation of Corso di generatori eolici, Politecnico di Milano, 2020

[58] L. A. Viterna and R. D. Corrigan, *Fixed pitch rotor performance of large horizontal axis wind turbines*, DOE/NASA Workshop on Large Horizontal Axis Wind Turbines, 1981

[59] L. Sartori, *Free form methodology for aero-structural optimization of wind turbine blades*, Master thesis at Politecnico di Milano, 2013

[60] A. Cairati, *Sensitivity analysis in the design of multi-MW wind turbine rotor blades*, Master thesis at Politecnico di Milano, 2015

[61] C. L. Bottasso, F. Campagnolo, and A. Croce, *Multi-disciplinary constrained optimization of wind turbines*, Multibody System Dynamics, pp. 21-53, 2012

[62] V. Giavotto et al, *Anisotropic beam theory and applications*, Computers & Structures, pp. 403–413, 1983

[63] Regulative norms of IEC 61400-1, *Wind energy generation systems – Part 1: Design requirements*, International Standard, Ed. 4, 2019